UNIVERSITY OF SOUTHAMPTON

The turbulent boundary layer over urban-like roughness

by

Manuel Aguiar Ferreira

Faculty of Engineering and Physical Sciences
Aerodynamics and Flight Mechanics Group

October 2019

Abstract

The sheer scale and nature of urban boundary layers present a number of practical challenges that make remarkably difficult to experimentally determine the aerodynamic characteristics of the surface roughness, or to obtain a complete description of the flow field within the canopy layer, including static-pressure measurements. Consequently, there is a lack of quality data sets against which to validate urban-canopy models for weather forecasting or pollutant dispersion. And the few that exist almost exclusively comprise velocity statistics, so the mechanisms responsible for drag generation that are essentially pressure-based still remain to be investigated. These points are addressed in this work by exploring alternative measurement techniques and analysis methods. A novel floating element (FE) balance is developed to overcome the weaknesses of traditional single-pivot balances, which are sensitive to streamwise pressure gradients and buoyancy effects. Measurements are conducted for two staggered arrays of cuboids with different height distributions, and a detailed uncertainty analysis is carried out. The skin-friction coefficient for both surfaces can be estimated to within 2%. Snapshots of the flow field are taken using planar particle image velocimetry (PIV) at multiple spanwise locations. Mean and instantaneous maps of the overlying static-pressure field are estimated via 2D-RANS and 2D-TH, by neglecting the contribution of the out-of plane components of velocity and acceleration in the momentum transport equation. Special care is exercised to resolve the inner canopy region, so the surface pressure can be extrapolated from the nearest point, and estimates of the form drag and the zero-plane displacement height can be inferred. Comparisons with FE data and other experimental studies demonstrate the viability of this approach for urban-like roughness, when direct measurement techniques are not available, outperforming an ill-conditioned three-parameter fit of the mean velocity distribution. Horizontally-averaged profiles of the streamwise velocity and Reynolds shear stress above and below the canopy top are analysed, drawing attention to the most limiting assumptions of urban canopy models. Specifically, the current results are not consistent with a constant mixing-length distribution or sectional-drag coefficient, and the axial velocity profile across the canopy height does not follow an exponential function. In the interest of improving current formulations, an alternative parameterisation of the sectional-drag coefficient is con-

sidered, which explores the self-similar behaviour of the axial pressure difference across individual roughness elements. Finally, coupled statistics of the forces acting on a target roughness element of a staggered-cube array, in combination with velocity-pressure correlations, are used to elucidate the mechanisms responsible for drag generation and how they relate with the turbulent structure in the roughness sublayer. Evidence suggests that although large-scale structures are not as significant as the small and intermediate scales for the drag-force fluctuations, they still play an important role in modulating the small-scale pressure signal in the near-wall region.

Declaration of Authorship

This is to certify that:

- the present thesis entitled *The turbulent boundary layer over urban-like roughness* comprises my original work towards the PhD at the University of Southampton;

- I have not used any sources other than those listed in the bibliography or identified in the text as references;

- I have not submitted this thesis at any other institution in order to obtain a degree or professional qualification.

Manuel Aguiar Ferreira, October 2019

Acknowledgements

I have received a great deal of support and assistance throughout the writing of this thesis. I am deeply grateful to my supervisor Prof. Bharathram Ganapathisubramani for his enthusiastic encouragement and invaluable advice. It was a fantastic experience having worked with him and to have conducted my research at such an amazing and historic facility. Appreciation is also due to Dr. Roeland De Kat for his willingness to discuss crucial aspects concerning experimental and numerical methods that improved the quality of this work.

I thank my fellow students and friends in the Aerodynamics and Flight Mechanics Group at the University of Southampton for the occasional insightful discussions, the morning tea breaks and after-work shenanigans. Finally, I consider myself fortunate to have a family and a partner, Liz, whose unfounded and unconditional faith in my ability was essential for the completion of my thesis that often felt like an overwhelming challenge. Thank you all for your support.

Contents

List of Figures

List of Tables

Chapter 1

Context of the present research

Turbulence is a complex, chaotic state of fluid motion. It is characterised by sudden changes in flow velocity and pressure stemming from a superposition of events of widely varying size. Although intuitively well-understood, many fail to realise its importance, for most flows occurring in nature and engineering applications are turbulent. A formal understanding of its behaviour is therefore key to predict, for example, the cruising efficiency of aerodynamic and hydrodynamic vehicles, the pumping requirements for pipe networks, or to promote mixing, heat and mass transfer processes. The complexity of turbulent flows lies in the seemingly random motion of the turbulent structures (e.g. eddies), at different scales, that interact with each other. This implies that the movement of a fluid particle cannot take place independently of the general motion (Tennekes et al., 1972). The governing equations of fluid flow, the Navier-Stokes equations, reflect this behaviour, but have thus far revealed to be nearly intractable unless (very often ad hoc) empirical assumptions about the nature of turbulence are introduced. Incidentally, even though each individual turbulent flow is essentially unique, they have many common characteristics that are associated with their initial and boundary conditions. This allows deriving general formulations that apply to entire classes or families of turbulent flows, which broadly fall into two categories: unrestricted shear flow, including jets and wakes, and wall-bounded turbulence. The present thesis addresses a subset of the latter, namely, developing boundary layers over urban-like roughness, which is arguably one of the most relevant problems in fluid mechanics today.

1.1 Turbulent boundary layer

The boundary layer is described by Prandtl (1904) as the narrow region where the flow velocity relative to a solid surface gradually decreases from its value in the freestream to zero at the wall. The *no-slip* condition is enforced by the viscosity of the fluid, however small it may be, as a result of momentum exchanges during molecular collisions with

the wall. Boundary-layer flows are driven by the energy extracted from the mean flow. Turbulent velocity fluctuations create large momentum fluxes, termed Reynolds stresses, which transfer the energy inwards where it is ultimately dissipated by the viscous action. More specifically, Townsend (1976) showed that the flow of energy in a boundary layer is adequately represented by a two-layer model, wherein the Reynolds stress gradient in the outer layer provides a continuous supply of energy from the mean-flow to the inner layer, within which most of it is converted into turbulent energy by the fluid shear. The inner part of the flow further includes a sublayer of constant stress that is close to a condition of absolute energy equilibrium, as the local turbulent production and the viscous dissipation are nearly balanced (Schubauer, 1954). The first is only marginally higher, creating an energy surplus that is diffused into the outer region. Approaching the wall, the viscous effects become increasingly significant and, within the viscous sublayer, turbulent eddies are annihilated altogether.

A particular feature of turbulent boundary layers is that the each part of the flow exhibits distinct characteristic length (and time) scales. In the outer layer, the size of the largest eddies, which control the entrainment of non-turbulent fluid, is prescribed by the boundary-layer thickness δ. On the other hand, the typical length scale in the inner layer reflects the interaction between the turbulent mechanisms and the viscous constraint imposed by the wall. It is thus on the order of ν/U_τ, where ν is the kinematic viscosity of the fluid and U_τ is the friction velocity, a measure of the turbulence intensity level. The frictional Reynolds number

$$Re_\tau = \frac{\delta U_\tau}{\nu} \qquad (1.1)$$

represents the ratio between these scales, and is of great importance for characterising turbulent boundary-layer flows, because of its profound implications. As the spectral separation increases — with increasing Re — the processes responsible for the main structure of turbulent motion become independent of viscosity and exhibit a universal behaviour. This is an essential aspect of all generalisations about the nature of turbulent flows. A prime example are the *similarity hypotheses* of Kolmogorov (1962) concerning the local structure of turbulence; another is the state of energy equilibrium outlined above, and existence of a constant shear-stress layer, from which follows the *law of the wall* (Coles, 1956); equally important is the hypothesis of *Reynolds similarity* by Townsend (1976), which asserts that the outer-flow structure of boundary layers can be expressed non-dimensionally in terms of suitable scales of velocity and length. These and other fundamental generalisations, albeit controversial, play a central role in fluid mechanics and are essential for engineering purposes. The Reynolds number is then a crucial parameter in design of experiments, determining the behaviour on the flow investigated.

1.2   The impact of surface roughness

Surface roughness is ubiquitous for all wall-bounded flow problems. Its effects may, however, be neglected for surfaces whose characteristic roughness length scale is smaller than the depth of the viscous sublayer, where the turbulent production is completely suppressed. If this condition is satisfied, the surface is said to be hydraulically smooth. Otherwise, pressure-based forces parallel to the wall become important, and the growth of the boundary layer may depend weakly or not at all on the fluid viscosity, in which case the flow becomes transitionally or fully rough, respectively. In this regime, the contribution of the viscous layer to the total stress is negligible and the term roughness sublayer is used instead to indicate the region dynamically influenced by the roughness length scales.

The collective influence of the roughness elements typically leads to an increase of the turbulence intensity throughout the entire boundary layer, yielding greater momentum transfer rates (increased surface stress and faster growth rate). Like the smooth-wall counterpart, rough-wall turbulent boundary layers may also achieve an energy equilibrium state in the sense described by Townsend (1976), provided the roughness features are smaller than the boundary layer thickness and are uniformly distributed. Turbulent motions within the constant stress layer are then controlled not only by the length scale ν/U_τ, but also by the representative roughness height y_0. The ratio between them $y_0^+ = y_0 U_\tau/\nu$, commonly referred to as the roughness Reynolds number, quantifies the effect of wall roughness on the flow development — the larger it is, the greater the departure of the mean flow structure from the smooth-wall equivalent at matching Re_τ. Besides introducing an additional length scale, surface roughness poses yet another complication: while the origin of the boundary layer is well defined over a flat plate, it cannot be readily identified over rough surfaces. The roughness elements vertically shift the mean flow by some amount, expressed by the zero-plane displacement height d, that is a function of the surface topology. d is usually a portion of the roughness height, but a definite agreement on what it represents is still lacking.

1.3   Current challenges

Perhaps the greatest challenge turbulence research faces today is the prohibitive cost of achieving very high Reynolds numbers. This is detrimental for drawing conclusions about the asymptotic behaviour of turbulent flows, since viscous effects, as small as they may be, are still dynamically relevant with potential undermining consequences. A case in point is Townsend's hypothesis of Reynolds similarity that has always been a subject of disagreement, especially over rough walls. Numerous authors have tested its validity (see e.g., Flack and Schultz, 2010), reporting both opposing and supporting data.

The prevailing view is that mean flow universality emerges at sufficiently high Reynolds number, if the roughness height is a small portion of the flow depth. These conditions are particularly stringent for boundary layers above urban areas, which are characterised by exceedingly high Reynolds numbers and relatively tall buildings that may disrupt the outer-flow structure and delay the development of a constant stress layer (condition for energy equilibrium). Consequently, analysis methods and lower-order models that rest on scaling and similarity laws often yield inaccurate results. Indirect techniques to estimate crucial boundary-layer parameters from experimental velocity data, such as the wall shear stress and the zero-plane displacement, are notably sensitive in this regard. Direct methods are in turn independent of the flow conditions, yet their measurement principle either restricts application to a limited number of surface roughness (oil-film interferometry and pressure tapping) or are too complex to set up (floating-element devices).

For over half a century, considerable effort has been made towards developing correlations between the relevant flow parameters (y_0 and d) and the surface roughness characteristics. Under conditions of energy equilibrium and Reynolds similarity, this would allow predicting the shear stress incurred by arbitrary surfaces as well as the overlying boundary-layer flow. Although several approaches have been suggested, some of which show promising results (e.g. Macdonald et al., 1998; Grimmond and Oke, 1999; Flack and Schultz, 2010), an accurate universal law is still far from reach owing to the continuum of roughness distributions observed in practice. Examples include closely-packed, sand-grain roughness associated with pipe flows, regularly-distributed, discrete roughness such as urban canopies and wind farms, and naturally-occurring roughness featuring a range of scales that emerge from gradual deposition and/or growth processes. Specifically for urban canopies, formulations that attempt to model the flow within have become a popular alternative to empirical correlations (Macdonald, 2000; Yang et al., 2016). These models appear to perform reasonably well in predicting the roughness length in the constant-stress layer and displacement height, and are sensitive to the shape of the obstacles, the relative planar distribution and wind direction. As ever, they make crucial assumptions about the flow structure — i.e. exponential spatially-averaged velocity profile within the canopy and constant sectional-drag coefficient (Castro, 2017) — which occasionally prove to be invalid. Relaxing these requirements is therefore essential for improving weather prediction and scalar dispersion models above urban areas, or an entirely new approach must be considered.

Contrary to smooth-wall boundary layers, the roughness effects on wall turbulence are far less understood. Surface roughness is known to alter the turbulence characteristics within the roughness sublayer, but the same basic elements are present in each case (Grass, 1971; Djenidi et al., 1999; Kanda, 2006; Coceal et al., 2007). Furthermore, it has been demonstrated that the largest turbulent structures leave a footprint on the near-

wall region (Mejia-Alvarez et al., 2014) and modulate the intensity of the small scales (Perret and Rivet, 2013; Nadeem et al., 2015; Basley et al., 2018) in a similar manner as over smooth walls. It remains, however, unclear how these turbulent processes are affected by the geometry of the surface (Basley et al., 2019; Perret et al., 2019), or what the mechanisms responsible for drag generation are. The broad parameter space is a fundamental obstacle to understanding the dominant flow dynamics. Equally challenging is the fact that wall shear stress is predominantly pressure based, so time-resolved measurements cannot be readily obtained using standard techniques, except for idealised urban areas which generally consist of regularly-distributed arrays of cuboids.

1.4   Plan of thesis and author contributions

The present thesis investigates the impact of urban-like roughness on the development of turbulent boundary layers, specifically tackling some of the challenges listed above. In chapters 2 and 3 we address the difficulty of accurately measuring the surface drag and other flow parameters when similarity laws do not hold. Chapter 2 presents the design of a novel floating-element balance that privileges accuracy and reliability. It is able to decouple the wall-normal component of the aerodynamic load and is insensitive to mild pressure gradients, as opposed to more traditional devices. An alternative approach is considered in chapter 3, tailored for urban boundary-layer flows, using pressure-reconstruction methods based on in-plane velocity information. Instantaneous and mean maps of the pressure field within and above the canopy are obtained, from which the roughness length scale y_0 and displacement height d can be estimated. In chapter 4 we identify some of the shortcomings of semi-empirical canopy models and examine the existence of a self-similar behaviour of the axial pressure difference across individual roughness obstacles and its potential modelling aspects. This is achieved by exploring the mean velocity and pressure data over two staggered arrays of cuboids introduced in chapter 3. Finally, the turbulence dynamics within the roughness-affected layer and interactions with the canopy flow are investigated in chapter 5. We primarily focus on characterising the drag force acting on a target roughness element, and establishing the interrelations with the turbulent structure of the overlying flow. The main findings of this thesis are summarised in chapter 6.

This work is presented as four separate chapters $(2-5)$ that have either been already published, are under consideration or yet to be submitted for publication:

Ferreira, M. A., Rodríguez-López, E. and Ganapathisubramani, B. An alternative floating element design for skin-friction measurement of turbulent wall flows. *Experiments in Fluids*, 59:155, 2018

Ferreira, M. A. and Ganapathisubramani, B. PIV-based pressure estimation in

the canopy of urban-like roughness. *Experiments in Fluids*, Manuscript under consideration.

Ferreira, M. A. and Ganapathisubramani, B. Scale interactions in velocity and pressure over a staggered cube array. *Journal of Fluid Mechanics*, Manuscript in preparation.

It has additionally been partially presented by the author in the following conferences:

Ferreira, M. A., Rodríguez-López, E. and Ganapathisubramani, B. A novel approach for quantifying the zero-plane displacement of rough-wall boundary layers. In 70th Annual Meeting of APS Division of Fluid Dynamics, Denver, Colorado, November 19-21, 2017.

Ferreira, M. A. and Ganapathisubramani, B. Conditional structure of the boundary layer over large cube roughness. iTi Conference on Turbulence, Bertinoro, Italy, September 5-7, 2018.

Ferreira, M. A. and Ganapathisubramani, B. The pressure field within the canopy of urban-like roughness. In 71st Annual Meeting of APS Division of Fluid Dynamics, Atlanta, Georgia, November, 18-20, 2018.

Ferreira, M. A. and Ganapathisubramani, B. Scale interactions in velocity and pressure over urban-like roughness. In 71st Annual Meeting of APS Division of Fluid Dynamics, Seattle, Washington, November, 23-26, 2019.

Chapter 2

An alternative floating element design for skin-friction measurement of turbulent wall flows

Indirect methods to estimate surface shear stress are commonly used to characterise rough-wall boundary layer flows. The uncertainty is typically large and often insufficient to carry out quantitative analysis, especially for surface roughness where established scaling and similarity laws may not hold. It is, thus, preferable to rely instead on independent measurement techniques to accurately measure skin friction. The floating element was one of the first to be introduced, and still is the most popular for its features. Although its fundamental principle has remained unchanged, different arrangements have been suggested to overcome its inherent limitations. In this paper, we review some of these designs and further present an alternative that is able to correct for extraneous loads into the drag measurement. Its architecture is based on the parallel-shift linkage, and it features custom built force transducers and a data acquisition system designed to achieve high signal-to-noise ratios. The smooth-wall boundary layer flow is used as a benchmark to assess the accuracy of this balance. Values of skin-friction coefficient show an agreement with hot-wire anemometry to within 2% for $Re_\theta = 4 \times 10^3$ up to 10^4. A rough surface of staggered distributed cubes with large relative height, $\delta/h \simeq 10$, is also investigated. Results indicate the flow reaches the fully rough regime, at the measurement location, for the entire range of Reynolds number. Furthermore, the values of skin friction agree with existing estimations from alternative methods.

2.1   Introduction

Estimation of the surface shear stress τ_w is vital for any description of wall bounded flows. It is generally expressed in terms of the friction velocity $U_\tau = (\tau_w/\rho)^{1/2}$, which is an important scaling parameter for the structure of turbulent boundary layers. It may alternatively be expressed non-dimensionally by the skin-friction coefficient $C_F = \tau_w/q_0$, where $q_0 = \rho U_0^2/2$ is the freestream dynamic pressure, ρ is the density of the fluid and U_0 the freestream velocity. In fact, under certain conditions (Townsend, 1976), the mean flow profile and turbulent stresses over smooth surfaces can be solely expressed as a function of U_τ and the length scale δ, the boundary-layer thickness. The friction velocity is then commonly determined via indirect methods, like the Clauser chart (Clauser, 1956), by introducing assumptions about the flow structure. If the latter are not met, however, the basis of these methods become dubious, and consequently the accuracy of their estimate. This is often the case for boundary layers developing over rough surfaces, where the characteristic roughness height h constitutes an additional length scale which dynamically influences the near wall region (Jiménez, 2004). Evidence of such flows, where equilibrium and similarity hypothesis do not hold, is found in the experimental works of Krogstad et al. (1992), Antonia and Krogstad (2001), Medjnoun et al. (2018), amongst others. Flows past discontinuities in surface roughness are another prime example where indirect methods prove to be inadequate. So much so that seminal works have mostly drawn conclusions based on observations. Quantitative analyse have also been conducted, but in all cases the newly adjusted layer represented a significant fraction of the total boundary-layer thickness (Antonia and Luxton, 1971).

Direct measurement techniques, in contrast, benefit from being completely independent of the flow conditions. Some of the most popular include the floating element (FE), pressure-based methods and oil-film interferometry, out of which only the first provides the flexibility to carry out experiments with arbitrary surface topologies. Oil film is convenient if the wall shear stress (WSS) is of purely viscous nature (Pailhas et al., 2009; Medjnoun et al., 2018), whereas pressure-based methods apply to rough surfaces that are instead dominated by pressure drag, such as uniform arrays of large two-dimensional ribs or cubes (Antonia and Luxton, 1971; Cheng and Castro, 2002). The FE principle was introduced by Kempf (1929) nearly a century ago, and since then its use has become widespread. Today, there is a broad variety of FE designs tailored to meet specific requirements. A comprehensive review by Winter (1979) of existing devices reveals many diverse applications: from low-speed to supersonic flows, under distinct pressure gradient, heat and mass transfer conditions. Current designs still share similar features, but rely on more sophisticated signal conditioning systems, or large-scale facilities (Baars et al., 2016a) to improve the quality of the estimates. In addition, micro-electromechanical systems have recently enabled small-scale FE with remarkable

frequency response and spatial resolution (Schmidt et al., 1988; Sheplak et al., 2004). Despite their popularity, few studies have actually achieved acceptable levels of uncertainty. Agreement of FE measurements with alternative techniques or established skin friction laws is generally no better than 5% for smooth-wall boundary layers. The one of Baars et al. (2016a) stands out for achieving a discrepancy level to within 1% at high Reynolds number, but its large dimensions restrict utility in smaller-scale facilities. In this paper, we present a self-contained FE design for studying rough-wall turbulent boundary layer (TBL) flows, which privileges accuracy and reliability. Its technical aspects are discussed in section 2.2, followed by a detailed description of the experimental methods in section 2.3, including calibration and uncertainty analysis. Finally, measurements of skin friction over a smooth and a rough wall are presented in section 2.4.

2.2   The floating element

Essentially, the FE principle consists in measuring the streamwise net force F_w acting on a finite area S of a boundary-layer plate that is made structurally independent of the rest of the surface. This element is flush mounted, but can move freely in the planar directions facilitated by the existence of an air gap surrounding it. The mean WSS is then obtained via $\tau_w = F_w/S$. FE measurements are subject to a variety of error sources, predominantly of systematic nature, which limit their accuracy and repeatability. There have been few attempts to fully characterize their impact given the practical difficulties to parametrically change the setup of FE and the singular features of each device (O'Donnel, 1964; Brown and Joubert, 1969; Allen, 1977, 1980; Acharya et al., 1985). Consequently, error sources are often quantified by dimensional arguments alone. Here, we review the critical aspects to the design of WSS balances that ultimately determine the quality of their estimates.

2.2.1   Design considerations

Important error contributions arise from the necessary gap surrounding the FE, which makes it sensitive to (i) static pressure differences acting on non-parallel surfaces to the flow. Other sources of uncertainty are associated with (ii) misalignments of the FE relative to the boundary-layer plate and (iii) buoyancy forces resulting from uneven pressure distributions over the flow-exposed surface.

According to Brown and Joubert (1969), contribution (i) is the combination of the direct action of the freestream pressure gradient across the balance, F_α, and of the cavity-induced flow into and out from the test section, F_m. The resultant net force effectively masks out the action of the WSS. They suggest, as a first approximation, that $F_\alpha \propto \lambda \rho \alpha S$ and $F_m \propto \rho \gamma U_\tau \alpha^{1/2} S^{3/4}$, where $\alpha = (1/\rho)\partial p/\partial x$ is the kinematic pressure

gradient, λ is the lip thickness and γ is the nominal gap width, as indicated in figure 2.1. To minimise these loads, we engineered the fixed-to-floating surface joint to a tight tolerance, featuring an S-shaped labyrinth seal (0.5 mm thick and 15 mm long) to artificially tighten the gap. Baars et al. (2016a) used instead a grooved-path labyrinth seal that is intrinsically more efficient, though it requires a thicker lip and it may prove difficult to implement. Alternatively, filling the gap with liquid could eliminate unknown pressure forces on the side walls of the FE (the surface tension can be easily quantified). This arrangement is particularly suitable for studies under conditions of non-zero pressure gradient (ZPG), such as those carried out by Frei and Thomann (1980) and Hirt et al. (1986), but was discarded for practical reasons. Note, the relationships mentioned above assume the spurious flow is solely driven by the static pressure gradient. They ignore the pressure difference between the flow-exposed surface and the underside of the FE, Δp, with potentially greater significance. Enclosing the underside passively contributes towards reducing Δp, but it is advantageous being able to actively control the pressure differential as well. In the present device, this is achieved by means of a centrifugal blower, as depicted in figure 2.2.

The vertical misalignment of the FE (ii) was initially investigated by O'Donnel (1964) using a single-pivot balance. Years later, Allen (1977, 1980) further considered the influence of varying parameters λ and γ, and extended this analysis to parallel-shift designs (the reader is referred to Winter (1979) for a detailed description of both mechanisms). Although his empirical relations may not be directly transferable to other devices, the trends are expected to remain the same. So, they can still be used as guidelines to design balances that are essentially insensitive to misalignments. His results show that, for a fixed protruded or recessed position of the FE relative to the surrounding surface, wider gaps and thinner lips yield smaller lip forces. These act in the direction of a positive drag force and therefore should be minimised. Accordingly, the FE comprises a 1 mm thick flange that extends 10 mm outward, effectively reducing the lip size, and its edges were rounded off to prevent flow separation. The gap, on the other hand, was primarily designed to negate contribution (i), so it is smaller than would be desirable in terms of sensitivity to misalignments. In any case, the relative position of the FE was optically verified to a resolution of 15 μm before each test, by imaging the fixed-to-floating surface joint using a 16MP camera with high magnification.

Allen (1977) additionally demonstrated how the static pressure distribution over the flow-exposed surface is affected for different protrusion values, causing the centre of pressure to move about. This phenomenon is commonly known as buoyancy (iii) and may have a similar impact to that of contributions (i) and (ii) depending on the design of the FE. If simply supported on a single pivot point (Allen, 1977, 1980; Acharya et al., 1985; Krogstad and Efros, 2010), the pressure-induced moment is coupled with the moment produced by the surface shear stress — this effect becomes less important

if the pivot point is moved farther away from the wall. In contrast, planar supported elements are naturally insensitive in this regard. One of the first designs of this kind is the parallel-shift linkage, which is equivalent to extending the lever arm to infinity, thereby keeping the floating surface parallel to the flow (Kempf, 1929; Dhawan, 1951; Coles, 1953). The present device is based on this arrangement, as shown in figure 2.1. Other alternatives have also been successfully employed, like placing the FE in a pool of liquid (Frei and Thomann, 1980; Hirt et al., 1986) or using air bearings (Ozarapoglu, 1973; Baars et al., 2016a).

The existence of a fixed-to-floating surface joint entails a perturbation of the boundary-layer flow as it goes over, regardless of all design considerations. Different to contributions (i) – (iii), this error source is of random nature and primarily influences the signal-to-noise ratio (SNR) of the measurement. Here, we evaluate the extent of spurious flow over the FE by using the scaling argument introduced by Baars et al. (2016a). They argue that, for small perturbations the extent of contaminated flow adjacent to the edges of the element is roughly proportional to its perimeter and the gap size or misalignment, whichever is higher. Correspondingly, the ratio of the total surface area to the edge affected area is defined as a proxy for the SNR; it follows from the schematic in figure 2.1 that $\eta_A \simeq l^2/(4\gamma l)$. Large η_A values are desirable to improve the quality of the signal. However, practical restrictions in size of wind-tunnel facilities frequently dictate the general dimensions of these devices, and increasing manufacture tolerances as a way to tighten the gap comes with an increase in cost of the project. As a consequence, η_A is typically $\mathcal{O}(10)$ and it is highly challenging to achieve larger values. The FE developed by Baars et al. (2016a) for the large-scale wind tunnel at the University of Melbourne is notable for having $\eta_A = 375$.

2.2.2 Mechanical configuration

The unique design of the present device enables measuring not only the streamwise component of the aerodynamic load but also the induced pitching moment, as a mean to decouple extraneous loads from the measurement of WSS. Its assembly, shown in figure 2.1, consists of a closed aluminum frame with outer dimensions $220\,\mathrm{mm} \times 220\,\mathrm{mm} \times 40\,\mathrm{mm}$ ($W \times L \times H$), which holds all the mechanical and electronic components inside.

The working principle behind the WSS sensor is similar to that of a parallel-shift linkage. The streamwise load acting on the floating element (1) is directly transmitted to the floating frame below (5), which in turn is supported by a pair of flexures (4) that allow it to move freely along the streamwise direction and a pair of rigid blades (8). These are fixed to the upstream and downstream sides of the casing (3), respectively. The FE is supported by a set of holders (2) which rotate freely about the pivot point (7). The pitching moment generated around it is then counteracted by the pair of blades (6), mounted horizontally on each side of the floating frame. The pivot mechanism consists of
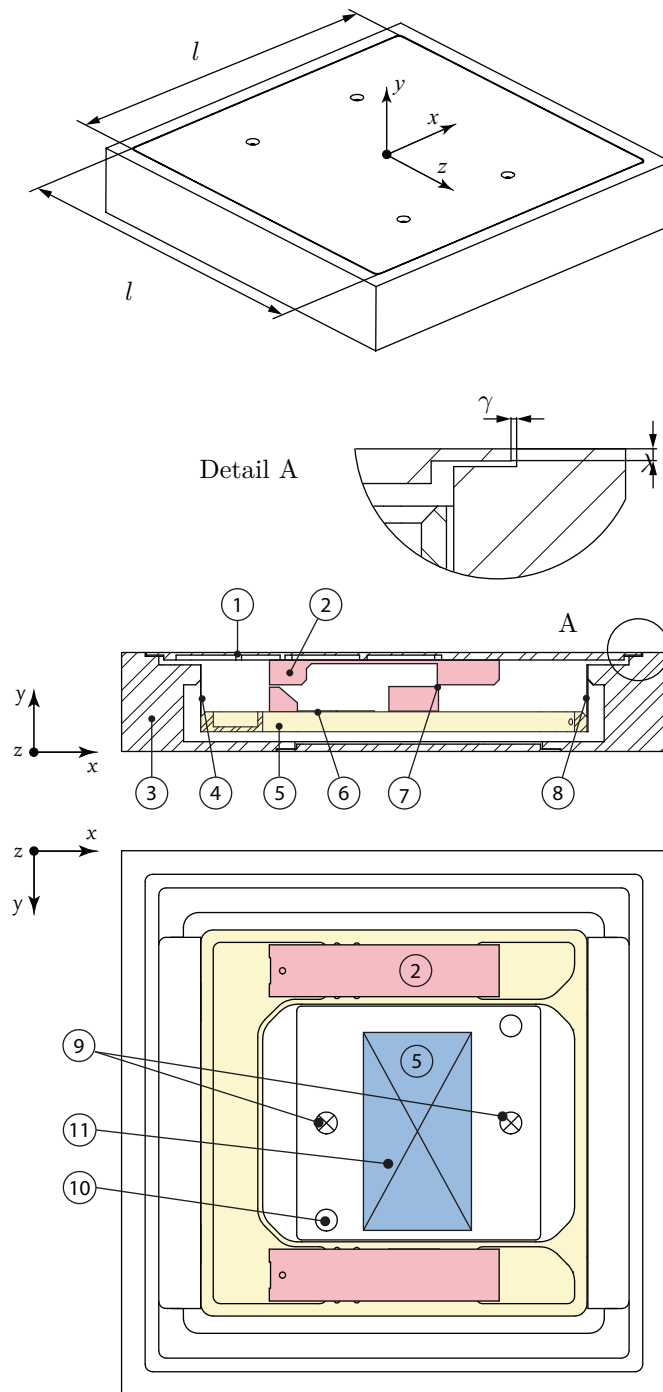
FIGURE 2.1: DRAWINGS OF THE FLOATING-ELEMENT BALANCE. From top to bottom: isometric view with general dimensions, slice along the *X-Y* plane and top view. (1) Floating element, (2) holders, (3) sealed chamber or casing, (4) flexure, (5) floating frame, (6) pitching moment transducer, (7) pivot point, (8) WSS transducer, (9) outlet to the blower, (10) static pressure taps, (11) acquisition module.
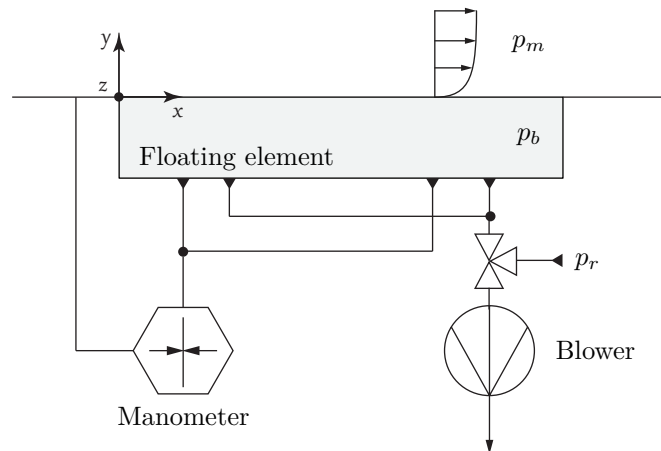
FIGURE 2.2: ACTIVE PRESSURE CONTROL SYSTEM. The FE is aligned with the wind tunnel floor over which a boundary-layer grows. p_m is the mean static pressure in the test section, p_r is the room pressure and p_b is the pressure inside the balance.

a 0.05 mm flexure that is clamped on either sides with a free-standing length of less than 0.5 mm to prevent it from buckling. Both pairs of blades, (6) and (8), are instrumented with metal gauges for strain measurement, and their sensitivity can be adjusted by varying the effective length. In the current configuration, the vertical transducers are fixed-supported aluminum blades 15 mm long, 10 mm wide and 0.45 mm thick. Those for the pitching moment are instead simply-supported, 15 mm long and 0.6 mm thick, resulting in greater sensitivity. The sensing element is a 200 mm side square, small enough in relative terms to ensure local measurement of WSS. Its dimensions are such that the variation in friction coefficient C_F is less than 1% between the leading and trailing edges. The $1/7^{th}$ law skin-friction relationship was used to obtain estimates of the local C_F for a smooth-wall boundary layer at $Re_x \simeq 2 \times 10^6$. This corresponds to a freestream velocity of $10\,\text{ms}^{-1}$ and a development length of approximately 3 m, according to the experimental setup described in section 2.3. In view of error contributions (i) and (ii) (refer to section 2.2.1), the fix-to-floating surface joint was carefully designed to a very tight clearance. Detailed in figure 2.1, the lip $\lambda = 1$ mm ± 0.1 and the gap $\gamma = 0.5$ mm ± 0.1, with a 15 mm long labyrinth seal which further mitigates cavity-induced flow asymmetries. Finally, the size of the FE and the gap width yield an effective surface area coefficient of $\eta_A = 100$. This value is much larger than average and falls in the same order of magnitude of the one from the large-scale TBL facility in Melbourne, though its dimensions are significantly smaller in comparison (the area ratio is 75).

This balance also features an external centrifugal blower used to modify the pressure inside, p_b. There are two nozzles mounted at the bottom, one on each of the two sides of the acquisition module, as depicted in figure 2.1. This is to ensure uniform pressure distribution on the underside of the FE and to minimize airflow inside the balance. p_b is monitored via two pressure taps, included in the same schematic, mounted on opposite

corners away from the nozzles. The circuit is detailed in figure 2.2. Both the pressure taps and the ports to the blower inlet are externally connected. The blower is driven by a 24VDC motor that is controlled through pulse-width modulation and is able to generate up to 1400 Pa of head pressure. The intensity of the blower can further be adjusted by regulating a three-way valve placed upstream, which lets air from the room to be sucked in.

Relevance of the pitching moment

One of the primary challenges to WSS measurement consists in designing a mechanism that is sensitive to streamwise loads alone. The ability of the system to negate other components is mostly related to geometrical tolerances, and in this particular case to the electrical characteristics of the strain sensors as well. It is virtually impossible to attain perfect orthonormality between the parts that make up the FE. So the pair of force transducers (8), in figure 2.1, may be slightly off the wall-normal direction, and similarly its strain gauges may exhibit a small misalignment between themselves and the blades. The balance is therefore not completely insensitive to normal loads, as drag transducers have intrinsically some degree of transverse sensitivity (in the axial direction). Although this effect is ordinarily quite small, it still stands as a source of bias error if Δp is not equalised. To circumvent this limitation, we use the pitching moment sensor to control the blower such that the pressure-induced force is canceled out. This is possible since the pivot point is offset from the centroid of the FE, and provided the buoyancy effects are not significant. In which case, the center of pressure could shift toward the location of the pivot point, hence reducing the moment produced by the vertical load. Furthermore, the latter cannot entirely be eliminated for rough-wall boundary layers as the zero-plane displacement effectively constitutes a lever arm for the WSS. The magnitude of the moment it induces is relatively smaller, yet entails the existence of a nonzero net vertical force to balance it.

Compliance

The tight clearance between the floating and fixed surfaces of this device, and the additional complication of an extra degree of freedom, demand a thorough examination of the motion of the FE. This is a function of the stiffness of the force transducers, the geometry of the balance and the loads it may likely experience.

In the facility described in section 2.3, the typical local Reynolds number Re_θ of smooth-wall boundary layers is $\mathcal{O}(10^3)$ (Dogan et al., 2016), for free-stream velocities ranging from 10 up to $25\,\mathrm{ms}^{-1}$. Under these conditions, the maximum integrated skin friction over the sensing area is approximately $50\,\mathrm{mN}$ from the logarithmic correlation of Österlund et al. (2000), $C_F = 2((1/\kappa)\ln(Re_\theta) + 4.08)^{-2}$. It is less straightforward

estimating the WSS over rough walls as it highly depends on its topology. Still, it is safe to assume loads up to two orders of magnitude larger for the rougher cases, $\mathcal{O}(1)\,\mathrm{N}$. Knowing the dimensions of the force traducers, it is possible to determine their maximum deflection and thereby estimate the corresponding displacement of the element. To illustrate, an integrated shear stress of $1\,\mathrm{N}$ applied $5\,\mathrm{mm}$ away from the wall would displace it along the streamwise direction by $3.5\,\mu\mathrm{m}$, and the maximum step height at the leading edge due to inclination of the surface would be $40\,\mu\mathrm{m}$. In terms of viscous units ν/U_τ, where ν is the kinematic viscosity of the fluid, the protrusion would be smaller than 3 for the highest freestream velocity, ensuring the FE is hydraulically smooth across its whole range of operation. Note, this analysis neglects any pressure difference between the top and the underside of the FE that is generally kept to a minimum.

2.2.3 Data acquisition system

The ability of the balance to measure WSS depends, amongst other factors, on the integrated wall drag, the sensitivity of the force transducers and the effective resolution of the analog-to-digital converter (ADC). Since practical restrictions in size of the FE limit the magnitude of the force it experiences ($F_w = \tau_w S$), an acquisition module able to provide a stable low-noise signal is paramount to ensure the quality of the measurements. In this section, we briefly explain the signal conditioning system especially designed for this application, which involves a 4-channel acquisition module and two sets of active strain sensors, one for each of two load components (drag and pitching moment).

Force transducers

The WSS produced by a smooth-wall boundary layer was considered to estimate the required sensitivity of the force transducers and resolution of the ADC. Specifically, one developing in the low-speed wind tunnel described in section 2.3, at $Re_\theta = 3830$ and a freestream velocity of $10\,\mathrm{ms}^{-1}$ (Dogan et al., 2016). This is expected to be the most demanding testing condition with $C_F = 3.05 \times 10^{-3}$, based on the relationship of Österlund, yielding an integrated skin friction of $F_{wmin} \simeq 7.3\,\mathrm{mN}$.

Ideally, the number of noise-free binary quantization levels of the ADC, $\#counts$, is given by the ratio between the full-scale load, F_{FS}, and the desired resolution. The former was taken to be $\mathcal{O}(1)\,\mathrm{N}$, which is roughly the maximum bulk drag generated by a rough patch with large relative height, and the minimum resolution is defined as 0.1% of F_{wmin}; thus, $\#counts = 1.37 \times 10^5$. Considering the geometry of the FE, the sensitivity to WSS is defined as $\Sigma_{F_w} = 2K\epsilon_{FS} = 0.1636\,\mathrm{mV/V}$, where K is the Young modulus of the blades and ϵ_{FS} is the mechanical strain under full-scale load. A factor of 2 was introduced since two force transducers are used in parallel. With a $5\,\mathrm{V}$ excitation voltage, the full-scale output of each drag transducer is $V_{FS} = (0.1636/2) \times 5 = 0.41\,\mathrm{mV}$,

yielding a minimum peak-to-peak noise-free resolution of $V_{p-p} = 2.99\,\mathrm{nV}$. Assuming normally distributed noise, its root-mean-square (RMS) is estimated from the peak-to-peak value using the coverage factor $k = 6.6$, which corresponds to a confidence interval of 99%; $V_{RMS} = V_{p-p}/k = 0.46nV$. The requisites of noise-free and effective resolution were then estimated as,

$$R_{free} = \log_2 \frac{V_{FS}}{V_{p-p}} = \log_2 \frac{0.41\mathrm{mV}}{2.99\mathrm{nV}} = 17.07 \tag{2.1}$$

$$R_{eff} = \log_2 \frac{V_{FS}}{V_{RMS}} = \log_2 \frac{0.41\mathrm{mV}}{0.46\mathrm{nV}} = 19.77. \tag{2.2}$$

These values indicate that at least a 20-bit ADC is required to achieve the skin-friction resolution mentioned above. An equivalent analysis was conducted for the pitching moment sensor whose sensitivity is $\Sigma_{F_w} = 0.1696\,\mathrm{mV/V}$, similar to that of WSS.

Acquisition module

The acquisition module was designed in-house around the integrated circuit AD7195 from Analog Devices. It is driven by a 5 V power supply and it includes the required signal conditioning, filtering and an ultra-low noise 24-bit sigma-delta ADC. The bridges on the force transducers were arranged in six-lead assemblies, where the same source is used both as the reference for the digital converter and for exciting the strain sensors. This way, changes to the excitation do not introduce measurement error as the output is ratiometric. An AC square wave is used to excite the force transducers which, together with the chopping scheme on the ADC, is able to cancel out induced DC errors, effects of parasitic thermocouples, and to average out pink noise that is dominant at low frequencies in these kind of applications. As a result, the acquisition system is capable of producing discernible output signals with a much lower excitation voltage in comparison to DC-driven sensors, enjoying a much higher SNR. The printed circuit board was dimensioned to fit inside the balance. The wiring from the bridges to the acquisition module were therefore kept short and are shielded by the aluminium case, hence reducing electromagnetic interferences. Wind tunnel off, the RMS of the noise is 56 nV/V and goes up to 190 nV/V once the drive unit is enabled.

2.3   Experimental methods

The FE is currently employed in the suction-type wind tunnel of the experimental fluid mechanics laboratory at the University of Southampton. This open-return wind tunnel has a 7:1 contraction followed by a closed working section 4.5 m long with cross-section 0.9 m wide and 0.6 m high. The free-stream turbulence intensity has been reported
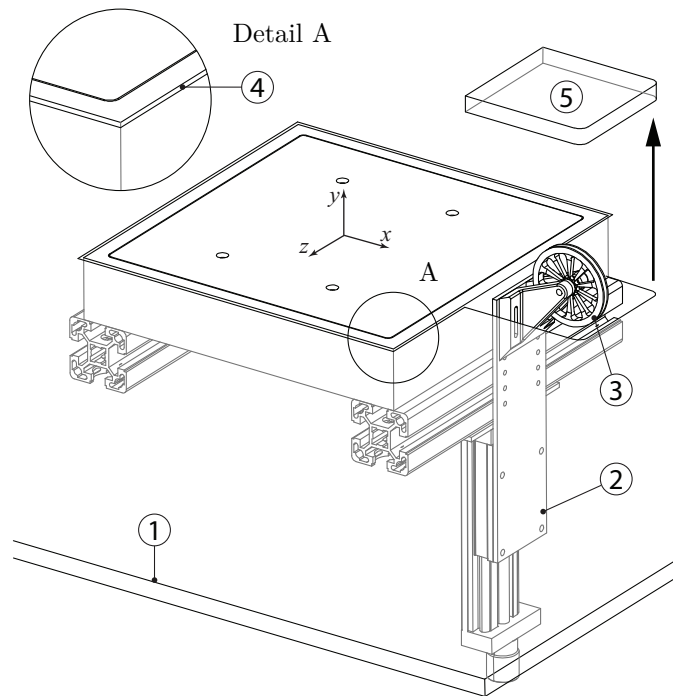
FIGURE 2.3: SMOOTH-WALL SETUP. The FE is flush mounted with the wind tunnel floor (1) and the gap surrounding the balance (4) is taped over to prevent leaks. The pulley (3) is attached to a linear traverse (2) which in turn is bolted onto the main frame. To calibrate, the lid (5) is removed to make way for the pulley to move into the test section. A wire is then strung over to suspend the weights.

to be homogeneous and lower than 0.5% at the measurement location (Claus et al., 2012b; Placidi and Ganapathisubramani, 2018). Despite not featuring an adjustable roof, experiments were conducted in nominal ZPG as the acceleration parameter could be neglected; it is on the order $\mathcal{O}(10^{-8})$. The walls of the test section are optically transparent to facilitate using imaging techniques, like particle image velocimetry (PIV), and the floor is cut out to fit the FE balance. The setup is illustrated in figure 2.3.

We consider two different kinds or surface topology: a smooth wall, used as the benchmark to assess the viability of this device, and a staggered array of cubes with 0.25 plan solidity fraction. Its relative height $h/\delta \simeq 0.1$, where h is the height of roughness obstacles and δ is the thickness of the boundary layer. This particular surface roughness has been previously studied by Claus et al. (2012b) and Cheng and Castro (2002), who provide direct measurements of WSS using a pivot-type FE and pressure-tapped roughness obstacles, as well as vertical profiles of the normal and shear stresses obtained via cross-wire anemometry. Boundary-layers are established directly on the wind tunnel floor, following the contraction. Before reaching the working section, they experience an intense favorable pressure gradient, which in the smooth-wall case undermines the validity of existent empirical relationships for the skin-friction coefficient. Furthermore, tripping conditions have been shown to impact the development of TBL (Rodríguez-

López et al., 2016). For these reasons, the local skin friction is instead estimated from a series of hot-wire anemometry of the velocity profile.

2.3.1   Hot-wire anemometry

Hot-wire measurements of the streamwise velocity profile were taken 3.3 m downstream of the contraction, at the centreline of the FE, as depicted in figure 2.4. A total of 9 freestream velocities equally spaced between 10 and 26 ms^{-1} were considered.

$$x = 3.3\,\mathrm{m}$$
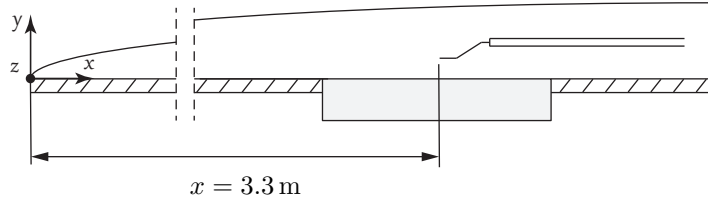
FIGURE 2.4: SMOOTH-WALL AND HOT-WIRE ARRANGEMENT. Measurements were taken at the centreline of the FE, 3.3 m downstream of the test section.

The boundary-layer probe is an Auspex A55P05 with 10 mm long prongs spanned by a 3 mm long and 5 μm diameter tungsten wire. The central active region is approximately 1 mm long and is shouldered on either side by copper-plated sections, yielding an effective length-to-diameter ratio of 200. The wire was operated by a Dantec StreamLine Pro constant temperature anemometer (CTA) system set to an overheat ratio of 1.8. We used the National Instruments USB-6212 BNC ADC to sample the signal at 20 kHz. Pre- and post-calibrations were conducted using a Pitot-static tube, mounted at the same streamwise location, that was connected to a Furness FCO510 micromanometer. The temperature was constantly monitored throughout calibration and acquisition stages using a T-type Omega thermocouple. Each velocity profile is populated by 30 points taken for a sampling period of $T = 40$ s, which in the worst case ($U_0 = 10\,\mathrm{ms}^{-1}$) is equivalent to $T\delta/U_0 = 8000$ eddy turnover times.

The mean skin friction was estimated using the method proposed by Rodríguez-López et al. (2015). Accordingly, the mean velocity profile is compared with a canonical description of the boundary layer following Musker (1979), for the inner and logarithmic layers, and using the exponential wake by Chauhan et al. (2009). The method allows adjusting the wall-normal coordinate to overcome any potential uncertainty in determining the initial relative position of the wall-probe. The skin friction is then estimated as that which minimizes the error between the experimental and canonical profiles. For further details on this method the reader is referred to the original paper (Rodríguez-López et al., 2015). The accuracy in determining U_τ is better than 1% for perfectly accurate velocity profiles and better than $0.5\nu/U_\tau$ for the initial relative position of the wall-probe. The method was originally validated against DNS and experimental databases, under presence of mild pressure gradients, wall-probe interference in the inner layer and
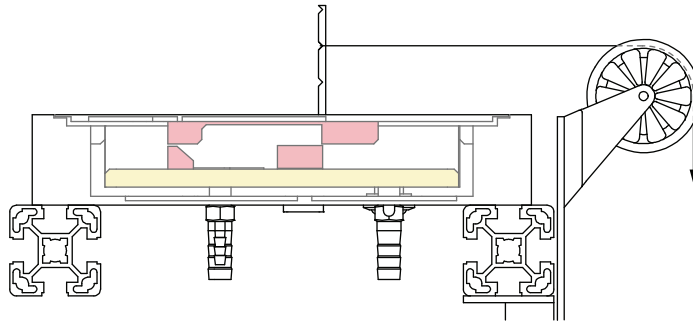
FIGURE 2.5: TYPICAL CALIBRATION SETUP. In this schematic, the see-through casing shows the alignment of the stud with the pivot point. The wire is looped around it, in the middle notch, and goes over the pulley that is mounted on the linear traverse. The nozzles to the centrifugal blower and pressure taps are also visible.

poorly converged data. Additionally, it has been shown to perform adequately in highly disrupted flows past strong tripping conditions (Rodríguez-López et al., 2016), porous fences (Rodríguez-López et al., 2017) and TBL under freestream turbulence (Esteban et al., 2017).

2.3.2 Static calibration

The balance was statically calibrated *in situ* using a set of weights and the wire-pulley arrangement pictured in figure 2.5. The pulley is an ME-9450 from Pasco with 50 mm diameter to string and an effective coefficient of friction of 7×10^{-3}. It was attached to a 50 mm linear traverse which enabled adjusting its vertical position to within 0.05 mm. For calibration purposes, a 40 mm long stud with machined-in grooves was mounted perpendicularly to the FE at the spanwise centerline, above the pivot point. A 0.1 mm nylon wire was then looped around it and strung over the pulley. A small mass was suspended to tension the wire, so that its alignment could be adjusted. First, by sliding the traverse system across the spanwise direction; secondly, by turning the knob to adjust the vertical position of the pulley to a predetermined height.

Prior to any acquisition, the device was turned on and let to warm up for 2 hours. The calibration involved recording the response of the strain sensors to $n = 24$ load combinations using M1-class weights. The output voltages were sampled for 20 s to average out noise and the mean values of each pair of transducers were summed up. For the smooth-wall, 6 different weights including the zero reading (0, 1, 3, 5, 10 and 15 g) were applied at 4 different heights (0, 9.6, 19.2 and 28.8 mm). This process was repeated 5 times to achieve statistical significance, so a grand total of 120 calibration points were taken. Note the loading direction of the balance over the course of the calibration changed to account for potential hysteresis. The values of force F_w (N) and pitching moment M_y (Nm) were obtained by multiplying the mass of the weights by the local gravity acceleration $g = 9.81084 \, \mathrm{ms^{-2}}$, from the land gravity survey data by the

British Geological Survey.

We consider the second-order response surface model in two variables:

$$y = \beta_1 x_1 + \beta_2 x_2 + \beta_{11} x_1^2 + \beta_{22} x_2^2 + \beta_{12} x_1 x_2 + \epsilon. \tag{2.3}$$

By letting $x_3 = x_1^2$, $x_4 = x_2^2$, $x_5 = x_1 x_2$, $\beta_3 = \beta_{11}$, $\beta_4 = \beta_{22}$ and $\beta_5 = \beta_{12}$, equation 2.3 is rewritten in matrix form as

$$Y = X\beta + \epsilon, \tag{2.4}$$

where

$$Y = \begin{bmatrix} y_{11} & y_{12} \\ y_{21} & y_{22} \\ \vdots & \vdots \\ y_{n1} & y_{n2} \end{bmatrix}; \; X = \begin{bmatrix} x_{11} & x_{12} & \dots & x_{15} \\ x_{21} & x_{22} & \dots & x_{25} \\ \vdots & \vdots & & \vdots \\ x_{n1} & x_{n2} & \dots & x_{n5} \end{bmatrix}; \; B = \begin{bmatrix} \beta_{11} & \beta_{12} \\ \beta_{21} & \beta_{22} \\ \vdots & \vdots \\ \beta_{51} & \beta_{52} \end{bmatrix}.$$

$Y_{n \times 2}$ is the calibration design matrix; its rows i refer to different loading conditions and the columns j are for the individual components of the applied load, that is F_w and M_y, respectively. The model matrix, $X_{n \times 5}$, contains information about the response of the force traducers to each load combination (in units of mV/V), as well as information about the model form - the number of columns corresponds to the number of terms in the right-hand side (RHS) of equation 2.3. The regression coefficients B are estimated via weighted least squares (WLS) fit to account for the uncertainty in the predictors. This is particularly important as the size of the dataset is fairly small. From Strutz (2016),

$$\hat{B}_{kj} = (\bar{X}^T W^j \bar{X})^{-1} \bar{X}^T W^j Y, \tag{2.5}$$

where $\hat{B}$ is the least squares estimator of B, W^j is the weighting matrix for a particular degree of freedom (DOF), j; and the *overbar* indicates averaged quantities over all calibration runs (5 in total). As suggested by Reis et al. (2013), the weighting matrix V_w is computed as the sum of the error contributions due to weights and the wire-pulley setup, such as misalignments and friction forces, and the variance in the readings of the strain sensors V_r. Accordingly,

$$W^j = (V_w^j + D^j V_r D^{jT})^{-1}. \tag{2.6}$$

The second term on the RHS of equation 2.6 should be thought of as the projection of the variance in the readings onto the estimated load. $V_{r\,2n \times 2n}$ is diagonally symmetric and is computed as the covariance between the readings of the force traducers, whereas $D^j_{n \times 2n}$ is the sensitivity matrix whose diagonal contains the partial derivatives of equation 2.3 with respect to a given DOF. Finally, $V^j_{w\,n \times n}$ is a diagonal matrix and its values are statistically approximated by the sum of squared residuals (SS_E) of the fit by replacing
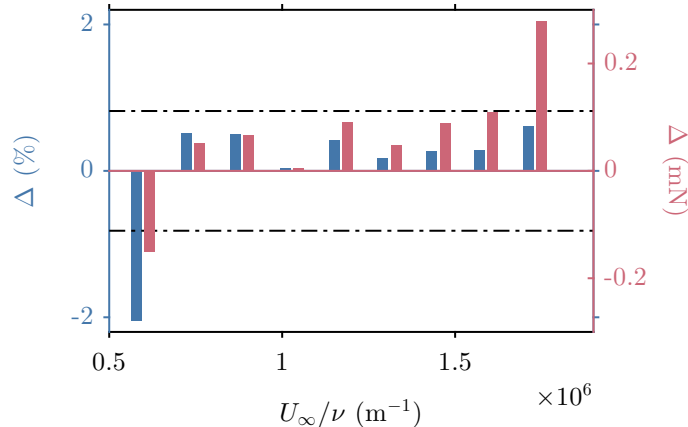
FIGURE 2.6: LONG TERM STABILITY OF THE CALIBRATION. Relative (left) and absolute (right) discrepancies between measurements of wall drag for the smooth-wall boundary-layer case over a range of Reynolds numbers. Drag values were obtained using different calibrations performed two weeks ahead of and after the measurements.

W for the identity matrix.

The parameters of the linear regression are listed in equation 2.7. They also appear divided by the respective uncertainty $|\hat{B}/u_B|$ to highlight the relative importance between them. u_B is the positive square root of the main diagonal elements of $(\bar{X}^T W^j \bar{X})^{-1}_{5\times5}$, which is the covariance matrix of the model coefficients.

$$\hat{B} = \begin{array}{c} \begin{array}{cc} F_w & M_y \end{array} \\ \begin{bmatrix} -2.178 & 81.439 \\ 0.002 & -115.143 \\ -0.115 & -91.906 \\ -0.075 & -121.468 \\ 0.124 & 106.961 \end{bmatrix} \end{array}; \quad \left|\frac{\hat{B}}{u_B}\right| = \begin{array}{c} \begin{array}{cc} F_w & M_y \end{array} \\ \begin{bmatrix} 31.45 & 6.41 \\ 0.02 & 9.09 \\ 0.05 & 0.21 \\ 0.03 & 0.30 \\ 0.05 & 0.26 \end{bmatrix} \end{array} \qquad (2.7)$$

The large magnitude of B_{11} in comparison to the remaining terms reveals a strong linear behavior of the drag sensor, independent of the pitch moment acting on the FE. On the contrary, the latter appears to be equally dominated by the linear and nonlinear terms of both force transducers. The corresponding values of $|\hat{B}/u_B|$, however, indicate that the relative importance of the second order terms is negligible as the associated variance is significantly high. This is likely due to lack of orthogonality in the design of the response model (Johnson et al., 2010). The variance inflation factor (VIF) is a statistical indicator that quantifies the degree of multicollinearity in a least squares regression. As a rule of thumb, the value of VIF is ideally kept under ten, but in this particular case is $\mathcal{O}(10^2)$, which is explained by the large cross correlation value between the readings; $x_{i1} \otimes x_{i2} = 0.953$. Still, the standard error of the fitting is relatively small. $\hat{\sigma}_{F_w} = 0.057$ mN and $\hat{\sigma}_{M_y} = 0.006$ mN.m, where $\hat{\sigma}^2 = \text{SS}_E/(n-5)$.
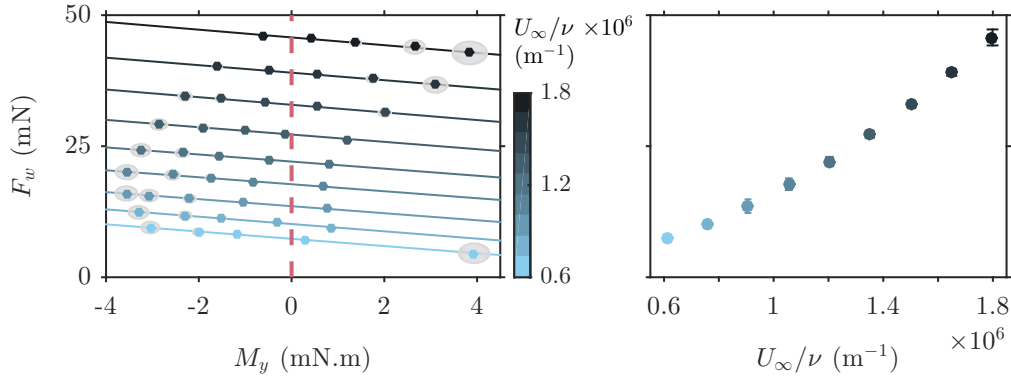
FIGURE 2.7: METHOD TO EVALUATE THE WSS. On the left: at each *Re* number, indicated by the colormap, there were acquired 5 data points across a range of pressures p_b. Linear curves were then fit to each individual set in order to infer the drag value for which the pitching moment is null, indicating the absence of a vertical net force. The gray-shaded regions show the uncertainty associated with the measurements, addressed in section 2.3.4. On the right: intercept of the linear regressions and corresponding uncertainty bar as a function of unit *Re*.

A series of pre- and post-calibrations were carried out over the course of one month to assess the long term stability of the balance to environmental changes and setup. The difference between measurements of WSS obtained using linear estimators from calibrations performed weeks apart are shown in figure 2.6. Apart from the data point taken at the lowest Reynolds number, discrepancies between calibrations are generally smaller than 0.5% with a standard deviation of just over 0.8%, or 0.1mN in absolute terms.

2.3.3   Measurement of wall-shear stress

The balance is first turned on and left warming up for 2 hours, unless a pre off-tunnel calibration was performed before the measurement. In the meantime, the tunnel is run for an extended period to ensure steady flow conditions. The acquisition sequence is fully automated; it starts with a shakedown period of 3 minutes during which the wind tunnel is set at the maximum freestream velocity. It is then turned off for half an hour before zeroing the balance. This initial kick guarantees the very first data point is taken under the same conditions as the first data point of subsequent runs. A total of 9 drag values were acquired over a range of *Re* for both the smooth and the rough wall. The evaluation method is illustrated in figure 2.7. For each freestream velocity the pressure inside the balance p_b is progressively varied using the blower such that the pitching moment passes through the zero-crossing. This experiment was conducted in a suction wind tunnel, so the static pressure in the test section is naturally lower than p_b. Consequently, given the location of the pivot point, the pitching moment is initially positive but gradually becomes negative with increasing suction of the blower. The values of wall drag are the

Y-intercept of the linear regression through each set of data points acquired at fixed *Re*, where the pitching moment is null. This is a necessary step since the extraneous contribution of the vertical load to the measurement of WSS is minimized when the moment it induces is canceled out, as explained in section 2.2.2. Acquisitions last $30\,\text{s}$ at $150\,\text{Hz}$, equivalent to 2500 boundary layer turnover times at the lowest operating velocity. Between them, a readjustment period of 3 minutes is given for the response of the system to reach a nearly constant value. The SNR of these measurements is found within the range $1 < \sigma/\mu < 5$, where σ and μ are the standard deviation and the mean value of the signal, respectively. Once the run is over, the wind tunnel is turned off and the balance set to idle for another period of half an hour between runs. The aforementioned procedure is repeated 5 times for the results to achieve statistical significance.

Alternatively to the linear regression method described above, it is possible to implement a PID controller to drive the blower as a function of the pitching moment. The acquisition process is therefore expedited since only one data point is taken at each *Re*, as opposed to 5. The accuracy of the controller is dependent on the sensitivity of the blower and resolution of the duty cycle.

2.3.4 Uncertainty estimates

This analysis follows the rules established by the International Bureau of Weights and Measures for evaluating and expressing uncertainty in measurement (BIPM et al., 2008). The complete uncertainty budget for the friction velocity U_τ is given in figure 2.8 as a function of the Reynolds number. It factors the most important contributions, including: (a) calibration errors, (b) the inference method of WSS, (c) the inclination of the FE, (d) determination of air properties, temperature and pressure, and (e) precision of the measurements.

By definition $U_\tau = \sqrt{\tau_w/\rho_0}$; the WSS is expressed as $\tau_w = F_w/S$ and the air density is obtained via the ideal gas law $\rho_0 = p_0/(RT_0)$, where $R = 287.05\,\text{JKg}^{-1}\text{K}^{-1}$ is the specific gas constant, p_0 is the atmospheric pressure and T_0 is the room temperature. Hence, $U_\tau(F_w, T_0, p_0)$ is a function of three independed variables. Assuming all input quantities are uncorrelated, the combined uncertainty of U_τ is the positive square root of the variance $u_{U_\tau}^2$, written as

$$
u_{U_\tau}^2 = \underbrace{\left(\frac{\partial U_\tau}{\partial F_w}\right)^2 u_{F_w}^2}_{(a)+(b)+(c)} +
$$
$$
+ \underbrace{\left(\frac{\partial U_\tau}{\partial T_0}\right)^2 u_{T_0}^2 + \left(\frac{\partial U_\tau}{\partial p_0}\right)^2 u_{p_0}^2}_{(d)} + \underbrace{u_{rep}^2}_{(e)},
$$

$$(2.8)$$
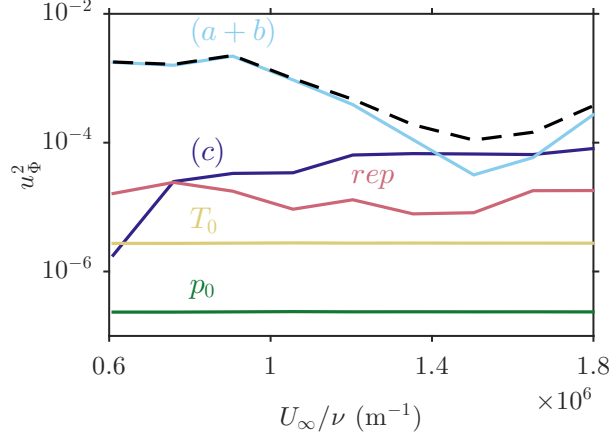
FIGURE 2.8: UNCERTAINTY BUDGET. Breakdown of the total variance of U_τ, *black dashed-line*, as a function of Reynolds number. The *light-blue* line shows the contribution both due to calibration errors and the wall-drag evaluation method, $u_{(a+b)}$; *dark-blue* line refers to the error induced by the inclination of the FE, $u_{(c)}$; the *green* and *yellow* curves show, respectively, the uncertainties associated with pressure and temperature, $u_{(d)}$; the *red* line reflects the repeatability of the measurements, $u_{(e)}$.

where u_Φ is the standard uncertainty of the arbitrary variable Φ.

Contributions (a) & (b). The first term on the RHS of equation 2.8 is the combination of sources (a), (b) and (c), which are inherent to the working principle of the balance. Particularly, (a) and (b) cannot be decoupled; the calibration error $u_{(a)}$ propagates through the linear regression and is reflected in the uncertainty estimate of the Y-intercept, from here on denoted $u_{(a+b)}$. $u_{(a)}$ is determined by multiplying the readings of the force transducers by the covariance matrix of the calibration coefficients $(\bar{X}^T W^j \bar{X})^{-1}_{5\times 5}$, defined in section 2.3.2. Accordingly,

$$u_{(a)_j} = X(\bar{X}^T W^j \bar{X})^{-1})X^T, \tag{2.9}$$

where $u_{(a)_j}$ is the uncertainty associated with the load component j (drag or pitch), $\bar{X}$ is the averaged model matrix of the calibration, W^j is the weighting matrix for j and X is the vector containing the readings of the force transducers, written according to the model form expressed in equation 2.3. Potential errors induced by wire misalignments, friction of the pulley and weight application are all factored into the covariance matrix W^j. Further details can be found in Reis et al. (2013). $u_{(a+b)}$ amounts to approximately 97% of the total variance at low *Re* but only 30% at higher values. In absolute terms, its magnitude is fairly independent of the loading conditions, so its relative significance diminishes with *Re* as opposed to that of $u_{(c)}$, which increases monotonically to become the primary source of uncertainty.

Contribution (c). Surface inclination causes the pressure-based wall-normal load F_n to be projected in the streamwise direction. Similarly to WSS, this error contribution is a

flow-driven phenomenon which manifests as an offset in skin-friction coefficient (Baars et al., 2016a). Provided a constant tilt angle, it can be corrected for. However, the additional DOF of the present device rules out this possibility. It thus stands as a source of bias error that must be included in the uncertainty budget, $u_{(c)}$. The streamwise projection $F'_w = F_n \sin(\alpha)$, where α is the tilt angle of the FE. Then it follows that,

$$u_{(c)}^2 = \underbrace{\left(\frac{\partial F'_w}{\partial F_n}\right)^2 u_{F_n}^2}_{=0} + \left(\frac{\partial F'_w}{\partial \alpha}\right)^2 u_\alpha^2. \tag{2.10}$$

The flow-exposed surface is mounted parallel to the principal flow direction, thus $sin(\alpha) = 0$ and u_{F_n} can readily be ignored. In turn, the accuracy of the digital spirit level $(0.1°)$ in addition to the maximum predicted rotation of the FE $(0.075°)$, yields $u_\alpha \simeq 0.125°$. The second term of equation 2.10 can be rewritten as $[\Delta p_d\, S\, \cos(\alpha)]^2\, u_\alpha^2$, where Δp_d is the pressure difference at which wall-drag is evaluated. Considering that buoyancy forces, no matter how small, entail the existence of a net vertical force when the pitching moment is canceled out, Δp_d will depend on the flow conditions. Specifically, the latter increases with Re, hence the trend $u_{(c)}$ exhibits in figure 2.8.

Contribution (d). Air density is function of the atmospheric pressure and room temperature, $\rho_0(p_0, T_0)$. The first was acquired at the start and finish of the experiment, using a weather station accurate to within $100\,\mathrm{Pa}$. The mean value was then assigned to p_0, so it follows that its uncertainty includes not only the accuracy of the measurement system but also the range of the fluctuations; $u_{p_0} = \sqrt{(P_{0_{acc}})^2 + (P_{0_{max}} - P_{0_{min}})^2}$. The freestream temperature, on the other hand, was continuously monitored using a T-type Omega thermocouple with an accuracy of $0.5°$. A similar system was dedicated to measure temperature inside the balance.

Differential pressures were monitored via three Furness FCO510 micromanometers (model 2) with full scale (FS) ranges of 200 and $2000\,\mathrm{Pa}$. These have a reported accuracy of ± 1 digit bellow 20Pa and 0.25% of the reading above this threshold. The freestream dynamic pressure q_0 is acquired via a Pitot-static tube positioned above the FE, aligned with its leading edge. Following the assumption of a thin boundary-layer, potential wall-normal pressure gradients are neglected and the pressure over the flow-exposed surface of the FE is taken to be the equal to the local static pressure. The static port is then shared with a second manometer, by means of t-junction, to monitor the pressure difference between the top and underside of the FE Δp. Additionally, the streamwise pressure gradient $\partial p/\partial x$ is estimated by measuring the pressure drop between the aforementioned Pitot-static tube and another Pitot probe mounted far upstream, assuming a linear growth of the boundary-layer. Note that from these quantities solely q_0 represents a source error in $C_f(F_w, q_0)$. Despite playing a roll on the uncertainty estimation of F_w, that of Δp is not factored in this analysis (refer to equation 2.10).

2.4   Results

Measurements of skin friction for both the smooth- and the rough-wall were acquired following the procedure described in section 2.3.3. A total of 5 runs were performed in subsequent days for freestream velocities ranging between $U_0 = 10$ and $26\,\mathrm{ms}^{-1}$ in increments of $2\,\mathrm{ms}^{-1}$. Pre- and post-calibrations were performed for each configuration without notable discrepancies, owing to the long term stability of this device.

2.4.1   Smooth wall

Values of WSS inferred from hot-wire anemometry of the boundary-layer profile were used as the standard of comparison for the FE measurements. The results, given in figure 2.9, show an excellent agreement between these techniques, especially for Re_θ over 5×10^3 ($U_0 = 14\,\mathrm{ms}^{-1}$) where the relative difference between them falls below 2%. For the most part, the disparity of the data at low freestream velocities may be explained by the increased uncertainty in the measurement; with the exception of the first data point, whose error bar does not encompass the power curve fit through the hot-wire values. In absolute terms, the magnitude of the force discrepancy is approximately $0.92\,\mathrm{mN}$, which makes it remarkably difficult to identify its cause. This could either be an indication of additional error sources which were not accounted for, or of poorly estimated uncertainty contributions. A similar behavior is observed on the skin friction measurements of Baars et al. (2016a), who suggested that it could be related to secondary loads acting on non-parallel surfaces to the flow and to the projection of the pressure-based force in the streamwise direction that could not be fully eliminated. From these potential contributors, the first was not considered in the uncertainty analysis presented in section 2.3.4. Additionally, it is plausible to assume some residual coupling of the vertical net force, despite the measures to workaround this limitation.

The smooth-wall skin friction relationship of Österlund et al. (2000) is also included in figure 2.9 for comparison. While the values of C_F obtained from hot wire share the same trend, they are generally lower by 2%. This is also true for the FE measurements at higher Reynolds numbers, plausibly for the reasons discussed in section 2.3: the streamwise pressure gradient in the contraction and tripping conditions.

2.4.2   Rough wall

C_F measurements of the rough-wall boundary layer are shown in figure 2.10. Values obtained using the present FE take a nearly constant value (to within 1%) across the entire range of Re, which indicates the flow reaches the fully rough regime farther upstream of the balance location. Here, we determine the equivalent sand-grain roughness k_s, normalised to viscous units $k_s^+ = k_s U_\tau / \nu$, based on the boundary-layer thickness
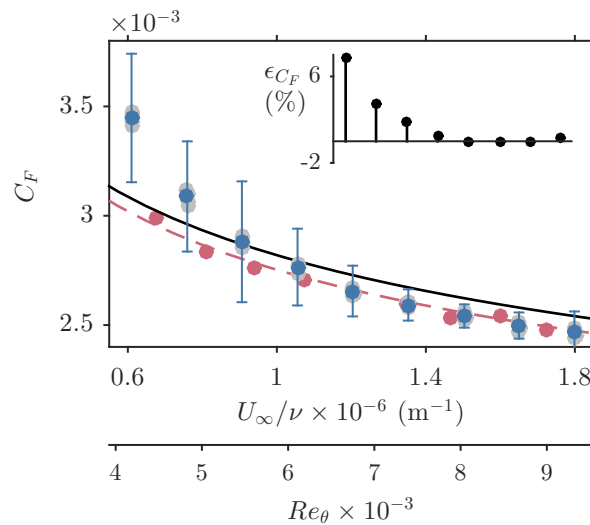
FIGURE 2.9: SMOOTH-WALL FRICTION COEFFICIENT. C_F as a function of unit Re and Re_θ. *Red* circles show the values inferred from hot-wire anemometry; the *dash-line* is a power curve fit though those points. *Blue* circles are the mean FE measurements; the error bars indicate the magnitude of the uncertainty. The *black solid line* is the smooth-wall skin friction correlation for Re_θ from Österlund et al. (2000), $C_F = 2((1/\kappa)\ln(Re_\theta) + 4.08)^{-2}$. The inset shows the relative discrepancy of the FE measurements from the values of hot-wire anemometry.

reported by Cheng and Castro (2002) for the same flow conditions; $\delta = 0.12\,\mathrm{m}$ at $U_0 = 10\,\mathrm{m/s}$. Assuming the functional form for the viscous-scaled mean velocity profile U^+ of Coles (1956), the downward shift relative to the smooth wall case $\Delta U^+ = 13.8$. This yields $k_s^+ = 1070$ that is well above the empirical threshold $k_s^+ \geq 80$ from which the flow/surface becomes fully rough (Jiménez, 2004). The test-retest variability of the measurements appears to have worsened comparing to the smooth wall, revealed by the spread of individual (grey) data points around the mean. At high Re, it becomes in fact the largest uncertainty contribution. Additional estimates of C_F are included in the same figure, specifically that inferred from cross-wire anemometry of the boundary-layer profile by Cheng and Castro (2002), and those obtained by Claus et al. (2012b) using a pivot-type FE and pressure-tapped roughness obstacles. Overall, the wall drag over the staggered array of cubes is substantially higher compared to the smooth wall and the disparity between the estimates is on the order of 25%.

Claus et al. (2012b) highlighted the marked discrepancy between their measurements and advanced the hypothesis that, while trends with Re are correct, the uncertainty in the pressure data could undermine the validity of the form-drag estimate. They further argue, by comparing the results from both techniques, that a lower C_F of the FE would imply a negative friction drag contribution. On these grounds, and given the quoted uncertainty of their FE (Krogstad and Efros, 2010), they concluded the absolute pressure-drag value is likely overestimated. The present measurements support this ob-
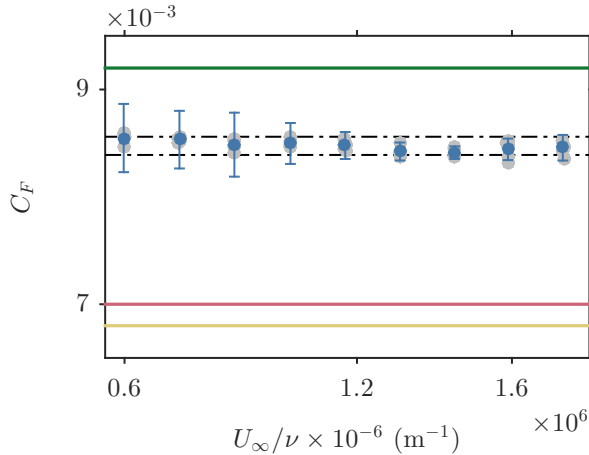
FIGURE 2.10: ROUGH-WALL FRICTION COEFFICIENT. *Blue* circles are the mean FE measurements of C_F for each unit *Re*; the error bars indicate the magnitude of the uncertainty. The *black dash-dotted* lines indicate the $\pm 1\%$ bound around the mean value over the range of *Re*. The *yellow* line shows the value inferred from the Reynolds shear stress by Cheng and Castro (2002); and the *red* and *green* indicate the values obtained by Claus et al. (2012b) using a pivot-type FE and pressure-tapped roughness obstacles, respectively.

servation, as the mean skin friction coefficient $\overline{C_F} = 8.45 \times 10^{-3}$ is still 8% lower than that of the pressure data. However, they do not agree with the FE estimate of Claus et al. (2012b) which is 17% lower in comparison. To explain this discrepancy, it would be required to carry out a comprehensive uncertainty analysis of their measurements, otherwise we can only speculate. Two plausible sources of error are contemplated here. The first is related to the streamwise pressure gradient, which could be neglected in terms of flow development (based on the acceleration parameter), but still stands as a source of buoyancy effects. Naturally, the suction wind tunnel where these experiments were conducted imposes a favourable pressure gradient in the freestream and over the flow-exposed surfaces. Since the distribution on the underside of the FE is likely to be uniform, the pressure difference across Δp becomes larger downstream. As small as it may be, this effect induces a moment opposite to the action of the WSS that could result in an apparent drag reduction considering the setup of Claus et al. (2012b). Another potential source of uncertainty has to do with roughness-induced pressure inhomogeneities within the canopy. When the roughness length-scale is comparable to the size of the FE, the integrated vertical pressure force is likely to lie off-centre, thus creating a spurious moment around the pivot point with similar consequences to that mentioned above depending on the obstacles distribution.

Cheng and Castro (2002) reported wind-tunnel measurements over geometrically identical staggered arrays of cubes, 10 and 20 mm tall. They evaluate C_F for both surfaces from spatially averaged shear stress profiles, using cross-wire anemometry. For the largest case, they further provide an estimate based on the pressure distribution over

a unit area, and verified that the shear stress in the inertial subrange is roughly 21% lower in comparison – it possibly does not reflect the spatial anisotropy within the canopy. In view of this observation, Reynolds and Castro (2008) defined a correction factor for the WSS of staggered arrays of cubes based on the shear stress profile ($U_\tau = 1.12\sqrt{-\overline{uv}}$), which Placidi and Ganapathisubramani (2015) extended to arbitrary cubical arrays with varying frontal and plan solidities. The underlying assumption to this approximation is that the ratio between the shear stress above the canopy and the total surface stress remains constant, or it changes marginally with fetch. Accordingly, we can use the value of C_F obtained by Cheng and Castro (2002) taken at the same fetch as the present experiment, shown in figure 2.10, to obtain a corrected estimate of C_F to compare against the FE measurement. This yields a skin friction coefficient of 8.8×10^{-3} that is only 4% higher. A slight overestimation could either be explained by the uncertainty associated with the form-drag data, which was not provided, or by limitations of the aforementioned assumption. Nevertheless, the agreement is remarkable.

2.5 Conclusion

In this paper, we proposed a self-contained FE design based on the parallel-shift linkage. Different from traditional arrangements, one set of flexures was replaced by single bending-beam transducers to monitor the streamwise load. The position of the FE is then fixed and it does not require preloading. Additionally, pitching moment transducers in liaison with a centrifugal blower successfully mitigate the potential coupling of the vertical load due to residual transverse sensitivity of the force transducers. A second order polynomial in two variables was used to calibrate the balance. The typical standard error of the fitting is $\hat{\sigma}_1 = 0.057\,\text{mN}$ and $\hat{\sigma}_2 = 0.006\,\text{mNm}$ for drag and pitch, respectively. The FE showed a notable long term stability, as discrepancies between the results obtained with calibrations carried out one month apart are generally smaller than 0.5%.

Measurements of skin-friction coefficient C_F for a smooth-wall boundary layer agree with values inferred from hot-wire anemometry to within 2% for $Re_\theta > 4 \times 10^3$. A detailed uncertainty analysis revealed that the most important error contributions are related to the calibration and drag evaluation method, as well as the tilt angle of the FE. In contrast, the test-retest variability amounted to a small fraction of the total uncertainty budget. This experiment further considered the flow over a rough surface of staggered distributed cubes with large relative height ($\delta/h \simeq 10$) and 0.25 solidity fraction. Results showed that the boundary-layer is fully rough at the measurement location, since C_F takes a nearly constant value across the range of Reynolds number and $k_s^+ = 1070$ at the lowest operating velocity ($U_0 = 10\text{ms}^{-1}$). The mean skin friction coefficient $\overline{C_F} = 8.45 \times 10^{-3}$ was compared against estimates from previous studies. Of

particular interest is the FE measurement of Claus et al. (2012b), which underestimates the present value by 17%, highlighting the importance of buoyancy effects on pivot-type balances. It was additionally possible to establish a comparison with estimates obtained from cross-wire anemometry of the boundary layer, provided by Cheng and Castro (2002), assuming $U_\tau = 1.12\sqrt{-\overline{uv}}$ (Reynolds and Castro, 2008). In this case, the relative difference in C_F is approximately 4%.

Notwithstanding the performance of the FE balance, it is important to note that it was initially designed to measure not only the surface drag but also the associated pitching moment, as a means to infer the zero-plane displacement height. This was, unfortunately, impossible to achieve because the pitching moment induced by surface drag and that induced by the vertical load, which arises from the pressure difference across the FE, could not be decoupled. To effectively measure the zero-plane displacement, it would then be required an additional vertical force sensor and to significantly reduce the residual transverse sensitivity of the force transducers, given the large relative magnitude of the vertical load.

Chapter 3

The pressure field within the canopy of urban-like roughness: an experimental approach

In-plane velocity measurements from PIV are used to estimate the pressure field above and within the canopy of two staggered arrays of cuboids, with distinct height distributions, via 2D-RANS and 2D-TH. The viability of this approach is examined by first comparing the mean drag profiles against reported wind-tunnel measurements that were carried out under similar test conditions and numerical simulations (LES and DNS). The surface drag is extrapolated from the nearest data point surrounding the roughness elements. Secondly, estimates of the friction velocity U_τ^p and the zero-plane displacement height d^p are obtained by integrating the axial pressure difference across each individual obstacle, assuming it is spanwise uniform. These are compared against direct measurements of the wall-shear stress from a floating-element balance and a pressure tapped cube, as well as against estimates from indirect methods. In addition to mean pressure maps, snapshots of the pressure field are obtained via 2D-TH, based on Taylor's Hypothesis, which are used to compute the RMS of the pressure fluctuations on the surface of a cube. The results indicate that 2D-RANS and 2D-TH perform adequately, providing reasonable estimates of the mean pressure distribution and of the boundary-layer flow parameters, outperforming indirect methods which rely on equilibrium assumptions that are often not verified.

3.1 Introduction

Experimental studies of boundary-layer flows over urban environments are generally limited to velocity data. Few provide a detailed description of the surface pressure over the roughness obstacles and it is not yet clear how direct measurements of the

surrounding pressure field could possibly be achieved. In fact, only Cheng et al. (2007) and Claus et al. (2012b) have examined the change in pressure distribution and its effects on cube arrays with varying wind direction and packing density. Their analysis sought to document the flow statistics and the aerodynamic characteristics of different surfaces, i.e. the effective roughness height y_0 and the zero-plane displacement d, by pressure tapping opposite faces of a roughness element. This approach is particularly attractive for *d-type* surfaces, like transverse ribs (Antonia and Luxton, 1971), because a single wall-normal array of pressure taps is sufficient to estimate the form drag. In contrast, cubical arrays require a bidimensional grid, which, due to space restrictions, may have to be distributed over multiple identical obstacles to guarantee an adequate spatial resolution (e.g. Claus et al., 2012b). Further complications arise for surfaces with non-uniform height distributions, as each repeating unit is comprised of multiple elements with different aspect ratios, some of which may be too small to accommodate tapping holes. Measuring surface pressure then becomes a complex and somewhat cumbersome procedure. An alternative approach would be to use a non-intrusive technique to measure the surrounding static-pressure field and extrapolate the value on the surface. Direct methods have been successfully used, for example, using micro-air bubbles as pressure sensors (e.g. Ooi and Acosta, 1984; Ran and Katz, 1994), however, they are strictly used in water tunnels and still present serious limitations with respect to the density and the distribution of the bubbles. They are also not compatible with particle image velocimetry (PIV), so simultaneous measurements of the flow field and the overlying pressure distribution cannot not be obtained. This would be of interest to further our understanding about the mechanisms responsible for drag generation and how these relate to spatial pressure fluctuations and large-scale motions above the canopy layer.

Given the lack of a suitable direct measurement method, pressure reconstruction from PIV stands as a promising tool. Introduced by Gurka et al. (1999), who estimated the average pressure fields of an impinging jet and of a channel flow, it quickly became popular for its potential to provide an integral description of the flow dynamics. At present, numerous variations of this technique have been proposed for planar, stereo or volumetric data, uncorrelated or time-resolved, using Eulerian (EU) or Lagrangian (LA) approaches. A review by Van Oudheusden (2013) details the operating principles and implementation aspects of these methods. He further discusses their intrinsic limitations arising from the seemingly chaotic motions of turbulent flows, and highlights the dominant factors that influence their accuracy, namely, the quality of the velocity-source data and their spatial and (if applicable) temporal resolutions. The Eulerian computation for convective flows using Taylor's hypothesis (TH), introduced by de Kat and Ganapathisubramani (2013), overcomes the requirement for time information to obtain estimates of the instantaneous pressure gradient. In this special case, performance is subject to the measurement of a convection velocity rather than the temporal resolution (Krogstad

et al., 1998; Laskari et al., 2016).

Snapshot planar-PIV for uncorrelated in-plane velocity measurements has become widespread, but its potential for pressure reconstruction is essentially restricted to (quasi-)2D turbulence, when the contribution of out-of-plane motions to the transport of momentum is negligibly small. Yet, despite this detrimental aspect, some applications (e.g. industrial measurements) would largely benefit from full-field pressure estimations, even if the flow is not strictly two-dimensional. This premise has recently motivated the work of Van der Kindere et al. (2019), who quantified the accuracy of two PIV-based reconstruction methods using in-plane velocity data (2D-EU and 2D-TH), and how they perform against equivalent, time-resolved 3D approaches. They showed that, for a turbulent boundary-layer, using 2D-TH produces comparable results with those of a 3D-EU approach for higher noise levels in velocity data, and that pressure statistics are typically insensitive to the third spatial dimension. Furthermore, they achieved an agreement to within 4% ($\approx 2\,\mathrm{Pa}$) in the mean surface pressure over a forward-backward facing step with data from an array of surface-mounted transducers, and $10-15\%$ in the root-mean-square (RMS) pressure. The correlation coefficient between the estimated and the reference pressure signals is approximately 0.5. In view of their analysis, employing these techniques towards understanding and modelling the flow processes in urban areas is a natural step.

In this study, static-pressure fields over two staggered arrays of cuboids are inferred from in-plane velocity data, using 2D-RANS and 2D-TH, by neglecting the contribution of the out-of-plane motions. This is especially detrimental within the canopy layer, where the flow is highly three-dimensional. Although empirical analysis suggest that the error induced by the missing terms is potentially the primary source of uncertainty, it cannot be readily quantified. The performance of the reconstruction methods is then examined following a *type-B* evaluation strategy: First, by comparing the mean surface pressure distribution against reported wind tunnel measurements (Claus et al., 2012b) and numerical simulations (Claus et al., 2012a; Leonardi and Castro, 2010). Secondly, by estimating the values of friction velocity U_τ and zero-plane displacement d based on the reconstructed pressure field. The pressure distribution is therefore assumed to be uniform along the spanwise direction, which, according to measurements of Cheng et al. (2007), is a reasonable approximation over nearly 70% of the width of the cuboids.

3.2 Experimental methods

Experiments were conducted in the open-return, suction wind tunnel at the University of Southampton. This facility features a 7:1 contraction followed by a closed working section, $4\,\mathrm{m}$ long with cross section $0.9\,\mathrm{m}$ wide and $0.6\,\mathrm{m}$ high. Boundary layers are established directly on the wind tunnel floor, following the contraction. The freestream
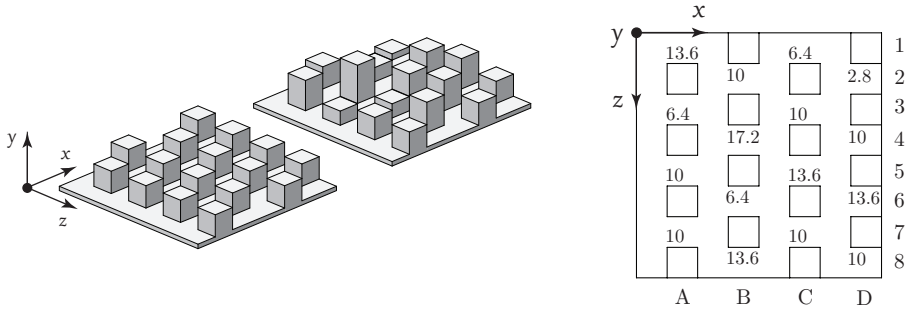
FIGURE 3.1: ILLUSTRATION OF THE ROUGH SURFACES. On the left, perspective view of the tiles which make up each surface roughness. On the right, the plan view of the staggered array including the heights of each individual element in mm for the case with a random height distribution. Elements are identified by means of an alphanumeric grid, displayed on the right and bottom sides. The XX axis indicates the principal flow direction.

turbulence intensity has been reported to be homogeneous and lower than 0.5% at the measurement location (Claus et al., 2012b; Placidi and Ganapathisubramani, 2018), and the flow develops in nominally zero-pressure gradient. The walls of the test section are optically transparent, to facilitate using imaging techniques (e.g. PIV), and the floor is cut out to fit a floating element (FE) balance. This work follows the convention that x, y, z are respectively the streamwise, wall-normal and spanwise directions; u, v, w, are the corresponding velocities in those directions.

We consider two rough surfaces, illustrated in figure 4.1: a staggered array of cubes with uniform height (C10U) and an array of cuboids with the same plan arrangement but a variable height distribution (C10R), the standard deviation is 3 mm (further details regarding its design can be found in Cheng and Castro, 2002). Both arrays have the same mean height $H = 10$ mm and a planar solidity fraction $\lambda_p = 0.25$ (defined as the ratio between the plan area of the obstacles and the floor area of a repeating unit). This particular kind of surface topology is often referred to as urban-like roughness because it shares similar features with urban environments. Particularly, the regular shape of the obstacles/buildings and the long street canyons, which, in this case, span across the wind tunnel. Cheng and Castro (2002), Reynolds and Castro (2008) and Claus et al. (2012b) have previously investigated the boundary-layer flow developing over these surfaces, under similar test conditions. They provide measurements of the vertical profiles of the mean streamwise velocity and of higher order statistics, obtained via cross-wire anemometry and Laser Doppler Velocimetry (LDV). Reynolds and Castro (2008) additionally acquired snapshots of the velocity field over cube roughness using planar PIV. Since the present measurements were found to be entirely in agreement with these studies, only the reconstructed pressure fields are shown in this chapter, of which there is no previous available experimental data.
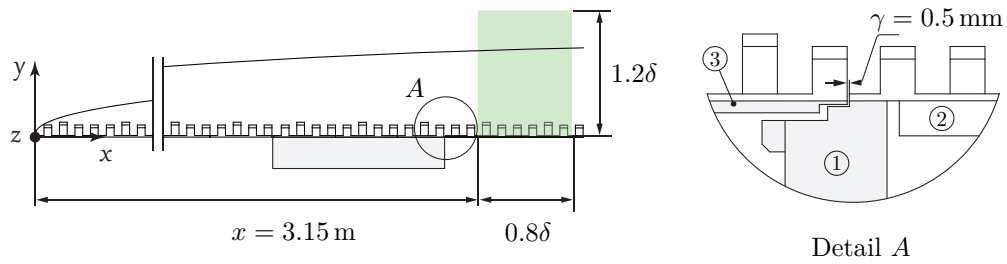
FIGURE 3.2: WIND TUNNEL SETUP. Schematic of a boundary layer developing over the rough surface. The FE (gray) is located 3.3 m downstream of the contraction. A detail of the floating-to-fixed surface joint is given on the right, where (1) is the casing of the balance, (2) is the wind tunnel floor and (3) is the sensing element. The field-of-view for the PIV is highlighted green and is located downstream of the balance.

3.2.1 Floating element

Wall shear stress is directly measured using the FE balance described in Ferreira et al. (2018). Its design is based on the parallel-shift linkage, featuring dedicated pairs of bending-beam transducers to monitor not only the streamwise load but also the induced pitching moment, as a means to decouple extraneous loads. The FE itself is a 200-mm-side square that is small enough in relative terms to ensure local measurements of wall shear stress. The balance is flush mounted with the wind tunnel floor, roughly 3.0 m downstream of the contraction, as depicted in figure 3.2. Special care was exercised mounting the surrounding tiles of the FE, given the tight tolerance of the fix-to-floating surface joint that is only $\gamma = 0.5$ mm wide. It is emphasised that the dimensions of the FE are not a multiple of a tile-size, which is 80-mm-side square. Therefore, on the floating element, two complete tiles were placed at the centreline, one behind the other, the first flush with the leading edge. Adjacent tiles were then laser cut to fit within its plan area while the remaining pieces were mounted outside, creating a seemingly continuous surface. Having an incomplete set of tiles on the sensing element does not impact the measurement of wall shear stress over the cube roughness, since there still is an integer number of repeating units. For the 'random' height case (C10R), however, the tile itself is the repeating unit so obstacles in rows 1, 2, 7 and 8, and columns C and D, are underrepresented (refer to figure 3.1). This potentially introduces some bias error that is challenging to estimate, but from the relative number of obstacles left out to the total number within 9 tiles covering the FE, we may assume their impact is not appreciable.

A total of 5 runs were performed in subsequent days for freestream velocities ranging between $U_0 = 10$ and $26 \, \text{ms}^{-1}$ in increments of $2 \, \text{ms}^{-1}$. Each acquisition lasted 30 s at 150 Hz, equivalent to 2500 boundary-layer turnover times at the lowest operating speed. Pre- and post-calibrations were conducted for each configuration without notable discrepancies. The acquisition procedure and uncertainty analysis are detailed in Ferreira
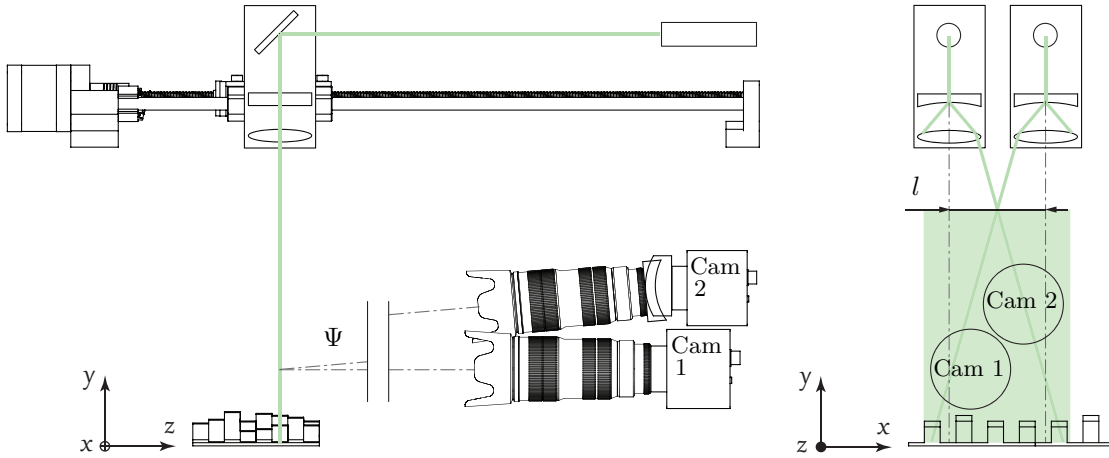
FIGURE 3.3: PIV SETUP. Lasers were placed above the test section. Two sets of optics and mirrors were mounted on a spanwise traverse, which allowed to simultaneously displace the light sheets to predetermined locations. The cameras were mounted on two-dimensional linear translation stages, outside the wind tunnel. One of them featured a Scheimpflug adapter to adjust the plane of focus to the image plane by $\Psi \simeq 10°$. The streamwise distance between the laser beams l ensures the entire canopy region is illuminated.

et al. (2018).

3.2.2   Particle image velocimetry

Measurements of the flow field that developed over each surface were acquired using planar PIV in the streamwise wall-normal plane. For the case of uniform height, the measurements were taken at 3 different spanwise locations (on the side of the cube, 1/4 cube and centre cube) to spatially average the flow across a repeating unit. Given the height variability of the second surface roughness, we considered instead 8 spanwise locations matching the centreline of the obstacles numbered according to figure 3.1. The field-of-view (FOV) is located behind the FE, as shown in figure 3.2. This development length was verified to be sufficient for the flow to establish a constant shear-stress layer above the canopy and to reach fully rough conditions at a fixed freestream velocity of $U_0 = 10\,\mathrm{ms}^{-1}$; $Re_\tau|_{\mathrm{C10U}} = 5300$ and $Re_\tau|_{\mathrm{C10R}} = 6000$. Two laser/camera arrangements were setup depending on the surface roughness; figure 3.3 shows the schematic for the array of cuboids with a variable height distribution (C10R). The flow was seeded with $\approx 1\mu\mathrm{m}$ particles of a vaporised solution of glycol-water. Two Litron $200\,\mathrm{mJ}$ dual pulse Nd:YAG lasers were used to illuminate the particles via a system of mirrors and $50\,\mathrm{mm}$ cylindrical lenses, which steer and expand the laser beams into sheets with a thickness no larger than $1\,\mathrm{mm}$. The set of optics was mounted on a traverse that enabled accurate displacement of the light sheets in the spanwise direction to predetermined locations. The streamwise distance between them l was adjusted to eliminate the shadows cast by

the obstacles in the canopy. Two LaVision Imager Pro LX 16MP cameras, each equipped with 200 mm $f/8$ Nikon lenses, allowed a FOV 0.8δ wide and 1.2δ high (in terms of mean roughness height, $9H \times 14H$). Both cameras share the same FOV, but have different viewpoints to overcome the lack of optical access within the canopy. Due to space restrictions, one of them was fitted with a Scheimpflug adapter to adjust its plane of focus (the angle of the image plane relative to the plane of focus $\Psi \simeq 10°$). The setup of the cube roughness (C10U) employed a single camera and a laser in similar fashion as described above. For each test case, 2500 image pairs were recorded at a fixed frequency of 0.5 Hz, which is slow enough to safely assume statistical independence between them. The images were correlated in the pixel domain with LaVision Davis 8.2.2, using decreasing interrogation window sizes down to 16px×16px and an overlap of 75%. The instantaneous vector fields were then filtered using a 3×3 Gaussian kernel and finally scaled and mapped to real dimensions, resulting in an effective spatial resolution of approximately 0.35 mm. The average free-stream pixel displacement is 16 and the particle diameter larger than 2p. Following Benedict and Gould (1996), the linear estimates of the uncertainty associated with the mean values are $\overline{u}/U_0 = 0.28\%$, $\overline{v}/U_0 = 0.17\%$, with (co-)variances $\overline{u'u'}/U_0^2 = 0.054\%$, $\overline{v'v'}/U_0^2 = 0.020\%$ and $\overline{u'v'}/U_0^2 = 0.023\%$.

Stitching the vector fields

The vector fields for C10R were obtained by combining two independent dual-pulse lasers whose light sheets overlap over most part of the FOV, except in the canopy. Variations in light intensity are not expected to introduce any bias error, yet perfect alignment of the cameras and calibration of each individual FOV were paramount for stitching the instantaneous vector fields (Raffel et al., 2018). In the outer layer, the large particle image shift contributes to minimize the measurement uncertainty. However, near the wall values are likely to be biased to some degree due to spatial averaging of the particle motions within the interrogation windows, and from potential mismatches between the mapping functions of each camera. The effect of error propagation is evident in figure 3.4, by examining the boundary of the overlapping region surrounding the obstacles. It is possible to observe a slight discontinuity in the unfiltered velocity map along the black contourline. The Gaussian filter successfully removes this inconsistency, which does not seem to appear up to higher order statistics. The stitching algorithm uses a modified *tapered-cosine window* as the weighting function to ensure a smooth transition across the wall-normal boundaries of the overlapping region. It consists of two half-cosine lobes of width $\alpha N/2$ convoluted with a rectangular window of width $(1 - \alpha)N$, where N is the number of overlapping vectors in the streamwise direction and $\alpha = 0.3$.
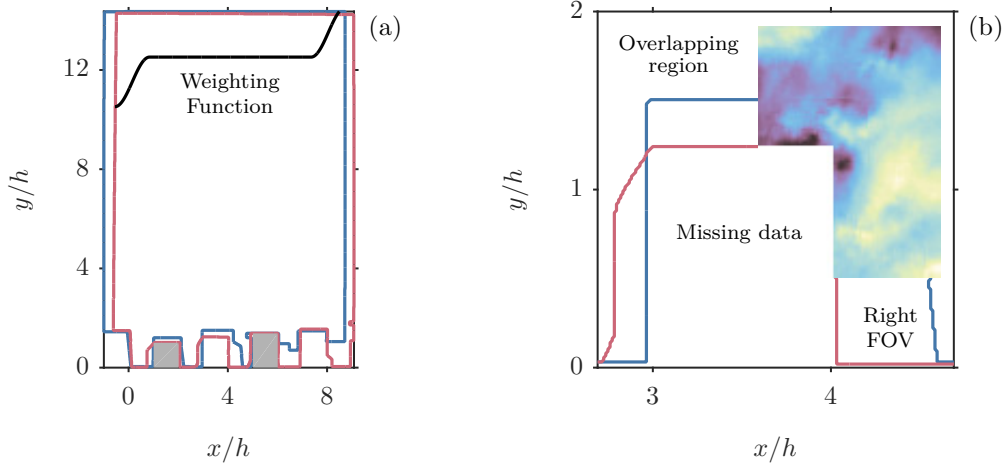
FIGURE 3.4: STITCHING SCHEME. **(a)** The composite FOV and illustration of the weighting function in the overlapping region. The red and blue lines indicate the contour of the vector fields of the right and left cameras, respectively; obstacles in the image plane are highlighted gray. **(b)** Detail of the unfiltered velocity map showing the discontinuity across the blue contourline.

3.2.3   Pressure estimation

The numerical framework for pressure reconstruction methods has been outlined by numerous authors, so we only present here the general expressions for those employed in the current study, 2D-RANS and 2D-TH. The reader is referred to Van Oudheusden (2013) and Laskari et al. (2016) for an in-depth explanation of the theoretical background, uncertainty analysis and implementation.

2D-RANS: Time-averaged pressure fields were estimated from PIV data using a Poisson formulation of the Reynolds-averaged Navier-Stokes (RANS) equation, and assuming a divergence-free flow. Accordingly,

$$\nabla^2\bar{p} = -\rho\nabla \cdot \{\bar{\mathbf{u}} \cdot \nabla\bar{\mathbf{u}} - \nu\nabla^2\bar{\mathbf{u}} + \nabla\boldsymbol{R}(\mathbf{u}', \mathbf{u}')\}. \tag{3.1}$$

where $\mathbf{u} = \bar{\mathbf{u}} + \mathbf{u}'$ is the velocity vector field, $\bar{p}$ is the average pressure field, $\boldsymbol{R}$ is the Reynolds stress tensor, ρ is the density of the fluid and ν its kinematic viscosity. Equation 3.1 was spatially integrated by means of a Poisson solver, designed based on the work of De Kat and Van Oudheusden (2012) (velocity gradients are determined using a central difference scheme). Boundary conditions were enforced all around the domain of integration: along the top edge, which lies in the freestream, pressure values were prescribed by a modified Bernoulli equation to account for traces of turbulent kinetic energy. Around the roughness obstacles and on the vertical boundaries of the integration region, the pressure gradient was instead imposed via Neumann conditions. The freestream reference pressure $\bar{p}_0$ was measured with a pitot-static probe mounted

at the same downstream location as the FOV.

2D-TH: A crucial aspect in determining instantaneous pressure fields from velocity information is the correct estimation of the material acceleration in the Navier-Stokes equation. For incompressible flows, and taking an Eulerian frame of reference, the latter may be written as follows

$$\frac{\partial \mathbf{u}}{\partial t} + (\mathbf{u} \cdot \nabla)\mathbf{u} = -\frac{1}{\rho}\nabla p + \nu\nabla^2\mathbf{u}. \tag{3.2}$$

Although most terms in equation 3.2 can be readily computed from snapshot PIV, the lack of temporal resolution impedes a complete description of the fluid motion. This is traditionally achieved with time-resolved measurements of the velocity field, using high-end imaging equipment or multiple-exposure techniques. Alternatively, de Kat and Ganapathisubramani (2013) proposed using Taylor's "frozen turbulence" hypothesis to approximate the motion of a perturbation (i.e. turbulent eddy) relative to the local mean as one of convection, thus relaxing the acquisition requirements. The time derivative of a velocity fluctuation then reads

$$\frac{D\mathbf{u}'}{Dt} = \frac{\partial \mathbf{u}'}{\partial t} + (\mathbf{u_c}.\nabla)\mathbf{u}' = 0, \tag{3.3}$$

where $\mathbf{u_c}$ is the local convection velocity vector. After substitution into (3.2), this yields an expression independent of the time derivative

$$\nabla p = -\rho\{[(\mathbf{u} - \mathbf{u_c}) \cdot \nabla]\mathbf{u} + (\mathbf{u_c} \cdot \nabla)\overline{\mathbf{u}} - \nu\nabla^2\mathbf{u}\}. \tag{3.4}$$

The underlying assumption behind TH is that the time scale of a turbulent field is larger than the time scale of its advection downstream. This is typically true for convective flows, as in the case of grid-generated decaying turbulence, where turbulent eddies of different sizes are convected together with the local mean. In wall-bounded flows, however, turbulent structures have different characteristic transport velocities depending on the position within the boundary layer and on the scale and type of event (Krogstad et al., 1998), posing a practical challenge to accurately measure $\mathbf{u_c}$. Incidentally, researchers have often found the mean field to be a sensible estimate, yielding reasonable results at least for channel flows (see e.g. Geng et al., 2015, Laskari et al., 2016) and forward-backward facing steps (Van der Kindere et al., 2019). Following this approach, $\mathbf{u_c} = \overline{\mathbf{u}}$, and the Poisson formulation of equation 3.2 becomes

$$\nabla^2 p = -\rho\nabla \cdot \{(\mathbf{u} \cdot \nabla)\mathbf{u} - (\overline{\mathbf{u}} \cdot \nabla)\mathbf{u}' - \nu\nabla^2\mathbf{u}\}. \tag{3.5}$$
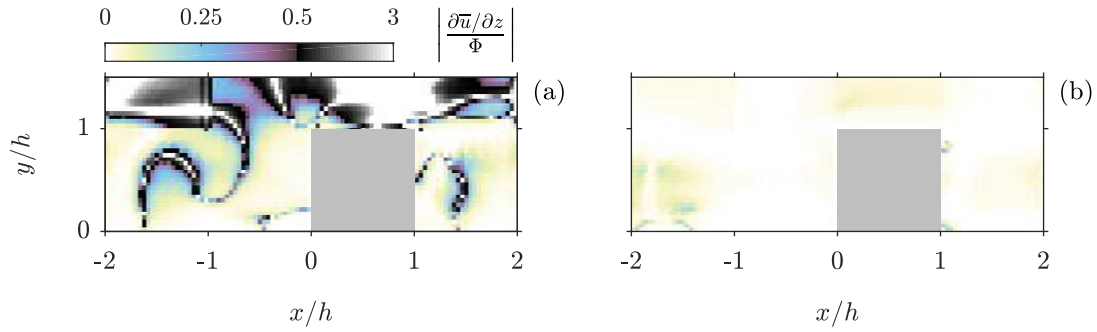
FIGURE 3.5: THE MISSING NON-LINEAR CONVECTIVE TERMS. Relative magnitude of the in-plane and out-of-plane streamwise velocity gradients within the canopy of a staggered-cube array, from large eddy simulation (LES) data of Xie and Castro (2006). **(a)** $\Phi = \partial\overline{u}/\partial x$ and **(b)** $\Phi = \partial\overline{u}/\partial y$. Values larger than 0.5 are highlighted red.

Similarly to *2D-RANS*, equation 3.5 is integrated by means of a Poisson solver[1] with finite differences. Dirichlet boundary conditions are imposed in the freestream along the top edge, where pressure values are prescribed by $p = \overline{q}_0 - (\rho/2)(u^2 + v^2)$, and Neumann boundary conditions elsewhere.

Implications of planar-PIV

The uncertainty associated with PIV-based pressure estimation is primarily related to the quality and nature of the velocity data. As explained by Van Oudheusden (2013), unless the flow is purely two-dimensional (2D), out-of-plane motion must be accounted for in the governing equations whether planar or volumetric pressure fields are to be extracted. In a statistical sense, the outer region of the boundary layer which develops over these surfaces may be treated as 2D, in which case neglecting 3D terms does not affect the accuracy of the estimation. Near the wall, however, the flow is dynamically influenced by the roughness length scales, giving rise to dispersive stresses. Especially within the canopy, where the flow meanders around the obstacles, strong out-of-plane motions are expected. There have been some attempts to circumvent the lack of 3D information in planar PIV (Haigermoser, 2009; Baur, 1999), but so far it appears that modifications to existing methodologies alone do not yield significant improvements (Van Oudheusden, 2013). Therefore, additional effort would be necessary to resolve the missing components of velocity and acceleration (e.g. with Tomographic PIV or 3D particle tracking velocimetry).

Quantifying the error introduced by this approximation is nontrivial, as it requires a priori knowledge of the flow conditions. Sensitivity studies (Charonko et al., 2010; De Kat and Van Oudheusden, 2012) have shown, nonetheless, that a small to moderate degree of out-of-plane motion does not seriously affect the pressure field estimation,

---

[1]The source code can be found in `https://git.soton.ac.uk/bharath-lab/piv-based-pressure-estimation`.

provided a global integration approach such as a Poisson solver is used — the error within the canopy is diffused into the outer region where the flow is effectively 2D. The impact of 3D flow motion on planar reconstruction was further investigated by McClure and Yarusevych (2017). They found that for fully turbulent regimes, the relative error in the near wake of a cylinder does not exceed 5%, but can grow larger than 20% farther downstream, as turbulence becomes increasingly homogeneous (and in-plane vorticity emerges). On the basis of these and previously existing empirical analysis (e.g. De Kat and Van Oudheusden, 2012), they concluded that planar methods are generally applicable if the out-of-plane gradients are less than half of in-plane velocity gradients, from which point the accuracy of the estimation rapidly decays. To assess this criteria, we use the LES data set of Xie and Castro (2006) to compute the relative magnitude of the mean velocity gradients at the centreplane of a cube, shown in figure 3.5 for the streamwise component. It is clear that $\partial \overline{u}/\partial z$ is consistently smaller than $\partial \overline{u}/\partial x$ or $\partial \overline{u}/\partial y$ by one order of magnitude, occasionally exceeding the aforementioned threshold. The uncertainty associated is then expected to remain at acceptable levels in the region of interest. Naturally, above the canopy the streamwise gradient approaches zero causing the ratio to suddenly diverge.

Additional error sources and noise propagation

Besides the lack of spatial information, 2D-TH formulation is intrinsically sensitive to regions of intense shear and turbulence intensity. This is partly due to the limited spatial resolution of the PIV system but, more importantly, because the basic assumptions of TH are unlikely to hold. This limitation was recently investigated by Van der Kindere et al. (2019) for a turbulent-boundary layer flow past a wall-mounted rib. TH appeared to perform reasonably well over most part of the FOV, except in the vicinity of the shear layer shed off from the leading edge and in the wake region, where the mean velocity is considerably lower than the local fluctuations. In light of these result, they suggested $|\mathbf{u_{rms}}|/|\overline{\mathbf{u}}| \cdot \overline{\omega} H/U_0 > 10$ to be a suitable performance indicator for 2D-TH, where $\overline{\omega}$ is the mean out-of-plane vorticity and H the obstacle height. Accordingly, using the mean roughness height as the length scale to normalise vorticity, we expect TH to yield sensible results above the canopy. Values are typically less than 2 in the shear layer and below the canopy top, except in the vicinity of isolines of zero-velocity where it far exceeds the stipulated limit.

Noise propagation from velocity data was estimated following the procedure outlined by De Kat and Van Oudheusden (2012), which is derived from the approach to uncertainty analysis of Kline and McClintock (1953). For 2D-RANS, neglecting the contribution of the viscous term, the linear propagation of uncertainty applied to equation

[3.1](#) yields

$$\epsilon^2_{\overline{p}_{RANS}} \propto \epsilon^2_{\overline{\mathbf{u}}}\left(\frac{1}{2}|\overline{\mathbf{u}}|^2 + \Delta^2_{xy}|\nabla\overline{\mathbf{u}}|^2\right) + \frac{1}{2}\epsilon^2_{\overline{\mathbf{u'u'}}}, \tag{3.6}$$

where ϵ_Φ is the estimated precision error of the arbitrary quantity Φ and Δ_{xy} is the spatial resolution of the vector fields, listed in table [3.1](#). Note that equation [3.6](#) considers second-order central finite differences to estimate derivatives in space; truncation errors were not included in this analysis. For 2D-TH, [Laskari et al. (2016)](#) expressed the relative error propagation from velocity as

$$\epsilon^2_{p_{TH}} \propto \epsilon^2_{u_c}\left(\Delta^2_{xy}|\nabla\mathbf{u'}|^2\right) + \epsilon^2_{\overline{u}}A^2_u +$$
$$+ \epsilon^2_u\left(\frac{1}{2}|\mathbf{u}-\mathbf{u_c}|^2 + \frac{|\mathbf{u'}|^2}{2} + \Delta^2_{xy}|\nabla\mathbf{u}|^2\right),$$

with

$$A_u = \epsilon_u\sqrt{\frac{1}{2}|\mathbf{u}-\mathbf{u_c}|^2 + \Delta^2_{xy}|\nabla\mathbf{u}|^2} +$$
$$+ \epsilon_u\sqrt{\frac{1}{2}|\mathbf{u}|^2 + \Delta^2_{xy}|\nabla\mathbf{u}|^2} + \epsilon_u\sqrt{\Delta^2_{xy}|\nabla\mathbf{u}|^2}. \tag{3.7}$$

We estimate $\epsilon^2_{\overline{p}_{RANS}}$ to be on the order of 2% around the shear-layer interface and in the region immediately above, where turbulence intensity is highest (refer to [Cheng and Castro, 2002](#)). Within the canopy, it becomes noticeably smaller (less than 1%). Lastly, to determine $\epsilon_{p_{TH}}$, we assume the uncertainty on the local convection velocity $\epsilon_{u_c} \approx 3\%$, yielding an average relative error in pressure of about 1.2%.

3.3   Analysis of the pressure fields

Mean pressure maps, reconstructed from velocity data using 2D-RANS are shown in figures [3.6a](#) and [3.7](#), expressed non-dimensionally by the pressure coefficient $C_{\overline{p}} =$

TABLE 3.1: Uncertainty budget from RMS errors at $(1.5h, h)$ for C10U and $(4.5H, 17.2H)$ for C10R streamwise alignment 3. $\overline{\mathbf{u}}$ and $\mathbf{u_c}$ are normalised by U_0, and $\overline{\mathbf{u'u'}}$ by U_0^2. Uncertianty in $\mathbf{u}$ is given by the typical bias error in pixel displacement.

	ϵ_Φ	C10U	C10R
2D-RANS	$\overline{\mathbf{u}}$	$\{1.5, 1.0\}$	$\{1.1, 0.65\}$
	$\overline{\mathbf{u'u'}}$	$\{0.120, 0.025\}$	$\{0.30, 0.035\}$
2D-TH	$\mathbf{u}$	0.1p	—
	$\mathbf{u_c}$	3.0	—
	Δ^+_{xy}	15	

$(\overline{p} - p_0)/q_0$, where q_0 is the freestream dynamic pressure; the flow direction is from left to right. Within the canopy, the pressure field is governed by the presence of roughness obstacles. High pressure regions generally develop on the upper half of the windward side, where the mean streamwise velocity is highest. On top, a low pressure region reveals the existence of a shear layer shed off the sharp leading edge that is essentially stronger for tall isolated obstacles. The pressure is quickly recovered downstream, suggesting that the total force acting on the cuboids is predominantly influenced by the pressure distribution on the windward side. Effects of mutual sheltering are particularly visible over C10R (figure 3.7), whereby the pressure surrounding the smallest obstacles is markedly modified. Above the canopy, the pressure field is mostly uniform and takes on the value of the local freestream static pressure $p_0 \simeq 0$.

The absolute difference between estimates obtained with 2D-RANS and 2D-TH, averaging over 2500 snapshots of the pressure field, is given in figure 3.6b for C10U. Discrepancies are most significant around the bottom-left corner, reaching 20% of the largest pressure value, but appear to be confined to a small region of the FOV. They presumably emerge from noise propagation and the sensitivity of the Poisson solver to Neumann boundary conditions. Along the edge surrounding the obstacles, which is typically 0.5 mm off the wall, both methods produce similar results. In fact, the spatially-averaged absolute difference $\langle |C_{\overline{p},\mathrm{RANS}} - C_{\overline{p},\mathrm{TH}}| \rangle$ is only 0.0038, comparable to values reported by Van der Kindere et al. (2019). Despite having been inferred from distinct PIV data sets, the pressure fields over C10R agree at least qualitatively with each other, in the sense that the higher pressure regions pertain to the tallest obstacles (figure 3.7). They are also not significantly affected by the mask of spurious vectors (in white), except for (d) and (g), where there seems to exist a local artificial decrease of the pressure value in-between the mask of the out-of-plane obstacles (at $x/H = 3.5$ and 4.5, respectively).

3.3.1 Drag profiles and pressure fluctuation

To assess the performance of the pressure estimation, we examine the normalised axial-pressure difference across selected obstacles $\Delta\overline{p}(y) = \overline{p}_w(y) - \overline{p}_l(y)$, where the subscript identifies the windward (w) and leeward (l) faces, represented in figures 3.8a and 3.9. Available experimental measurements (Cheng and Castro, 2002) and numerical solutions (Claus et al., 2012a; Xie et al., 2008; Leonardi and Castro, 2010) were included for reference, revealing a notable collapse in spite of the inherent uncertainty of the reconstruction methods. Around the mid-canopy height of C10U, the agreement is generally better than $0.1\langle\Delta\overline{p}\rangle$, but it worsens near the wall. There, a low pressure level is maintained by the recirculating region that develops ahead of the cube, so $\Delta\overline{p}$ is relatively small. It then grows larger away from the wall, reaching a peak for $y > 0.8h$. Leonardi and Castro (2010) showed that, for staggered cube arrays, the peak-to-peak
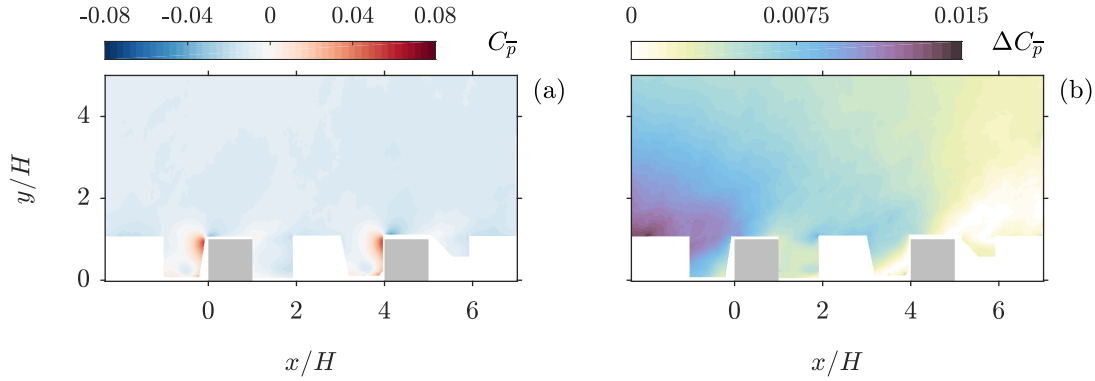
FIGURE 3.6: PRESSURE WITHIN THE CANOPY OF C10U. **(a)** The normalised mean pressure field reconstructed from planar-PIV on the vertical centreplane of the obstacles using 2D-RANS, and **(b)** the absolute difference between the estimates obtained with 2D-RANS and 2D-TH. The pressure coefficient $C_{\overline{p}} = (\overline{p} - p_0)/q_0$, where q_0 is the freestream dynamic pressure. Obstacles in the measurement plane are highlighted gray.

amplitude increases with packing density, as the shear-layer interface between the canopy and the flow aloft becomes gradually more prominent. Presumably, a similar effect would result from an increase of the roughness Reynolds number based on the mean height $H^+ = U_\tau H / \nu$, which is somewhat lower for computations than it is in this experiment. Since the peak-to-peak amplitude is smaller with 2D-RANS, discrepancies in local extrema likely arise from uncertainties, both in the measurements and numerical solutions. $C_{p_{rms}}$ profiles are shown in figure 3.8b. Pressure fluctuations are most intense around the stagnation region, on the windward side close to the canopy top, reaching nearly 50% of the local mean pressure value, and become less significant towards the wall. On the leeward side, $C_{p_{rms}}$ is mostly uniform and relatively small, which reflects the existence of a low momentum region that extends across the canopy height.

Estimates of drag profiles for three cuboids within C10R are compared in figure 3.9a against LES data from Xie et al. (2008). We emphasise that the simulation was performed over a geometrically identical array, but the flow is in the opposite direction. Despite this important caveat, their results are still consistent with the current measurements, suggesting that the pressure field is hardly affected by the local height distribution. This is true, at least, for staggered and aligned arrays, provided the plan solidity fraction $\lambda_p \leqslant 0.25$ — conditions which minimise transverse wake interaction. The agreement between drag profiles is best for the shortest obstacle (8-A). So it is reasonable to assume that effects of local Reynolds number become noticeable for taller obstacles, explaining, albeit not entirely, the reduced peak-to-peak amplitude from LES data (carried out at a lower H^+). Although the general shape of $\Delta\overline{p}$ across the largest cuboids appears to be preserved, figure 3.9b shows that it is markedly different for those lying in their wake. Results of Xie et al. (2008) confirm this observation, but they only
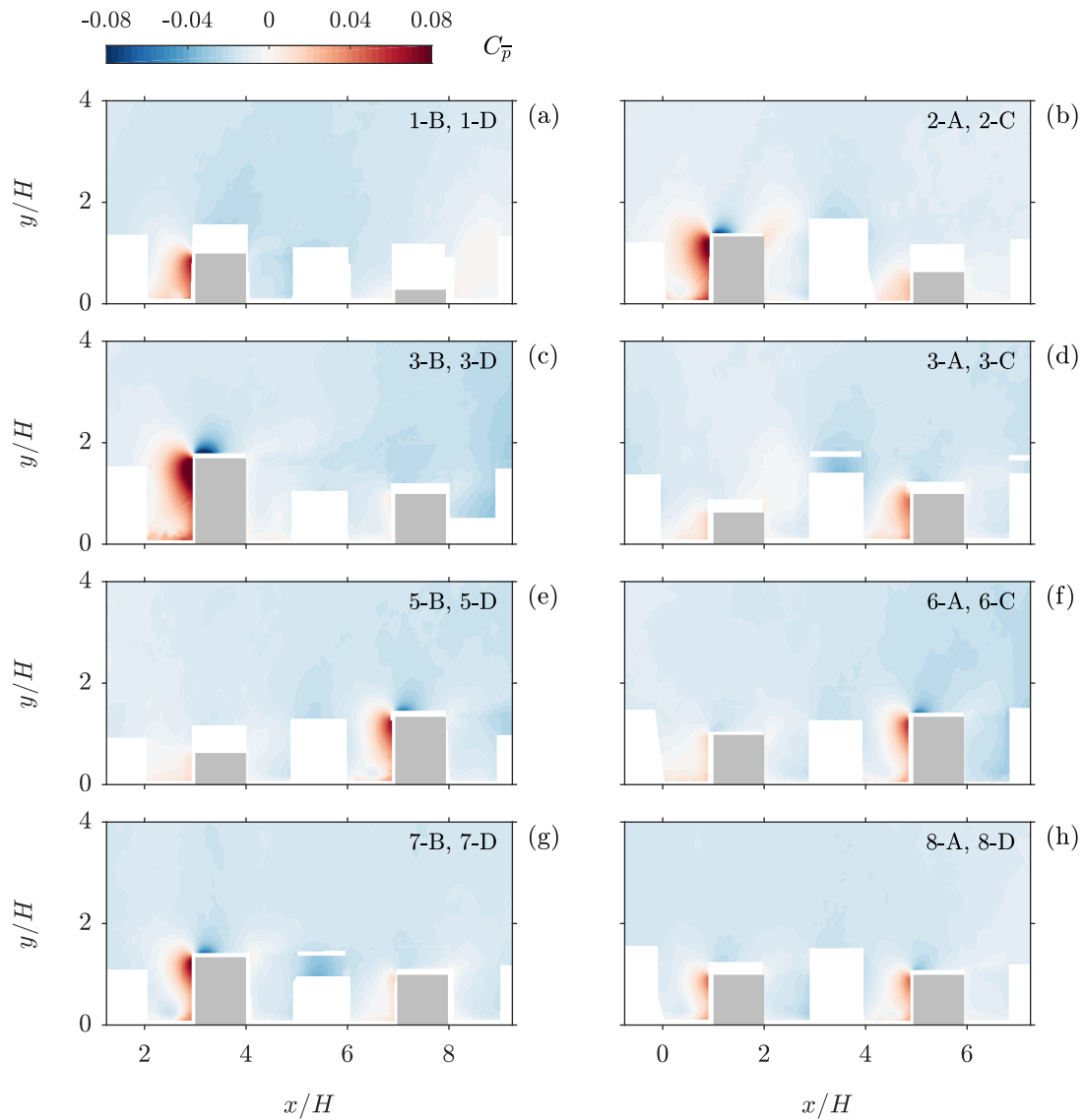
FIGURE 3.7: PRESSURE WITHIN THE CANOPY OF C10R. Normalised mean pressure fields obtained using 2D-RANS at each streamwise alignment, 1 to 8, as outlined in figure 4.1. x-coordinate is referenced to the leading edge of the roughness tile. Obstacles in the measurement plane are highlighted gray.
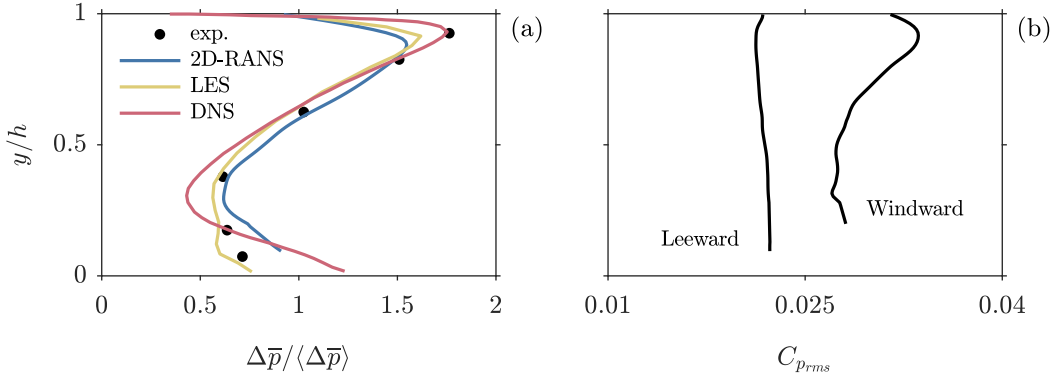
FIGURE 3.8: STATISTICS OF SURFACE PRESSURE OVER C10U. **(a)** Axial-pressure difference across a roughness element, normalised by the vertically-integrated value. Measurements of a pressure-tapped obstacle by Cheng and Castro (2002) (black circles) and numerical solutions by Claus et al. (2012a) (LES) and Leonardi and Castro (2010) (direct numerical simulation (DNS)) were included for reference. **(b)** $C_{p_{rms}}$ on the windward and leeward sides of a cube, obtained with 2D-TH.

identify the shortest obstacles ($0.64H$ and $0.28H$ high) to have distinct $\Delta\overline{p}$ distributions, while the present data show that for each streamwise alignment the shorter one does not share the usual drag profile, regardless of its height.

3.3.2   Boundary-layer flow parameters

Neglecting the viscous contribution to wall-shear stress, we attempt to estimate the friction velocity U_τ over C10U and C10R from pressure data. The results are compared against FE measurements, listed in table 3.2, to ascertain the performance of the reconstruction methods in the canopy layer. Additional estimates were included for reference, specifically those inferred from cross-wire anemometry of the boundary-layer profile by Cheng and Castro (2002), over identical obstacle arrays, and from a pressure-tapped cube (C10U) by Claus et al. (2012b).

The form drag of individual obstacles F_i is obtained by integrating the axial-pressure difference over their cross sectional area $h_i \times w$, assuming a spanwise-uniform distribution and a zeroth-order (constant) extrapolation of the pressure value at the edge of the domain down to the wall. The surface shear stress is then estimated considering the total drag within the plan area of a repeating unit S. Accordingly,

$$F_i = w \int_0^{h_i} \Delta\overline{p}_i \, dy, \tag{3.8}$$

and

$$U_\tau^p = \left(\frac{1}{\rho S} \sum_{i=0}^{n} F_i \right)^{1/2}. \tag{3.9}$$

The results, listed in table 3.3, are consistent with direct measurements of wall-shear
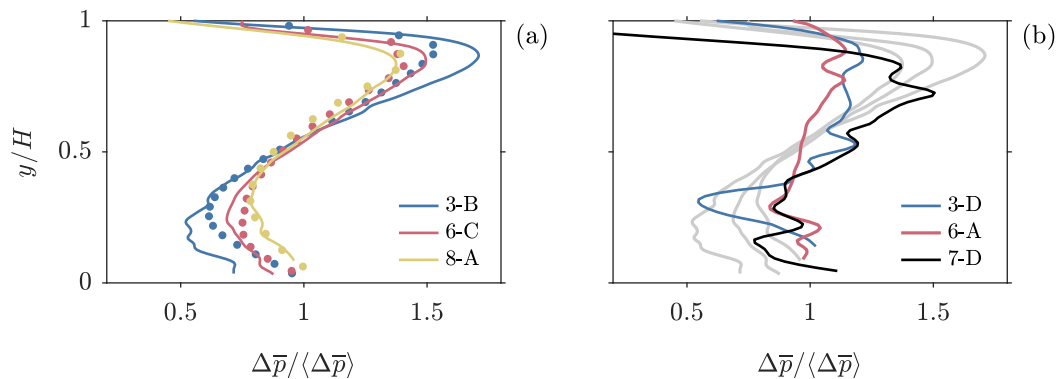
FIGURE 3.9: NORMALISED DRAG PROFILES OF SELECTED CUBOIDS IN C10R. **(a)** Results from pressure reconstruction using 2D-RANS (solid lines) are compared with LES data from Xie et al. (2008) (circles). Obstacles, 3-B, 6-C and 8-A (refer to figure 4.1) are, respectively, $1.71H$, $1.36H$ and $1H$ high. **(b)** Illustrates the marked difference between the profiles represented in (a) and those of shielded obstacles (3-D, 6-A, 7-D). Colors identify different streamwise alignments.

stress using the FE balance (table 3.2). The relative discrepancy between them does not exceed 3.7% with 2D-RANS and 7% with 2D-TH (C10U). Marginally lower pressure-based values are expected as the frictional drag is not accounted for, yet the inherent uncertainty level frustrates any attempt to quantify its contribution. Especially considering that U_τ^p relies on information at the vertical centreplane of the cuboids alone and, thereby, is likely overestimated. The total stress method appears to systematically under-predict the friction velocity, which could either result from the lack of a fully-developed equilibrium layer or, as Womack et al. (2019) recently argued, due to a small favourable pressure gradient imposed by the fixed cross-section of the wind tunnel facility.

The zero-plane displacement d could also be determined following the theoretical arguments of Jackson (1981), who proposed that the vertical origin of the boundary layer is given by the centroid of the distributed drag. This reads,

$$d^p = \left(\sum_{i=1}^{n} \int_0^{h_i} w y \Delta \overline{p}_i \, dy \right) \bigg/ \left(\sum_{i=1}^{n} F_i \right). \tag{3.10}$$

For the uniform array, values of zero-plane displacement agree with pressure tap measurements by Cheng et al. (2007) ($d^p = 0.612H$) and Claus et al. (2012b) ($d^p = 0.56H$), as well as with DNS data by Leonardi and Castro (2010) using pressure-based ($d^p = 0.617H$) and log-law fitting methods ($d = 0.645H$). Note that Cheng et al. (2007) also present estimates obtained via a modified Clauser chart using U_τ inferred from the total-stress method, all of which are greater than $0.822H$. Additional estimates by Claus et al. (2012b) lie in the range $0.49H - 0.79H$, depending on the slope of the log-law — they compared multiple values of U_τ and, in some cases, treated the von Kármán

TABLE 3.2: Measurements of the friction velocity U_τ/U_0 (top) and the zero-plane displacement height d/H (bottom) from multiple sources. [1] Cheng and Castro (2002), [2] Xie et al. (2008), [3] Leonardi and Castro (2010), [4] Claus et al. (2012b).

	method	C10U	C10R
Present study	FE	$0.0651 \pm 1.7\%$	$0.0689 \pm 1.6\%$
	$\overline{u'v'}$ PIV	0.0614	0.0628
[1]	$\overline{u'v'}$ x-wire	0.0579	0.0644
[4]	$\overline{u'v'}$ PIV	0.0610	—
	Form drag	0.0678	—
[1]	Clauser	$0.86 - 1.16$	$1.19 - 1.36$
[2]	Clauser	—	1.20
[3]	Form drag	0.617	—
	Clauser	0.645	—
[4]	Form drag	0.560	—
	Clauser	$0.490 - 0.79$	—

coefficient κ as a fitting parameter. The marked discrepancy between reported values indicates that the uncertainty associated with indirect methods is in fact larger than is usually reported, impeding for example a definite conclusion on the validity of Jackson's Hypothesis.

The influence of height variability on surface roughness was systematically investigated by Jiang et al. (2008), Hagishima et al. (2009), and Millward-Hopkins et al. (2013), invariably leading to an increase of wall-shear stress and zero-plane displacement. Accordingly, the current results show an increase by 5.8% (8% from pressure data) of U_τ, followed by a corresponding increment in d of 18.7%. Cheng and Castro (2002) and Xie et al. (2008) examined the boundary-layer flow over C10R and found the zero-plane displacement height to fall within $1.19H - 1.36H$, from the mean streamwise velocity profile. These values are substantially larger than our estimate, but, notably, the pressure-based estimate obtained from LES data of Xie et al. (2008) ($d^p = 0.710H$) is consistent with the current analysis. Empirical relationships have been proposed by Jiang et al. (2008) (from LES data) and Millward-Hopkins et al. (2013) (using building data from a major UK city and a morphometric model) to express the influence of the height standard deviation upon the surface roughness parameters. They predict a relative increase in d from C10U to C10R of 33% and 40%, respectively.

TABLE 3.3: Boundary-layer parameters estimated from pressure data obtained using 2D-RANS and 2D-TH. The values within brackets indicate the relative difference from FE measurements.

		C10U	C10R
	h/δ_{99}	0.083	0.076
2D-RANS	U_τ^p/U_0	0.0627 (-3.7%)	0.0678 (-1.6%)
	d^p/H	0.619	0.735
2D-TH	U_τ^p/U_0	0.0605 (-7.0%)	—
	d^p/H	0.594	—
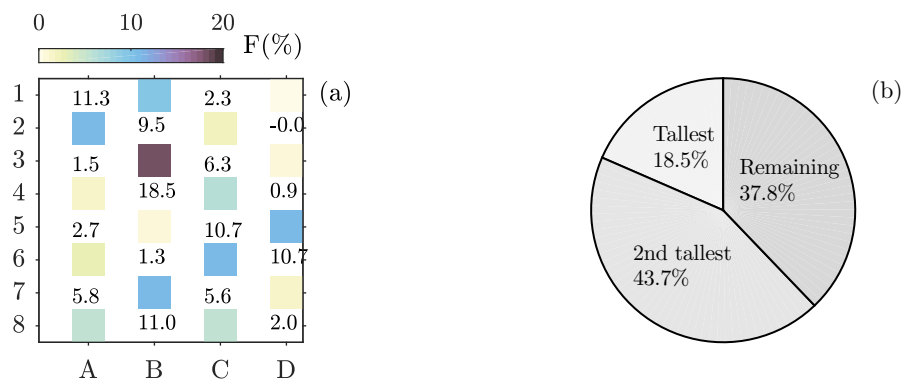
FIGURE 3.10: DISTRIBUTION OF SURFACE DRAG OVER A REPEATING UNIT OF C10R. **(a)** Plan-view, as given in figure 4.1, wind direction is from left to right. Each individual obstacle is color-coded according to the relative contribution to the total surface drag, obtained by integrating the axial pressure difference over the cross sectional area. Individual percentage contributions are written either above or below. **(b)** Pie chart illustrates the relative contribution to wall drag by the tallest obstacle ($1.72H$ high) and by the second tallest ($1.36H$ high).

3.3.3   Distribution of surface drag over C10R

Previous studies (Kanda, 2006; Xie et al., 2008; Millward-Hopkins et al., 2013) have shown that the distribution of the surface drag is dominated by the height variability of the roughness elements. Particularly over C10R, Xie et al. (2008) predicted that the percentage contribution of the tallest obstacle alone is 22.4%, despite its proportionate cross sectional area (10.8%), whereas the second tallest are responsible for 42.9% and the remaining obstacles for 34.7%. There are two reasons for this large disproportion: For one, form drag on obstacle arrays mostly arises from the upper half of the canopy, where the velocity is highest. Leonardi and Castro, 2010 found that the spatially-integrated mean axial velocity over the range $0.5 \leqslant y/h \leqslant 1$ is around 80% of the value integrated over the entire canopy height (for cube arrays with different density fractions). In fact, based on the profiles represented in figure 3.8a, roughly 67% of the pressure drag is exerted on the upper half. The second factor has to do with the height variability of the

surface roughness. Taller obstacles are not only exposed to higher momentum flow but also benefit from reduced wakes of neighbouring roughness elements, whose significance is, in turn, diminished. An equivalent analysis can be done using equation 3.8 to estimate the relative contribution to the total drag of individual roughness elements. Illustrated in figure 3.10a, the results show a remarkable quantitative agreement with findings of Xie et al. (2008). The load exerted by the fluid is fairly uniform for obstacles which stand above the mean canopy height. 2-A, 7-B, 6-C and 5-D protrude $0.36H$ and produce about the same form drag, in the range $9.5 - 11.3\%$. In contrast, the variability is increased for those which lie in sheltered regions. Depending on the local height distribution, $1H$-high obstacles experience loads from 0.9 (3-D) up to 9.5% (1-B) of the total surface drag.

3.4   Conclusion

We investigated the potential of using two-dimensional, PIV-based pressure reconstruction methods to achieve a more complete description of the flow field over two staggered arrays of cuboids (C10U and C10R). Empirical analysis suggest that the error induced by the missing out-of-plane components of velocity and acceleration could be problematic within the canopy layer, where the flow meanders around the roughness obstacles, however, it cannot be quantified without a priori knowledge of the flow conditions. So in order to assess the performance of this approach, surface pressure was extrapolated from the edge of the domain and compared against equivalent numerical and experimental studies. Overall, both 2D-RANS and 2D-TH yielded sensible estimates over the entire domain, showing minor discrepancies that should arise due to the sensitivity of the Poisson solver to boundary conditions. Estimates of the mean axial-pressure difference across individual elements showed a remarkable collapse with LES and DNS data, as well as with pressure-tap measurements. The RMS of the pressure fluctuations on the surface of a cube (C10U) was also obtained via 2D-TH, although it could not be validated against published results. This may potentially be explored to study, in a statistical sense, the relationship between the streamwise load applied on the roughness obstacles and the turbulent structure of the boundary layer above. It would then be beneficial to quantify the correlation coefficient between pressure values from PIV and reference transducer data on the surface. Lastly, the frictional velocity U_τ and the zero-plane displacement height d were inferred assuming a constant spanwise distribution of the surface pressure. Estimates closely match direct measurements using a FE balance and a pressure-tapped roughness obstacle. Discrepancies are at worst 7% in U_τ and 3.5% in d.

We conclude that pressure reconstruction from planar velocity data, using 2D-RANS and 2D-TH, has the potential to be a very useful tool in the study of urban boundary layers. It revealed a complex interaction between roughness elements, having different

drag profiles, depending mostly on the relative height distribution along the streamwise direction. This is reflected on the contribution to wall drag by individual elements that is largely disproportionate over C10R, some of which might even be thrust producing. This approach additionally stands as an alternative to direct measurement techniques when these are not available or cannot be easily employed (such is the case of C10R, whose repeating unit is comprised of 16 different elements), outperforming an ill-conditioned three parameter fit of the mean velocity profile or the total stress method. There are, nonetheless, some rather limiting aspects to bear in mind: For arbitrary-shaped obstacles (e.g. pyramids, cylinders, spheres) or arrays of cuboids at varying wind directions, the contribution of the spanwise components is likely to become important, resulting in a less accurate estimation in the canopy layer. It also requires highly spatially-resolved velocity maps and, since surface pressure is extrapolated from the closest available data point, performance is subject to laser reflections off the wall. Some of these shortcomings may be mitigated, however, using thin-volume tomographic PIV or a refractive-index matched facility.

Chapter 4

On the sectional-drag profile of urban-canopy layers

There have been significant efforts towards improving predictions of the canopy-drag of urban environments simply based on the surface geometry. Some of the most successful approaches are quasi-empirical formulations which typically treat urban agglomerates as a porous medium, thereby simplifying the governing equations. They necessarily make additional assumptions about the turbulent structure of the flow above and within the canopy that have always been target of intense scrutiny, in part because quality field and wind tunnel measurements are rather difficult to obtain, and few numerical simulations of large cube roughness have actually proved to be reliable. In this chapter, we investigate the mean-flow characteristics of the boundary layers that developed over C10U and C10R, in terms of velocity and pressure, and assess the adequacy of these assumptions. Profiles of normalised velocity defect and streamwise turbulence intensity showed a remarkable collapse with smooth-wall data at matching Re_τ, evidencing the presence of outer-layer similarity. Logarithmic regions were found to be fully immersed in the roughness sublayer for both surfaces, extending down to the height of the tallest obstacle. Although data in the canopy layer were partially missing, horizontally-averaged statistics could still be obtained. In contrast to most formulations, the mean velocity profile within the canopy does not have an exponential shape, and the sectional-drag coefficient and mixing-length distributions cannot be considered constant. In light of this results and of recent developments in urban-canopy modelling, we propose a new formulation for the sectional-drag coefficient, which exploits the apparent self-similar behaviour of the axial-pressure difference across roughness elements.

4.1   Introduction and background

Urban areas affect the development of atmospheric boundary layers, typically leading to an increase of the streamwise momentum deficit and turbulence intensity in the near wall region. Their impact is generally quantified using a roughness function ΔU^+, which modifies the universal smooth-wall formulation for the mean velocity profile (Coles, 1956). Despite its nonlinear behaviour at low Reynolds number, in the fully-rough regime, the viscous contribution to surface drag becomes negligible (Flack and Schultz, 2010) and ΔU^+ reaches an asymptote that scales with the viscous-normalised roughness length y_0^+ (i.e. $\Delta U^+ \propto \ln y_0^+$). The latter can then be used as an equivalent, alternative measure of the roughness strength, in which case the vertical velocity distribution in the inertial sublayer (IS) reads

$$U^+ \equiv \frac{U}{U_\tau} = \frac{1}{\kappa} \log\left(\frac{y-d}{y_0}\right), \tag{4.1}$$

where U_τ is the skin-friction velocity, y is the wall-normal coordinate and $\kappa = 0.384$ is the von Kármán coefficient. The zero-plane displacement d is an intrinsic parameter to rough walls, causing a vertical shift of the inertial range of the boundary layer. It may arguably be interpreted as the height at which the mean-distributed surface drag appears to act (Jackson, 1981), yet, thus far, there is still a lack of authoritative data to support or disproof this hypothesis. Leonardi and Castro (2010), who investigated the flow over large cube roughness with varying density fractions, found that estimates of the zero-plane displacement given by the origin of the log-law and those determined as the centroid of the surface drag would not agree unless κ is specific to the surface morphology. Accordingly, their results suggest κ to fall with increasing roughness Reynolds number y_0^+. Other authors have questioned the universality of the von Kármán coefficient (see Frenzen and Vogel, 1995; Leonardi and Castro, 2010), but a definite conclusion seems elusive largely because of the limited range of Reynolds number at which experiments and simulations are carried out.

Of particular interest to boundary-layer meteorology is to characterise the flow above the canopy (described by equation 4.1) based on the surface morphology. Following the seminal work of Lettau (1969), various empirical relations have been derived from measurements and/or simulations over idealized urban environments to explain arbitrary canopy flows. Existing models have been comprehensively reviewed by Grimmond and Oke (1999) and Barlow and Coceal (2008), who have also advanced their own formulations. They broadly fall in two categories: *Morphometric models* that parameterise y_0 and d on the basis of density parameters and the characteristic height of the surface roughness H (Macdonald et al., 1998; Grimmond and Oke, 1999); and *quasi-empirical formulations* that attempt to model the canopy flow (Macdonald, 2000; Coceal and

Belcher, 2004; Yang et al., 2016). The second ordinarily treat urban agglomerates as a porous medium, analogously to vegetation canopies. As such, the governing equations are both time- and horizontally-averaged in space over a representative region of the surface roughness (i.e. a repeating unit for regularly distributed arrays), as outlined by Raupach and Shaw (1982). Canopy models are traditionally built upon a reduced axial momentum balance, specifically, (i) the contribution of the dispersive stress $\tilde{u}\tilde{v}$ within the canopy is considered to be negligible in comparison to the remaining terms; (ii) the (spatially-averaged) Reynolds shear stress $\overline{uv}$ is modelled by a *constant* mixing-length l_m relationship; and (iii) the canopy drag is expressed in terms of a sectional drag coefficient C_D, which is taken to be invariant with height. All listed assumptions considered, (i) to (iii), the vertical velocity distribution takes on an exponential behavior that is distinctive of canopy models. The formulation advanced by Yang et al. (2016) follows a different approach which is not strictly related to the differential form of the momentum equation, but it still preserves most qualities mentioned above.

In recent decades, there has been significant progress in modelling the mean canopy-flow characteristics, however, there is still some uncertainty regarding critical aspects. Castro (2017) rigorously demonstrated that $\tilde{u}\tilde{v}$ is far from negligible for all but very sparse arrays, and stresses that these should not be ignored when modelling urban flows with plan solidity $\lambda_P \geq 0.1$ (defined as the ratio between the plan area of the obstacles and the floor area of a repeating unit). Furthermore, the *constant* mixing-layer analogy which forms the basis of vegetation-canopy formulations appears to be inadequate to model urban-canopy turbulence, regardless of the packing density. Several studies (Reynolds and Castro, 2008; Barlow and Coceal, 2008; Castro, 2017) have shown that integral lengthscales are generally smaller at the canopy top than around the mid-canopy height. These are essentially modulated by the sharp shear-layer interface that is naturally diffused for vegetation canopies, causing the mixing-length to be uniform. It is also clear that the usual parameterisation of the canopy drag $D = \lambda_f C_D |U| U$ (with constant C_D) is inconsistent with the spatially-averaged velocity distribution, especially towards the bottom where it drops zero. Alternatively, Martilli and Santiago (2007) proposed a modified sectional-drag coefficient C_D^{mod} which depends instead on the turbulent and dispersive velocity scales. Santiago et al. (2008) showed that C_D^{mod} is predominantly uniform across the canopy height and does not grow exponentially towards the bottom. On the other hand, it requires full knowledge of the turbulent field in order to be determined, highlighting a serious limitation of experimental studies that have been so far unable to provide a complete and accurate description of the flow within the canopy.

Despite these general assumptions, there have been some attempts to improve the parameterisation of the mixing length in the near-wall region. For example, Coceal and Belcher (2004) used an harmonic mean to interpolate between the in-canopy scale $(h-d)$, controlled by the thickness of the shear layer, and that characteristic of the logarithmic

region (κy). Their closure model effectively yields non-exponential velocity profiles, but implies a uniform distribution of the mixing length for higher packing densities, which is inconsistent with Castro's (2017) observations. Macdonald (2000) and later Di Sabatino et al. (2008) have also advanced formulations to better capture the behaviour of the mean velocity profile over urban surfaces with height variability, defining a buffer region, corresponding to the roughness sublayer (RS), where the mixing-length is modelled via a weighted averaged. They argue that, since turbulent qualities of the RS generally dominate over those of the IS, the velocity profile is unlikely to exhibit a logarithmic behaviour down to the edge of the canopy. Measurements by Cheng and Castro (2002) have shown, nonetheless, that the IS may still persist in a spatial-average sense. In a different manner, the formulation of Yang et al. (2016) does not explicitly parameterise the mixing-length within the canopy. It uses instead a predefined shape function for the velocity profile (that could take any form), prescribed by a wake-sheltering model, to derive expressions for U_τ and y_0. This approach is particularly versatile, and it is sensitive to height variability, wind direction, shape and plan-arrangement of the roughness obstacles.

While non-exponential velocity profiles may be achieved with more sophisticated methodologies, it is not yet clear how to circumvent the assumption of a constant sectional-drag coefficient C_D, or how it could be extended to arrays of variable height. Incidentally, some formulations (Millward-Hopkins et al., 2011; Yang et al., 2016) rely on Jackson's definition of the displacement height to complete the turbulence closure problem, underlining the importance of this approximation. Modifications to the current definition of C_D (Martilli and Santiago, 2007) could potentially provide a better description of the pressure drag, however, they cannot be readily integrated in canopy models, suggesting that an entirely new approach must be considered. In this context, the present work seeks to provide a comprehensive analysis of the boundary-layer flow above and within urban-like roughness. Spatial averages of the flow field and the surface pressure distribution are examined to further elucidate the limiting assumptions of canopy models. We investigate the existence of an inertial sublayer immediately above the canopy layer, or lack thereof, and estimate the mean canopy-flow characteristics, including C_D and l_m. Finally, we present an alternative approach to the traditional canopy-model formulations, drawing attention to the self-similar behaviour of the axial pressure difference across individual roughness obstacles and its potential modelling aspects. We use in this analysis the experimental data set presented in §3, briefly described below.

4.2 Available experimental data

It is extremely difficult and time-consuming to obtain reliable velocity data in highly turbulent environments. Those from early field measurements are either poorly converged or insufficient to capture the spatial features of urban-canopy layers. There is also a limited number of laboratory studies which sought to characterise the flow within urban areas because of their intricate layout. Among them, an experiment conducted by Macdonald (2000) stands out: Using pulsed-wire anemometry (detailed in Handford and Bradshaw 1989), spatially-averaged velocity profiles were obtained by taking measurements at discrete locations, thought to be representative of the flow field. This approach is common practice in design of experiments, but its viability had not been addressed until Coceal et al. (2007) and Kono et al. (2010). By systematically varying the number and location of the probes over a repeating unit, they found that useful estimates of the flow statistics may indeed be achieved with a limited number of sampling points. In fact, the formulation derived by Macdonald (2000) upon this data set is arguably one of the most relevant. Later, Cheng and Castro (2002) reported near-wall measurements using laser-doppler anemometry, along with surface pressure information (using a pressure-tapped roughness element). Although measurements at the lower half of the canopy were affected by reflections off the sides of the cubes, velocity data points in the upper half could still be used to partially obtain an estimate of the sectional drag coefficient (see Coceal and Belcher, 2004; Castro, 2017). This is to date the only experimentally available measure of C_D. Reynolds and Castro (2008) performed planar particle image velocimetry (PIV) over large cube roughness, improving the spatial resolution of previously existing measurements. Their analysis primarily focused on the flow topology at the vertical centreplane of the obstacles and on the nature of turbulent structures populating the near-wall region. In addition to these, Claus et al. (2012b) present details of the surface pressure over an obstacle array at varying wind directions, having a significant impact on the total drag imposed by the surface. Cheng et al. (2007) carried out a similar experiment but varied in turn the packing density. Unfortunately, profiles of spatially-averaged mean velocity were not acquired, and therefore they were unable to draw a parallel between experiments and the corresponding numerical simulations (Leonardi and Castro, 2010; Claus et al., 2012a) in terms of sectional drag coefficient and mixing-length scale within the canopy.

The experimental data set presented in §3 is unique since it provides an integral description of the boundary-layer flow over large obstacle arrays (depicted in figure 4.1), including maps of velocity and static-pressure, and direct measurements of the wall shear stress. Data are available for a staggered cube array with plan solidity $\lambda_P = 0.25$ (C10U), and for an array of cuboids with the same plan arrangement but a variable height distribution (C10R). The mean roughness height $H = 10\,\mathrm{mm}$ and the standard
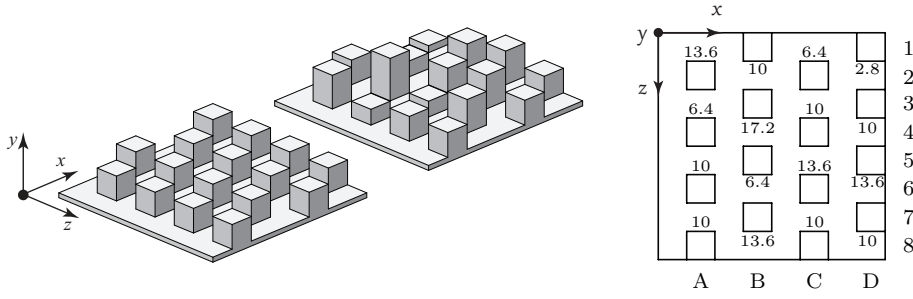
FIGURE 4.1: ILLUSTRATION OF THE ROUGH SURFACES. On the left, perspective view of a repeating unit of each surface roughness. On the right, the plan view of the staggered array including the heights of each individual element in mm for the case with a random height distribution. Elements are identified by means of an alphanumeric grid, displayed on the right and bottom sides. The XX axis indicates the principal flow direction.

deviation $\sigma_H = 0.3H$. $H/\delta \approx 0.1$ for both surfaces, where δ is the boundary-layer thickness. Snapshots of planar-PIV were acquired at different spanwise locations to obtain an accurate spatial representation of the flow field within the canopy. In contrast to previous studies (Cheng and Castro, 2002; Cheng et al., 2007; Claus et al., 2012b), in which surface pressure is measured by pressure-tapping opposite faces of individual roughness elements, the pressure fields were inferred from in-plane velocity data, thereby enjoying increased spatial resolution. As discussed in §3, this approach suffers from the missing (out-of-plane) components of velocity and acceleration in turbulent flows, but it produces nonetheless sensible estimates of surface pressure. Additionally, since static pressure is evaluated over the entire field-of-view (FOV), it may prove useful to further our understanding about the interplay between drag production and the canopy flow topology. Besides the current data set, we also consider results from direct numerical simulation (DNS) by Leonardi and Castro (2010), of a turbulent boundary layer over cube arrays with varying λ_P, and data from a large eddy simulation (LES) by Xie et al. (2008) over a geometrically similar array of cuboids as C10R. The relevant boundary-layer parameters are summarised in table 4.1.

4.3 The mean-flow features

In this section, we examine the basic properties of the boundary layer developing over each obstacle array. We assess the presence of outer-layer similarity and then consider the flow in terms of inner scaling, whereby dynamically relevant roughness length scales and the zero-plane displacement height are estimated. Spatially-averaged quantities over the canopy region and the mean pressure fields, at selected spanwise locations, are also presented here. These are compared against reported measurements and numerical solutions.

TABLE 4.1: Relevant parameters of the boundary-layer flow and corresponding uncertainty values. The friction velocity U_τ was directly measured using a floating element (FE) balance, described in §2. Estimates of d^p rely on Jackson's (1981) definition of displacement height. That of Leonardi and Castro (2010) accounts not only for surface pressure but also the frictional drag.

Data set	U_τ/U_0	H^+	Re_τ	y_0^+	y_0/H	d^p/H
C10U (current data)	$0.0651 \pm 1.7\%$	440	5,288	39.9	0.091	0.619
Leonardi and Castro (2010), $\lambda_P = 0.25$	0.110	90		6	0.067	0.617
C10R (current data)	$0.0689 \pm 1.6\%$	465	6,091	53.7	0.116	0.735
Xie et al. (2008)	0.0816	391		37.1	0.095	0.710

4.3.1 Outer-layer similarity

Canopy models rest on the principle of *outer-layer similarity* (Townsend, 1976), by which turbulent motions outside the RS become independent of viscosity and the surface conditions. Over rough walls, outer similarity emerges at sufficiently high Reynolds number, provided the roughness length scale is a small portion of the boundary-layer thickness δ (Perry and Abell, 1977). Only then may the velocity profile above the canopy be expressed by a standard log-wake function that scales appropriately. This hypothesis entails the existence of universal distributions for the viscous-scaled velocity defect data and the streamwise turbulence intensity, represented in figure 4.2. The spatially-averaged profiles over C10U and C10R show a remarkable collapse between each other for $(y - d)/\delta > 0.2$, evidencing the presence of outer-layer similarity in spite of the large relative height of the roughness obstacles ($\delta/H \approx 12$ in the worst case). Hot-wire data for a smooth-wall boundary layer at a lower $Re_\tau = \delta U_\tau/\nu$ are included for reference (chapter 2), and are in reasonalby good agreement with the current measurements. Note that accurately determining the velocity scaling U_τ (to within 2%) is paramount, for large uncertainties would undermine the reliability of this assessment.

It is well established that outer-layer similarity is closely related with the RS, but it is not yet clear what are the relevant length scales which determine its extent, and there is little information on how to quantify it. The usual approach consists in identifying the blending height above which the flow is horizontally homogeneous. Accordingly, Cheng and Castro (2002) found the depth of the RS to be approximately $1.85H$ (C10U) and $2.5H$ (C10R), after an initial development length when it becomes invariant from fetch and wind direction. In terms of boundary layer thickness, its effect propagates as far as 0.15δ (C10U) and 0.18δ (C10R), which is still below the typical limit of the inner region $y/\delta \approx 0.2$. A larger penetration would inevitably introduce inhomogeneities farther away from the wall, and potentially cause the breakdown of the inertial sublayer.
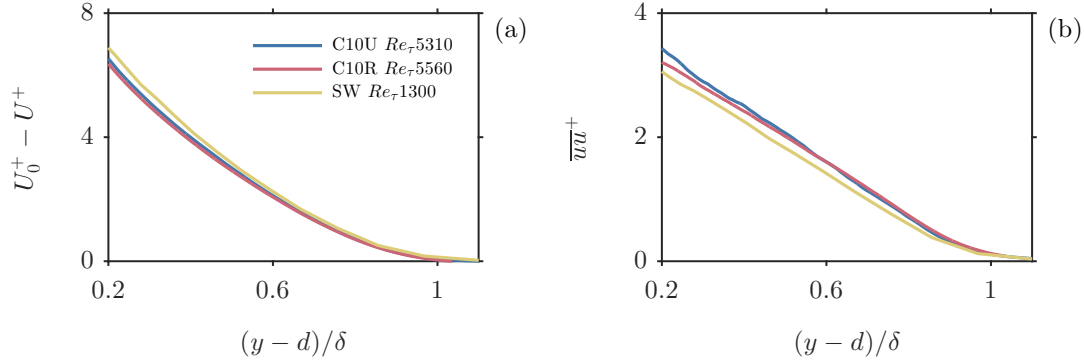
FIGURE 4.2: OUTER-LAYER SIMILARITY. **(a)** Viscous scaling of the spatially averaged velocity deficit over C10U and C10R. **(b)** The viscous-scaled streamwise turbulence intensity. Hot-wire data for a smooth-wall boundary layer at $Re_\tau = 1300$ were included to evaluate the existence of outer-layer similarly.

On this basis, the extent of the RS has been regarded as an indicator of outer similarity (Ligrani and Moffat, 1986). However, it has been shown that in rare, extreme cases where $\delta/H = 5$ (Amir and Castro, 2011) the outer region may still conform to the usual universal profile. Other studies in turn found roughness with much smaller heights that appeared to violate this hypothesis (Krogstad et al., 1992; Bhaganagar et al., 2004; Placidi and Ganapathisubramani, 2018), so it would be misleading to expect it to hold solely based on this criterion. Several authors have attempted to find alternative, 'meaningful' indicators that embody the roughness effect on the mean flow. They are typically based on a ratio between the characteristic turbulent length scale in the outer region and that of the surface roughness, such as δ/H, δ/H_S or δ/y_0 (Jiménez, 2004; Flack et al., 2005; Castro et al., 2013), where H_S is the sandgrain roughness of Nikuradse (1950). Some of these criteria reliably predict outer similarity for different surfaces, but consistently fail for large obstacle arrays. In this respect, Placidi and Ganapathisubramani (2018) recently argued that a suitable parameterisation must account, in addition to a relative measure of the roughness strength, for the nature of the canopy drag associated with the local surface topology. In which case it should consist of a combination of multiple parameters, rather than a single one. Their results suggest that, for large obstacle arrays, if the plan area of the sheltered region exceeds $\approx 20\%$ of the floor area of a repeating unit, then wall similarity is likely to hold provided that $\delta/H > 7$ and $\delta/H_S > 10$. This effect is quantified in Placidi and Ganapathisubramani (2018) by the sheltered solidity fraction $\lambda_S = (A_T - A_S)/A_T$, where A_T is the total plan area and A_S is the sheltered plan area. Particularly, $\lambda_S|_{C10U} = 0.5$ and $\lambda_S|_{C10R} = 0.62$ satisfy the condition $\lambda_S < 0.8$, and, since $\delta/H > 7$ and $\delta/H_S > 10$ are also verified (refer to table 4.2), both cases meet the requirements for wall similarity.
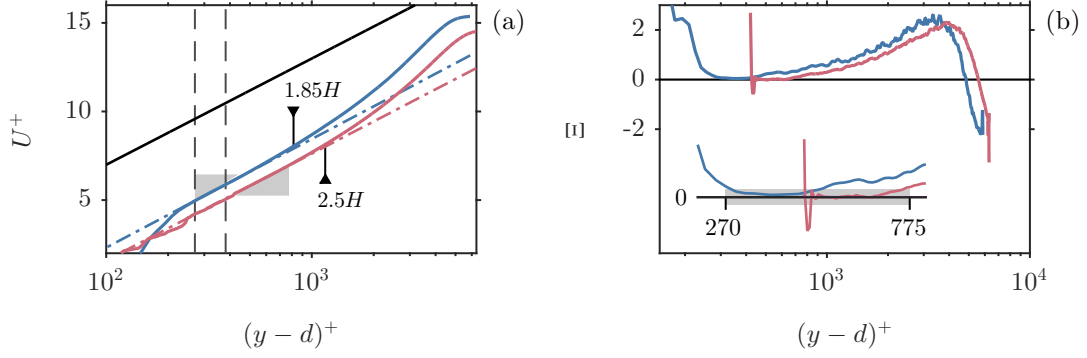
FIGURE 4.3: ESTIMATION OF THE SURFACE PARAMETERS. **(a)** Inner viscous scaling of the mean streamwise velocity profiles over C10U (blue) and C10R (red). Dotted-dashed lines are the linear-log fit through the inertial range with slope $\kappa = 0.384$ (highlighted gray), labels indicate the edge of the roughness sublayer (RS) and the solid-back line represents the log law for a smooth-wall boundary layer with negative zero intercept $A = -5$. **(b)** Indicator functions defined by equation 4.2. The inset shows a detail of the plateau corresponding to the log region where $\Xi = 0 \pm \epsilon_\Xi$, which for C10U ranges $270 - 440$ and for U10R $425 - 775$.

4.3.2 Boundary-layer parameters

Figure 4.3 shows the spatially-averaged, viscous-scaled velocity distribution alongside the indicator function

$$\Xi = \frac{\partial U^+}{\partial y^+}(y - d)^+ - \frac{1}{\kappa}, \tag{4.2}$$

obtained by taking the partial derivative of equation 4.1 with respect to y^+. Ξ is commonly used to identify the extent and slope of the log region over smooth walls (Österlund et al., 2000), but it may as well be an effective tool to estimate the height of the zero-plane displacement d, if U_τ and κ are known a priori. The displacement height is searched for such as to minimise the indicator function within the IS, which occurs where $\Xi = 0 \pm \epsilon_\Xi$. By letting $\epsilon_\Xi = 0.02/\kappa$ and $\kappa = 0.384$, the extent of the inertial range and the zero-plane displacement were determined for each surface (listed in table 4.2). The uncertainty in d was estimated by conducting a linear error propagation analysis on equation 4.2, yielding the expression

$$\epsilon_d^2 = \frac{1}{2\Delta_{xy}^2}\left[\left(\frac{\partial U}{\partial y}\right)^{-2}\frac{U_\tau}{\kappa}\right]^2\epsilon_U^2 + \left[\left(\frac{\partial U}{\partial y}\right)^{-1}U_\tau\right]^2\epsilon_\Xi^2 + \left[\left(\frac{\partial U}{\partial y}\right)^{-1}\frac{1}{\kappa}\right]^2\epsilon_{U_\tau}^2 + \Delta_{xy}^2. \tag{4.3}$$

Equation 4.3 factors the most important error contributions including uncertainties in the mean velocity data ϵ_U, the friction velocity ϵ_{U_τ}, the spatial resolution of the vector field Δ_{xy} and the arbitrary tolerance ϵ_Ξ. The wall-normal gradient of velocity was obtained via a second-order central difference scheme. An alternative, more conservative approach to this analysis is to consider ϵ_Ξ as a proxy for the uncertainty in the slope κ; then $\epsilon_\Xi = (1/\kappa^2)\epsilon_\kappa$. Assuming $\epsilon_\kappa = 5\%$, the uncertainties in the zero-plane displacement

TABLE 4.2: Boundary-layer flow parameters relevant to outer-layer similarity, and the zero-plane displacement estimated from pressure data (d^p/H) and indirectly from the mean velocity profile (d/H).

Case	δ/H	H_S/δ	λ_S	ΔU^+	d^p/H	d/H
C10U	12	7.3	0.50	13.6	0.619	0.65 ± 0.041
C10R	13	5.3	0.62	14.9	0.735	0.82 ± 0.033

become instead $0.056H$ (C10U) and $0.065H$ (C10R).

The IS appears to be immersed for the most part within the RS, supporting the hypothesis of Cheng and Castro (2002) that the spatially-averaged velocity profile may assume a logarithmic behaviour where turbulence is predominantly influenced by the surface geometry. We highlight that since they followed a less stringent definition to evaluate the bounds of the inertial range (based on the variation of the spatially-averaged shear stress), their values are somewhat larger than those reported here. Closer estimates would have been obtained by relaxing ϵ_Ξ. Contrary to the traditional, well-defined layer arrangement above the canopy, wherein the RS is followed by the IS which in turn precedes the outer region, the current analysis (based on the indicator function) suggests that the IS persists down to the canopy top. This is apparent in figure 4.3 for C10U and C10R, although the shear-layer interface is comparably diffused in the latter case. For this reason, below the height of the tallest element ($\approx 1.7H$) the velocity profile deviates from the classical formulation. Macdonald (2000), Di Sabatino et al. (2008) and Millward-Hopkins et al. (2012) among others, have all suggested different matching function to model the velocity profile below the IS, defining a reference height $\mathcal{O}(H)$ below which the logarithmic law does not apply. We believe these expressions are essential towards improving existing canopy models; however, a much narrower buffer region should be considered that is not associated with the depth of the RS but instead with the height variability of the surface roughness (e.g. $1 < y/H < 1 + \sigma_H$). We thus conclude that using a logarithmic profile to set the velocity-continuity condition at the edge of urban canopies, as in Macdonald (2000), Coceal and Belcher (2004), Millward-Hopkins et al. (2011) and Yang et al. (2016), is a sensible approximation, especially for uniform arrays.

Both velocity profiles have a linear-log region that is shifted downward by the roughness function ΔU^+, indicating an increased momentum deficit over these surfaces that is marginally larger for C10R. Given the existence of outer-layer similarity, the roughness function could be evaluated by assuming the functional form for the viscous-scaled velocity profile of Coles (1956) or by means of relationship 4.1 (which implies $\Delta U^+ \propto \ln y_0^+$), yielding similar results. In terms of sandgrain roughness H_S^+, both cases are well past the onset of the fully-rough regime at $H_S^+ \gtrsim 80$ (Flack et al., 2007), as expected from
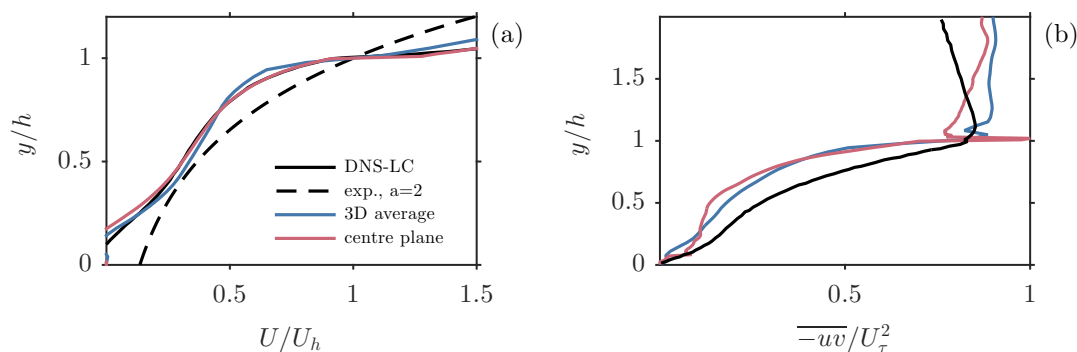
FIGURE 4.4: CANOPY-FLOW STATISTICS. **(a)** Axial mean velocity profile normalised by $U_h = U(y/h = 1)$ and **(b)** the viscous-scaled Reynolds shear stress. Estimates were obtained by taking the streamwise average of the flow field at the centre plane of the cuboids (red) or by spatially averaging over the total volume (blue). These are compared against DNS data from computations by Leonardi and Castro (2010) (black) and an exponential function with $a = 2$ (black dash-line).

the measurements of skin-friction coefficient in figure 2.10.

4.3.3 Within the canopy

In contrast to the outer region, where the mean velocity field is horizontally homogeneous, the flow within the canopy is dictated by the relative distribution of the roughness obstacles. Given its three-dimensional nature, planar-PIV measurements were taken at different spanwise locations, and flow statistics in the region with no optical access (behind out-of-plane obstacles) were linearly interpolated along the streamwise direction for C10U. A similar treatment could not be carried out for C10R owing to a substantial lack of data. All field variables within the canopy were extrinsically averaged over the total volume, as outlined in Böhm et al. (2013).

Mean flow and turbulence statistics

The spatially-averaged, mean velocity profile normalised by U_H and the Reynolds shear stress within the canopy layer are represented in figure 4.4. Streamwise averages along the vertical centreplane of the cubes and DNS data from computations by Leonardi and Castro (2010) are included for comparison. Note that in-plane and volume-averaged distributions closely agree with each other. Given plan arrangement of staggered arrays, any streamwise wall-normal plane extends across the three different flow regimes, which pertain to the constricted region, front-recirculation region and building wake region (as defined in Coceal et al., 2007). So provided the entire FOV is captured, streamwise averages alone should be representative of spatially-averaged statistics. There is also some degree of spanwise averaging of the flow across the laser sheet that could explain,
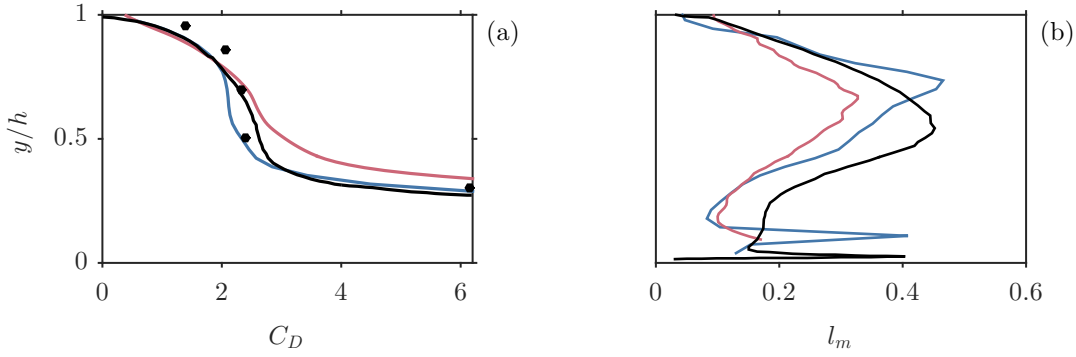
FIGURE 4.5: MEAN CANOPY-FLOW CHARACTERISTICS. **(a)** Sectional drag coefficient within the canopy of C10U, defined by equation 4.4. The canopy drag force was estimated from pressure data and normalised by the spatially-averaged velocity field. Values inferred from velocity data and surface pressure from Cheng and Castro (2002) are included for reference. **(b)** Canopy mixing-length scale, given as the ratio $(\sqrt{-\overline{uv}})/(\partial U/\partial y)$. Legend as for figure 4.4.

albeit not entirely, the general agreement.

The current velocity measurements collapse with DNS data below the roughness height, revealing a strong shear layer around the canopy top where the vertical velocity gradient is most intense. Incidentally, the velocity scaling U_H is inferred at this location, so its uncertainty is intrinsically high whether field or point measurements techniques are considered — the error associated is a function of $(\partial U/\partial y)^2 \epsilon_{\Delta_{xy}}^2$. In agreement with observations by Coceal and Belcher (2004) and Castro (2017), the velocity profile within the canopy does not seem to follow an exponential growth. This appears to be the case for any kind of urban-like roughness, even those with a variable height distribution that are characterised by much lower velocity gradients. The Reynolds shear stress exhibits a peak around the canopy height and then quickly drops to zero approaching the bottom. The present experiment was conducted at a higher roughness Reynolds number y_0^+ than numerical simulations by Leonardi and Castro (2010), consequently, the shear-layer interface is marginally stronger in the former case, yielding a lower shear-stress level below. Similarly, y_0^+ may change by varying the roughness density parameters. Kono et al. (2010) and Castro (2017) have shown that the shear layer weakens with a reduction of λ_P while the Reynolds shear stress within the canopy becomes increasingly significant.

Canopy-flow characteristics

In a manner parallel to figure 4.4, where first and second order statistics are shown, figure 4.5 presents the variation of the sectional drag coefficient C_D and the mixing

length l_m within the canopy. Here, C_D is defined as

$$C_D(y) = \frac{2D(y)}{\rho|U(y)|U(y)}, \tag{4.4}$$

where $D(y) = \lambda_P \Delta p(y)$ is the canopy drag force per unit volume of air and Δp is the sectional-drag profile (discussed in detail in the following section). l_m is given by

$$l_m = \frac{\sqrt{-\overline{uv}}}{\partial U/\partial y}. \tag{4.5}$$

As expected, in-plane and volume-averaged quantities still show similar trends, but to a lesser extent. There is a fairly good agreement between estimates of C_D. Specifically, the present measurements and DNS data from Leonardi and Castro (2010) collapse in the upper half of the canopy for $y/h > 0.7$. The values inferred from velocity data and surface pressure by Cheng and Castro (2002) are relatively higher. Yet they still capture the general behaviour of the sectional drag coefficient, contrary to suggestions that the lowest data point could be an outlier (Coceal and Belcher, 2004), in which case it would appear to plateau. Constant C_D is a crucial assumption of urban-canopy models, despite the fact that, by definition, it is likely to grow exponentially approaching the wall (refer to equation 4.4). The viability of this approximation has been rigorously examined by Castro (2017) for a range of packing densities and different plan arrangements (staggered and aligned). He stresses that unless $\lambda_P \leqslant 0.15$, assuming uniform distributions of C_D across the canopy is a clear oversimplification. Such is also the case of the mixing-length scale, which grows larger toward the mid-canopy height. Similarly to $-\overline{uv}$, l_m is a function of the roughness Reynolds number y_0^+ and is therefore expected to diverge from the DNS solution. The peak appears to shift upwards with increasing y_0^+ due to the sharper decay of the Reynolds shear stress away from the canopy top, as shown in figure 4.4b.

4.4   Sectional-drag profile

Following the analysis of the pressure fields presented in §3.3, and addressing the need to improve existing canopy-modelling assumptions, we examine whether the sectional-drag profile Δp can be described by a functional relationship, governed by a combination of scaling laws.

The flow field characteristics and surface pressure distribution around wall-mounted obstacles, either isolated or immersed within urban canopies, are related, in one way or another, with the mean velocity shear at the obstacle height $\tau_h = \partial U/\partial y|_h$. This is substantiated by numerous studies on boundary-layer flows over (isolated) wall-mounted cubes (Castro and Robins, 1977; Fackrell, 1984; Hearst et al., 2016), two-dimensional

ribs (Castro and Fackrell, 1978), and urban-like roughness (Yang et al., 2016). The former typically normalise shear by the time scale of the flow at the obstacle height, which results in $\hat{\tau}_h = (h/U_h)(\partial U/\partial y)|_h$. This quantity has been shown to be a relevant parameter affecting the wake characteristics of an obstacle, and could potentially be used as a scaling factor for the canopy drag distribution. However, its definition is not compatible with the large majority of canopy models which assume a velocity profile that is continuous but non-differentiable at the shear-layer interface. It additionally does not embody the effect of the Reynolds number by which the spatially-averaged mixing length and Reynolds shear stress within the canopy can be considerably modified, as illustrated in figures 4.4b and 4.5b — both DNS and experimental data share a similar mean velocity distribution U/U_h, so $\hat{\tau}_h$ should be approximately the same.

In a different context, Yang et al. (2016) parameterise the wake geometry of individual roughness elements based on the ratio of the horizontal convective velocity scale (U_h) to the turbulent transport velocity scale in the vertical direction (U_τ). They argue that the wake expansion rate behind solid objects, whose aspect ratio is on the order $\mathcal{O}(1)$ or lower, is primarily driven by $U_h^+ = U_h/U_\tau$, since the contribution to entrainment by the lateral shear layers is relatively small. Specifically, for a given obstacle array, the sheltered volume fraction within the canopy is proportional to U_h^+ and, consequently, so is the spatially-averaged vertical velocity gradient. We may then interpret this quantity as a measure of the strength of the shear layer that is not explicitly dependent on τ_h. This is valid provided the plan solidity λ_P remains constant (i.e. varying the Reynolds number alone), or otherwise it must also be taken into account. For example, surfaces with different plan density may have similar U_h^+, but the sparser would naturally have a less prominent shear layer over a repeating unit. In view of these arguments, the non-dimensional shear expressed by $G(\lambda_P, U_h^+)$ is investigated here as an appropriate, useful scaling parameter for the sectional-drag profile of urban canopies, which contains information about the local Reynolds number and the mean velocity shear at the height of the obstacles.

4.4.1   Self-similar behaviour

Figures 4.6 and 4.7 show the axial-pressure difference across isolated or partially isolated obstacles within a series of staggered-cube arrays with varying plan solidity as well as C10R. As opposed to §3.3, Δp is normalised here by $\rho U_\tau^2/\lambda_P$, such that when the viscous contribution to surface drag is negligible the vertically-integrated value is unity. The sectional-drag is predominantly influenced by the pressure distribution over the windward face of the cuboids. High pressure regions typically develop around the top edge, where the velocity is higher, giving rise to a local maxima $(\hat{p}_u, \hat{y}_u)$ which falls in the range $0.8-0.9h$ (refer to figure 4.7). Towards the bottom, the sectional drag becomes less significant, reaching a local minima $(\hat{p}_l, \hat{y}_l)$ before recovering nearer to the wall. Despite
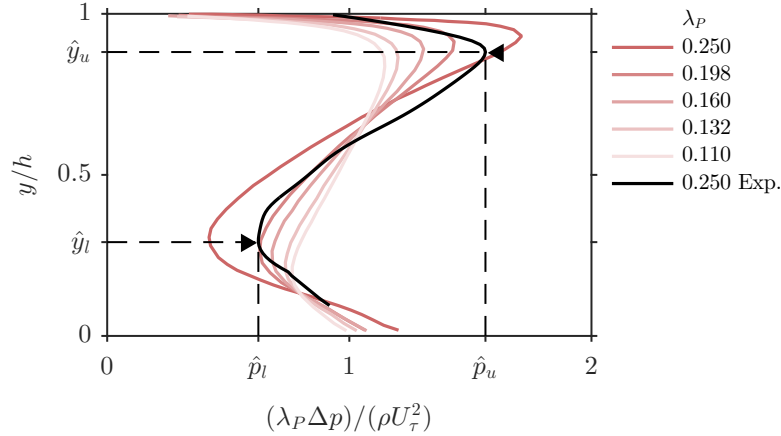
FIGURE 4.6: NORMALISED DRAG PROFILES OF STAGGERED-CUBE ARRAYS. DNS data, from computations by Leonardi and Castro (2010), for cube arrays with varying plan solidity λ_P are indicated by the coloured lines. Δp is normalised by the total contribution to surface drag (viscous and pressure-based) of a single roughness element $\rho U_\tau^2/\lambda_P$. The sectional drag from pressure reconstruction (black-solid line) was normalised using U_τ obtained with the floating element balance. Arrows pinpoint the local extrema $(\hat{p}_u, \hat{y}_u)$ and $(\hat{p}_l, \hat{y}_l)$.

the large discrepancy between the profiles, the current data appears to suggest that a suitable functional expression could be parameterised by the local extrema $(\hat{p}_u, \hat{y}_u)$ and $(\hat{p}_l, \hat{y}_l)$, which effectively capture the general behaviour of Δp. We therefore attempted to find correlations for the location and intensity of these peaks based on the scaling arguments mentioned above.

The results shown in figure 4.8 reveal a positive, linear relationship between the viscous-scaled sectional drag and $\lambda_P U_h^+$, interpreted as a measure of the significance of the shear layer. The slope of the linear regression of $\hat{p}_u$ is larger than that of $(\hat{p}_u - \hat{p}_l)$, suggesting that for a given fetch δ/h and fixed Re_τ, increasing U_h (e.g. by increasing the local roughness height) mostly comes with an increase of $\hat{p}_u$. This implies that, for obstacle arrays with a variable height distribution, the surface pressure should become increasingly homogeneous approaching the wall, provided there are no wake-sheltering effects to account for. Additionally, the regression line of the peak-to-peak amplitude shown in figure 4.8b exhibits a zero intercept, which indicates that if the shear layer becomes less prominent, the sectional drag profile gradually becomes more uniform across the canopy height. This might be the case, for example, of deep boundary layers at low Re_τ, or if a roughness element lies within a sheltered region.

Correlations between the height of the local extrema and the significance of the shear layer are visibly weaker in comparison. As shown in figure 4.8c, there is no obvious relationship that fits the data. While staggered-cube arrays show a steep positive trend, the local maxima for isolated obstacles within C10R only marginally shifts upwards with $\lambda_P U_h^+$. This suggests that other factors besides the strength of the shear layer may also
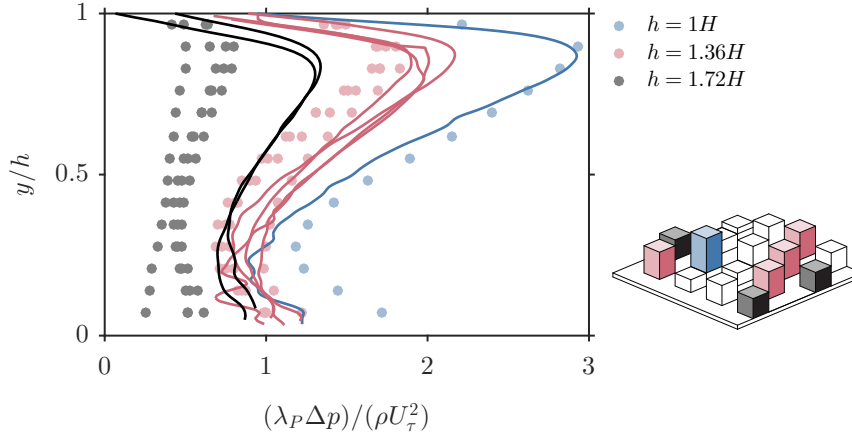
FIGURE 4.7: NORMALISED DRAG PROFILES OF ISOLATED CUBOIDS IN C10R. LES data from Xie et al. (2008) (circles) and the present experimental measurements (solid lines) are coloured according to the height of the cuboids, as illustrated at the bottom-right corner. Δp is normalised by the average surface drag (viscous and pressure-based) produced by the roughness elements $\rho U_\tau^2 / \lambda_P$.

be important, although we cannot readily identify them. Note that $\hat{y}_u$ is expected to plateau near the edge of the obstacle since the pressure field above the canopy takes on the value of the freestream static pressure (i.e. $\Delta p = 0$ at $y/h = 1$). This boundary condition sets the upper limit for $\hat{y}_u$, which is always less than 1. Given the small dispersion of the data around the mean, we assume for modelling purposes $\hat{y}_u = 0.85$, with an uncertainty associated of about $0.05h$.

Finally, the position of the local minima $\hat{y}_l$ appears to be driven by size of the frontal recirculating region which develops upstream of the roughness obstacles, and imposes a low pressure value on the windward face. This is apparent in figure 4.8d if the staggered-cube arrays and C10R are examined individually. Data shows that the local minima shifts upwards with increasing solidity fraction due to the sheltering effect; on the contrary, it drops when, for the same plan arrangement, the relative obstacle height with respect to the vortex diameter becomes larger. Thus it seems that $\lambda_P U_h^+$ does not have a significant impact, other than the role it plays in modifying the flow topology within the canopy. Other parameters which affect the wake sheltering, such as the aspect ratio of the obstacles, their relative height and location are important.

4.4.2   Modelling aspects

The potential for a functional relationship is well supported by the current analysis, except for the lack of a meaningful framework to predict the height of the local minima. In this respect, a wake sheltering model such as those proposed by Millward-Hopkins et al. (2011) and Yang et al. (2016), could prove useful to factor in the influence of the surface geometry. Consider the sketch in figure 4.9, illustrating the sheltering effect within an
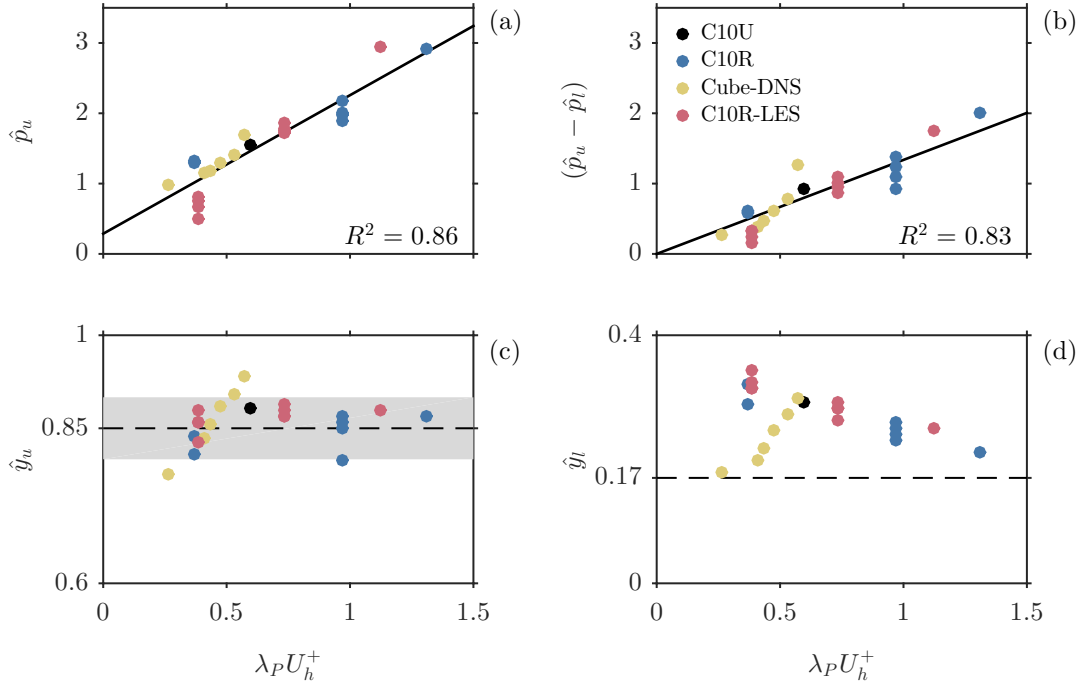
FIGURE 4.8: EMPIRICAL CORRELATIONS FOR THE SECTIONAL-DRAG PARAMETERS. As detailed in figure 4.6, **(a)** is the intensity of the local maxima $\hat{p}_u$, **(b)** is the peak-to-peak amplitude $(\hat{p}_u - \hat{p}_l)$, **(c)** is the position of the local maxima and **(d)** the position of the local minima normalised by the local roughness height h, upon $\lambda_P U_h^+$, interpreted here as a measure of the significance of the shear layer. The linear regressions are given by the black-solid lines, and the corresponding R^2 values are indicated at the bottom-right corner.

arbitrary urban canopy (the wind direction is from left to right). This simplified model consists of a sheltered region that is characterised by having low momentum, and an unsheltered region where the flow is defined by the horizontal convective velocity scale U_h. Three flow regimes can be identified: unsheltered or isolated, which pertains to the tallest obstacles; fully sheltered; and partially sheltered. The degree of wake sheltering is quantified by the length scale h_s (equivalent sheltered-layer height for arbitrary arrays), found in the range $0 < h_s/h \leqslant 1$ (from unsheltered to fully sheltered). Yang et al. (2016) parameterised the wake geometry as a function of the width w and height h of the roughness elements, as well as the wake expansion rate $\tan(\theta)$ defined in figure 4.9. As previously explained, the latter is assumed to be driven by the ratio U_τ/U_h, specifically, $\tan(\theta) = C_\theta(U_\tau/U_h)$, where C_θ is a coefficient of order unity that may depend on the roughness geometry. The reattachment point is then given by $L_s = h/\tan(\theta)$ (i.e. the stronger the shear layer, the larger the wake). Finally, h_s is determined by considering the streamwise spacing between obstacles and their relative height distribution.

   The sheltered-layer height h_s effectively captures the impact of surface geometry on the canopy-flow topology, and could potentially be used to estimate the location of the
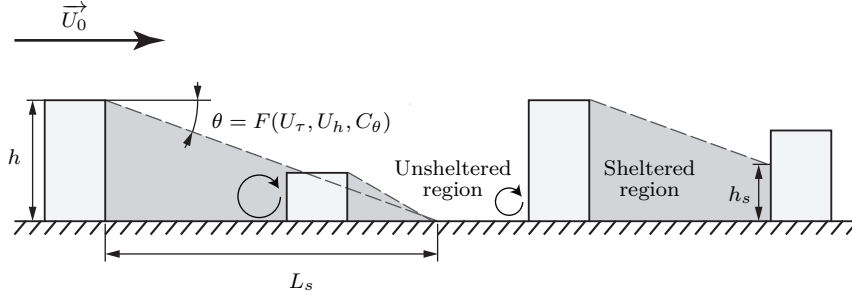
FIGURE 4.9: SKETCH OF THE VOLUME SHELTERING EFFECT. Yang et al. (2016) suggested a simplified model consisting of a sheltered region where the velocity is low and an unsheltered region with characteristic velocity U_h. Three possible flow regimes are contemplated here: isolated (tallest obstacles), fully sheltered and partially sheltered. Length scale h_s quantifies the degree of sheltering and is a function of the streamwise spacing between the roughness elements and $L_s = h/\tan(\theta)$.

local minima $\hat{y}_l$, in which case we may write $\Delta p^+ = F(\lambda U_\tau^+, h_s)$ as a shape function for the axial pressure difference across individual roughness elements. We propose here a piecewise third-order polynomial function (i.e. cubic spline) with zero derivatives at the local extrema for F, shown graphically in figure 4.10. The ith piece of the 1-dimensional spline through points $[0, \hat{y}_l, \hat{y}_u, 1]$ is represented by

$$\hat{p}_i = \lambda \Delta p_i^+ = a_i + b_i \hat{y} + c_i \hat{y}^2 + d_i \hat{y}^3,$$

with

$$\frac{d\hat{p}}{d\hat{y}}(\hat{y}_u) = \frac{d\hat{p}}{d\hat{y}}(\hat{y}_l) = 0.$$

(4.6)

$\hat{p}_u$, $\hat{p}_l$ are given by the empirical correlations defined in figure 4.8, while y_l would be governed by h_s from the wake sheltering model. The boundary condition at the wall $\hat{p}_i(0) = \hat{p}_l + C_w(h/H)(\hat{p}_u - \hat{p}_l)$. This linear model is a function of the relative height distribution h/H, ensuring that $\hat{p}_i(0)$ is always greater than $\hat{p}_l$. The coefficient $C_w = 1/4$ was adjusted to yield the best fit of the shape function to the sectional-drag profile of the roughness element 8-B ($1H$). The estimates depicted in figure 4.10 were obtained by taking into account the spatially-averaged velocity distribution over C10R and the value of friction velocity from FE data. Using the correlations derived above, these quantities allow to determine the local extrema for each roughness element, except for $\hat{y}_l$ that we set to $0.25H$ for the sake of simplicity (based on figure 4.7) — if $\hat{y}_u < \hat{y}_l$, then $\hat{y}_l = \hat{y}_u$ and $\lambda \Delta p_l^+ = \lambda \Delta p_u^+$. Otherwise, $\hat{y}_l$ would have been estimated from a wake-sheltering model.

The functional relationship outlined above convincingly reproduces the profiles of sectional drag across the entire canopy height. However, there is a weak quantitative agreement with results from pressure reconstruction which arises from the spread of the data around the regression lines in figure 4.8. We emphasise that by fixing $\hat{y}_l$, the
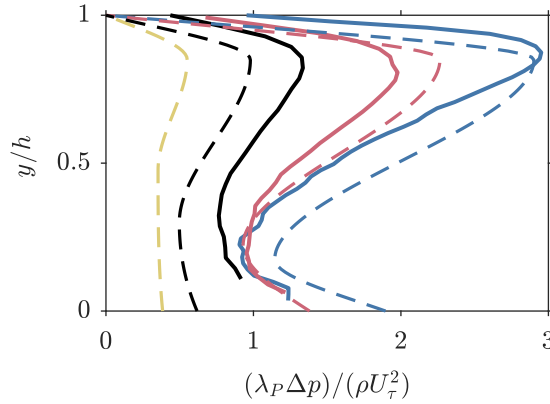
FIGURE 4.10: ESTIMATED DRAG PROFILES OF SELECTED OBSTACLES IN C10R. Dark-coloured lines are cubic splines in three pieces with zero-derivatives at the local extrema (equation 4.6), specified via empirical correlations depicted in figure 4.8. $\hat{y}_l$ was set to $0.25H$ based on the profiles given in figure 4.7. Dashed-lines are the corresponding profiles obtained from pressure data.

pressure difference across sheltered or partially sheltered obstacles cannot be adequately reconstructed. Nevertheless, the zero-plane displacement $d/H = 0.75$ could still be estimated based on the contribution of the largest (unsheltered) roughness elements, which amount to nearly 90% of the total pressure drag. This value is only marginally higher than that obtained directly from pressure data, as detailed in §4.3.3, and lower values would have been expected had the shortest obstacles been accounted for. Besides U_h^+, if the friction velocity U_τ is additionally specified, the distribution of surface drag can also be determined. Figure 4.11 shows that the current estimate may differ greatly from the values presented in figure 3.10a, but the distribution is still consistent. Except for obstacle 1-B, which lies in the same streamwise alignment as the shortest one, the relative error is on average 20%.

4.5 Further discussion and conclusion

Numerous urban-canopy models, with variable degree of complexity, have been proposed to characterise the mean boundary-layer flow based on the surface geometry. Formulations typically introduce assumptions about the turbulent structure that were in part derived from vegetation canopy models. Specifically, the horizontally-averaged axial mean velocity profile is taken to be exponential within the canopy — as a result of a constant sectional-drag coefficient C_D and mixing length l_m distributions — and transforms to the usual logarithmic behaviour immediately above. They further imply outer-layer similarity and a few assume that the origin of the log-law and height of the momentum sink (Jackson's, 1981 hypothesis) are different but equivalent definitions of the zero-plane displacement d. Castro (2017) recently examined the validity of these
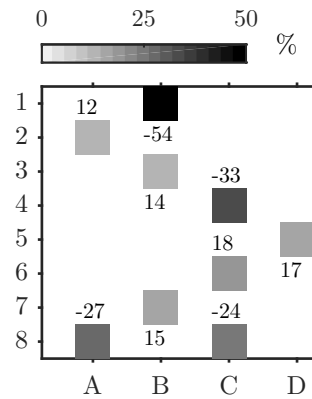
FIGURE 4.11: ESTIMATED DISTRIBUTION OF PRESSURE DRAG OVER A REPEATING UNIT OF C10R. Similarly to figure 3.10a, each individual obstacle is color-coded according to the percent error between the value inferred from the pressure fields and that estimated following the formulation outlined in this section.

assumptions and showed that, in most cases, they are rather limiting; however, it is unclear whether relaxing them would improve predictions sufficiently to justify the added complexity. In this perspective, we conducted a detailed analysis of the flow field above and within the canopy of C10U and C10R.

Scaled profiles of the horizontally-averaged axial velocity and turbulent intensity revealed the existence of outer-layer similarity for $y/H > 0.2$, despite the large relative roughness height. The extent of the inertial range and height of the zero-plane displacement were estimated in terms of inner viscous scaling by means of the indicator function Ξ, with constant $\kappa = 0.384$. The first was found to be fully immersed within the roughness sublayer and to persist down to the edge of the canopy for both surfaces. This is essentially in agreement with results of Cheng and Castro (2002), yet they used a less stringent criterion to identify the logarithmic region that appeared to extend well beyond the edge of the roughness-affected layer. Overall, estimates of the displacement height given by the origin of the log-law compare well with those determined as the centroid of the surface drag. Both methods predict an increase due to height variability and the discrepancy between them is at worse 8.5%. The agreement is noticeably better for the uniform cube array (C10U), which could suggest that either these are not equivalent approaches or κ is not universal but depends instead on the nature of the surface roughness. This possibility has also been discussed by Frenzen and Vogel (1995) and Leonardi and Castro (2010), amongst others, but it still remains an open question as the difference between the estimates is on the order of the uncertainty associated with these methods. Regarding the mean canopy-flow characteristics, the velocity profile did not exhibit an exponential behaviour and both the sectional-drag coefficient and the mixing length were found to vary significantly across the canopy layer of C10U.

Although equivalent measurements had previously been reported by Macdonald (2000) and Cheng and Castro (2002), these were either vertically unresolved or incomplete in the lower half of the canopy, so the velocity profile would appear to follow an exponential curve. Similarly, Castro (2017) argued that exponential velocity profiles may arise if a sufficiently coarse grid is used in numerical simulations, and convincingly showed, using an extensive body of quality data sets, that only for very sparse arrays with $\lambda_P \leq 0.15$ could C_D and l_m be reasonably approximated by uniform distributions.

In a bid to improve urban-canopy models, an alternative approach to the usual formulation of the sectional-drag coefficient was introduced. We found that the normalised axial-pressure difference across individual roughness obstacles exhibits a self-similar behaviour, which can be described by a functional expression parameterised by the local extrema $(\hat{p}_l, \hat{y}_l)$ and $(\hat{p}_u, \hat{y}_u)$. Based on scaling arguments, we established correlations for the location and intensity of these peaks. The non-dimensional shear factor (at the obstacle height) $\lambda_P U_h^+$ was shown to be a relevant parameter that linearly scales the intensity of the local extrema $\hat{p}_l$ and $\hat{p}_u$. In a different manner, the height of the local maxima $\hat{y}_u$ appeared to vary only marginally with $\lambda_P U_h^+$, and each data set revealed a distinct trend, indicating that other factors might also play a role. The results further suggested that the size of the recirculating region on the windward face of the cuboids is the driving parameter for the height of the local minima $\hat{y}_l$. It is thus highly dependent on the surface geometry, including the shape of the obstacles, the plan arrangement and the relative height distribution. We argued that $\hat{y}_l$ is associated with mutual sheltering effects and, therefore, may possibly be parameterised by a geometric wake-sheltering model, such as that of Yang et al. (2016). Using a three-piece cubic spline and assuming a fixed $\hat{y}_l$ (given the lack of a predictive tool), the normalised sectional-drag profile of individual roughness obstacles and surface drag distribution over C10R could be reproduced, and showed a good qualitative agreement with pressure data.

Despite its potential modelling aspects, this empirical formulation does not stand on its own. It is unable to provide an estimate of U_τ, and d can only be determined if the viscous-scaled velocity profile is specified well into the canopy (at least down to the edge of the shortest obstacles). Rather, we believe it could prove more useful if implemented in the framework of existing canopy models, since it overcomes the usual requirement for a (constant) sectional-drag coefficient that has been shown to be inconsistent with the spatially-averaged velocity profile.

Chapter 5

Scale interactions in velocity and pressure over a staggered cube array

An integral description of the boundary-layer flow developing over a large-cube array is obtained using velocity data from planar PIV to reconstruct the underlying pressure field via 2D-TH, introduced in chapter 3. We follow a POD-based scale decomposition of the streamwise velocity component to characterise the turbulent structure of the flow and inter-scale dynamics within the roughness affected layer, yielding comparable results to previous studies. Coupled-statistics of the forces acting on a target roughness element provide insight into the relevant mechanisms responsible for surface drag. This is complemented by conditional analysis and extended POD of the pressure field based on velocity modes to further our understanding of the velocity-pressure interrelations. It is found that coherent motions, at different scales, leave an imprint on the pressure field. Specifically, positive and negative pressure fluctuations are associated with flow regions experiencing a local deceleration and acceleration, respectively. We identified the larger turbulent features to contribute the most to the pressure variance, however, their direct contribution to surface drag appears to be mitigated by the relative size of the roughness obstacles that are considerably smaller. We conjecture that the pressure wave induced by the passage of alternating high and low-momentum regions evenly affects the flow field over a wide region, coupling the forces on the windward and leeward sides of the cube which, in turn, partially cancel each other out. This suggests that uncorrelated intermediate and small-scale pressure fluctuations are more important to the drag force variance. Nevertheless, as evidenced in this work, large-scale structures are still significant for the role they play in modulating the small-scale pressure events in the near wall region.

5.1 Introduction and background

The importance of accurate predictive models for wall-bounded turbulence cannot be overstated, as it governs a variety of flow processes (e.g. mixing, heat and mass transfer) and is key to the aerodynamic and hydrodynamic performance of most engineering systems (Marusic et al., 2010). In order to understand the behaviour of these seemingly chaotic flows, researchers have traditionally focused on the smooth-wall boundary layer problem, particularly on the inter-scale dynamics that occur very close to the surface.

Large coherent structures, populating the logarithmic region, are known to impose a footprint onto the near-wall turbulence (Townsend, 1976; Metzger and Klewicki, 2001; Abe et al., 2004; Hoyas and Jiménez, 2006), and to modulate the amplitude and frequency of small-scale motions (Hutchins and Marusic, 2007; Mathis et al., 2009; Ganapathisubramani et al., 2012; Baars et al., 2016b). They also have direct implications on the local fluctuations of wall shear stress. Hutchins et al. (2011) showed, by conditional averaging the flow field with data from surface probes, that a negative skin-friction event is more likely to occur in the presence of a low-speed large-scale motion (LSM), which is usually accompanied by an attenuation of the small-scale energy near the wall and amplification in the outer region (the behaviour is reversed for large-scale positive fluctuations). Of particular interest to wall turbulence is the frictional Reynolds number $Re_\tau = \delta U_\tau / \nu$, which may be regarded as a ratio of the outer (δ) and inner length scales (ν/U_τ). Here, δ is the boundary-layer thickness, U_τ is the friction velocity, and ν is the fluid kinematic viscosity. The interaction between the large and small scales becomes increasingly prominent with Re_τ, as the spectral separation between them increases and the large-scale outer-layer events become more energetic (De Graaff and Eaton, 2000; Metzger and Klewicki, 2001). This leads not only to an increase of the near-wall turbulence intensity via superposition of energy by the LSMs, but also to an increase of the amplitude modulation (Mathis et al., 2009). In view of this coupling mechanism, Marusic et al. (2010) and Mathis et al. (2011a) proposed a model for predicting flows in the near-wall region based on the large-scale signal in the logarithmic layer, proving to be a valuable tool to overcome the lack of spatial resolution of experimental measurements at high Reynolds number. It additionally offers the opportunity for turbulence control strategies, towards drag reduction or to improve mixing and heat transfer, by simply targeting the large-scale structures (Hutchins et al., 2011; Abbassi et al., 2017). In a different manner, it could also be explored to characterise the flow topology solely based on surface information (Discetti et al., 2019).

Much less has been done to understand the interrelation between turbulence and the flow processes over very-rough walls like urban canopies, where the roughness height h is $\mathcal{O}(0.1\delta)$. Within the roughness-affected layer, Castro et al. (2006) revealed a two-scale behaviour featuring a dominant scale that is on the order of the canopy height,

and an intermediate scale that is characteristic of the shear-layers shed from the leading edge of the cubes. While this is detrimental to the near-wall turbulence production and amplitude modulation, as it implies a reduced spectral separation between the largest and the near-wall scales (Basley et al., 2018), both experimental and numerical studies have found qualitative similarities with smooth-wall boundary-layer flows in terms of shape and scaling of the turbulent features (Grass et al., 1991; Djenidi et al., 1999; Coceal et al., 2007; Lee et al., 2011; Mejia-Alvarez et al., 2014), as well as in terms of inter-scale dynamics (Perret and Rivet, 2013; Anderson, 2016; Basley et al., 2018). In fact, there is convincing evidence to support the classical notion that the surface roughness merely acts to modify the boundary conditions, but not the nature of the turbulent flow (Takimoto et al., 2013; Basley et al., 2019; Perret et al., 2019). Roughness elements typically lead to a reduction of the streamwise coherence of the LSMs and to an increase in the spanwise direction throughout the entire boundary layer, while the viscous-normalised spacing between them appears to remain unchanged (see e.g., Leonardi et al., 2004; Coceal et al., 2007; Lee et al., 2011, 2012). These modifications presumably arise from intense outward injections of low-momentum fluid from the canopy which disrupt the development of larger-scale structures. As for the amplitude modulation (AM), Perret and Rivet (2013) and Blackman and Perret (2016) explored the apparent relationship between two-point third order statistics and the amplitude mechanism found by Mathis et al. (2011b), to reveal the existence of a top-down, non-linear scale interaction similar to smooth-wall boundary layers. Nadeem et al. (2015), Anderson (2016) and Basley et al. (2018) followed instead a decoupling procedure put forward by Mathis et al. (2009), based on the Hilbert transform. The first compared the flow over rod-roughened walls with varying streamwise spacing, and noticed some degree of dependence of the AM on the surface topology, which appears to be associated with modifications of the LSMs by the shedding of intermediate scales. Anderson (2016) has shown, nonetheless, that even for very-rough surfaces ($\delta/h = 4$), AM may still be present with the same intensity as in high-Reynolds number smooth-wall boundary layers.

Although much of the data reported on the effects of roughness on wall-bounded turbulence reveal recurring features and 'universal' scale interactions that appear to exist regardless of the surface conditions, the mechanisms responsible for drag generation are fundamentally different and still remain to be investigated. The present study focuses on characterising the surface drag over a staggered-cube array, and establishing its interrelations with the turbulent structure of the overlying flow. We further examine the measurements of particle image velocimetry (PIV) of the boundary-layer which developed over C10U, at $Re_\tau = 5288$ and $\delta/h = 12$, introduced in chapters 3 and 4 (additional flow parameters are listed in table 4.1). Profiles of the viscous-scaled velocity deficit and streamwise turbulence intensity revealed the existence of outer-layer similarity for $(y-d)/\delta > 0.2$, and the logarithmic region was found to be completely immersed

within the roughness sublayer, extending down to the edge of the canopy. This implies that LSMs are particularly exposed to intense injections of intermediate scales by the roughness elements, which could alter or prevent altogether AM at this Reynolds number. We therefore start by identifying the large coherent structures that populate the near-canopy region using proper orthogonal decomposition (POD), as proposed by Perret and Savory (2013), and check for AM of the small scales by exploiting its relationship with the scale-decomposed velocity skewness (Mathis et al., 2011b). Perret and Rivet (2013) have also followed this approach, circumventing the requirement for time-resolved velocity measurements and the choice of a cutoff frequency to decompose the flow field into coherent motions and stochastic fluctuations, which is especially challenging given the short spectral separation between scales. Contrary to smooth-wall boundary layers, where surface drag is of a continuous nature, over rough walls it is mostly pressure-based and is essentially locked onto the largest roughness obstacles. Having a uniform height distribution, the force acting on any given element within C10U is representative of the local wall shear stress, so it may be used to assess the potential links with the LSMs. In the absence of instrumentation to directly measure the axial load (e.g. by pressure tapping a roughness obstacle or using sensor elements), estimates are obtained from instantaneous maps of the pressure field presented in chapter 3.

5.2   The large and small scales

In this section, we decompose the velocity field into large and small scales using POD. We characterise the large-scale features above the canopy and examine the interaction between scales, in particular, the modulation mechanism reported in literature, which might also play a role on the fluctuations of surface drag.

5.2.1   Proper-orthogonal decomposition

POD was introduced by Lumley (1967) as an unbiased technique for studying coherent structures in turbulent flows. It consists in identifying a set of orthonormal functions which best correlate, in a statistical sense, with a set of observations that could either be an experimental measurement or a numerical solution of a scalar or vector field (e.g. pressure, velocity), taken at a given time. The reader is referred to Berkooz et al. (1993) for a more rigorous explanation. Given the discrete nature of the current dataset, and following the bi-orthogonal approach outlined by Aubry et al. (1991), each PIV-snapshot of the fluctuating streamwise velocity field $u'(\mathbf{x}, t)$, containing n_p point measurements, is reshaped into a row vector $a^{(j)} \in \mathbb{R}^{1 \times n_p}$. Here, $\mathbf{x}$ and t are the space and time coordinates, respectively. The data set is then organised in a rectangular matrix $A \in \mathbb{R}^{n_t \times n_p}$, where n_t is the total number of realisations. Since $n_t \ll n_p$, we consider the *snapshot* formulation of the discrete Fredholm equation (Sirovich, 1987),
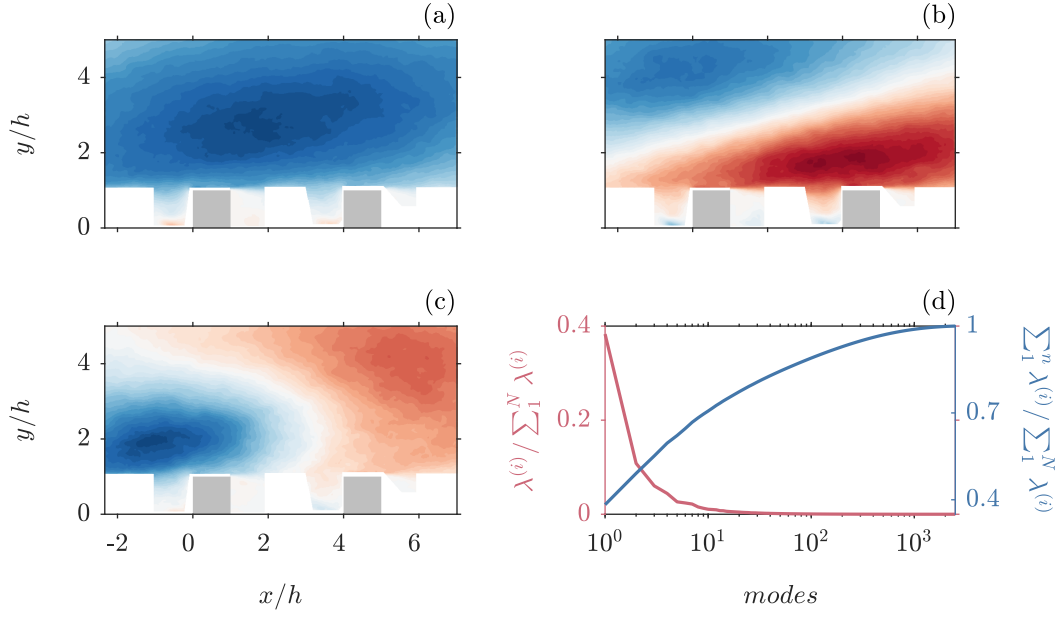
FIGURE 5.1: POD OF THE FLOW FIELD. First three spatial POD modes, ϕ_A^1 **(a)**, ϕ_A^2 **(b)** and ϕ_A^3 **(c)**. Red and blue-shaded regions correspond to positive and negative streamwise velocity fluctuations, respectively. **(d)** The cumulative energy contribution of the flow field modes (on the right-vertical axis).

which is equivalent to the eigenvalue problem of the two-point, temporal correlation matrix of A, written as

$$AA^T \Psi_A = \Psi_A \Lambda \tag{5.1}$$

with $\Lambda = diag(\lambda^{(1)}, ..., \lambda^{(r)}) \in \mathbb{R}^{r \times r}$ containing the set of eigenvalues of AA^T, and $\Psi_A = [\psi_A^{(1)}, ..., \psi_A^{(r)}] \in \mathbb{R}^{n_t \times r}$ the set of eigenvectors. The columns of Ψ_A are otherwise known as temporal modes, and form the orthonormal basis for the columns of A. The spatial modes $\Phi_A = [\phi_A^{(1)}, ..., \phi_A^{(r)}] \in \mathbb{R}^{n_p \times r}$ are then expressed as the projection of the snapshots ensemble onto the temporal modes,

$$\Sigma_A \Phi_A^T = \Psi_A^T A, \tag{5.2}$$

where $\Sigma_A = diag(\sigma_A^{(1)}, ..., \sigma_A^r) \in \mathbb{R}^{r \times r}$ is a diagonal matrix containing the norm of each contribution and is equal to the square root of the eigenvalues Λ.

5.2.2 Large-scale coherent structures

Figure 5.1d shows the energy convergence of the POD modes within the roughness sublayer. Remarkably, the first mode alone contains nearly 40% of the streamwise turbulent kinetic energy, far more than any other, and the contribution of the first ten modes (out of 2500) exceeds 70%. The first mode shape depicted in figure 5.1a reveals a streamwise-elongated, forward-leaning feature spanning across the whole domain $\mathcal{O}(\delta)$,
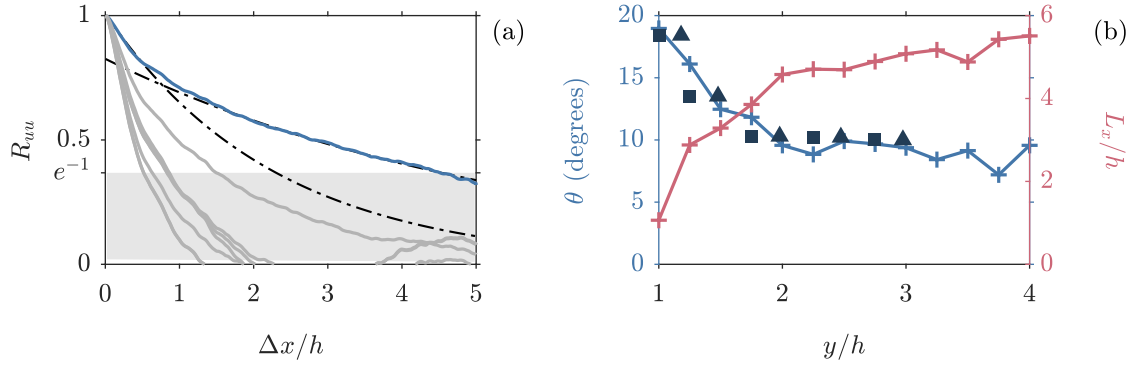
FIGURE 5.2: MORPHOMETRICS OF THE COHERENT STRUCTURES. **(a)** Two-point stream-wise velocity correlation R_{uu} for a fixed reference height $y/h = 2$ within the roughness sublayer (solid-blue line). The black dash-dotted lines are exponential curves of the form $ke^{-\Delta x/L_x}$ with $L_x/h = 2.3$ for $\Delta x/h < 1$ and $L_x/h = 5.6$ for $\Delta x/h > 1$. Solid-gray lines are correlations obtained for the same reference location by gradually removing the most energetic POD modes from the reconstruction of the velocity fields. **(b)** The angle of inclination θ of the structures (on the left-vertical axis) and the integral-length scale L_x (on the right-vertical axis) against the wall-normal location of the reference probe. Measurements of θ from Castro et al. (2006) (squares) and Reynolds and Castro (2008) (triangles) were included for reference.

which is presumably associated with high and low-momentum LSMs. This was suggested by Perret and Rivet (2013) who found that only mode one leaves a strong imprint in the time-delayed correlation function of the temporal coefficients $\Psi\Sigma$. Assuming a convection velocity, they estimated the average size of these coherent structures (those associated with $\phi^{(1)}$) to be approximately 1.2δ or $24h$. They additionally found the first POD mode to contribute the most to the shear stress in the outer region, whereas near the canopy top the second supersedes.

Contrary to Perret and Rivet (2013), the current data set is statistically uncorrelated, so it does not contain useful time information. The integral-length scale L_x is therefore estimated by fitting an exponential decaying function of the form $ke^{-\Delta x/L_x}$ to the spatial velocity correlation (e.g. Reynolds and Castro, 2008), defined by

$$R_{uu}(\mathbf{x}) = \frac{\langle u(\mathbf{x},t)u(\mathbf{x}+\Delta\mathbf{x},t)\rangle}{\sigma_u(\mathbf{x})\sigma_u(\mathbf{x}+\Delta\mathbf{x})},   \tag{5.3}$$

where $\langle\cdot\rangle$ is the ensemble average operator, $\Delta\mathbf{x}$ is the separation between 'probes' and $\sigma_u(\mathbf{x})$ is the standard deviation of the velocity field. The streamwise distribution of R_{uu} at a fixed reference height $y/h = 2$ is given in figure 5.2a, evidencing the two-scale behaviour reported by Castro et al. (2006). The correlation function can be fitted by two exponentials with decay constants differing by a factor of two — $L_x/h = 2.3$ for $\Delta x/h < 1$ and $L_x/h = 5.6$ for larger horizontal probe separations. At greater heights, however, the effect of the shear layers on the turbulence dynamics fades away and the flow exhibits instead one dominant scale. The correlation function is then adequately fit

by a single exponential (not shown here). Additional curves were obtained for the same location by gradually removing the most energetic POD modes from the reconstruction of the velocity fields. The results emphasise the link between the first mode and the large-scale events, as L_x (given by the larger dominant scale) drops from about $5.6h$ to less than $2h$ if only heigher-order modes are retained, which correspond to events of smaller wavelength.

The size L_x and typical inclination angle of the structures θ are plotted against the vertical coordinate in figure 5.2b, with θ expressed as the inclination of the contour level $R_{uu} = e^{-1}$. The integral-length scale increases monotonically from $1.1h$ at the canopy top to $5.5h$ at $y/h = 4$. This agrees well with results from Castro et al. (2006), Coceal et al. (2007) and Reynolds and Castro (2008) under similar flow conditions, in the sense that, immediately above the canopy, scales are expected to be on the order of the cube height, but are instead associated with the depth of the boundary layer away from the wall. Specifically, $L_x/\delta = 0.40 - 0.45$ in the outer region ($y/h > 2.5$), which closely matches the values reported by Ganapathisubramani et al. (2005) for the smooth wall case (0.42 at $y/\delta = 0.5$), and Reynolds and Castro (2008) (0.44). The angle of inclination sharply decreases from $19°$ at $y/h = 1$ to $10°$ at $y/h = 2$, thereafter decreasing marginally to approximately $8°$. This behaviour is opposite to the smooth-wall counterpart, where the LSMs are inclined at a shallow angle near the wall and lift away with increasing height (e.g., Marusic, 2001; Ganapathisubramani et al., 2005). Krogstad and Antonia (1994) had previously reported this behavioural change, owing to the large wall-normal velocity fluctuations over the surface. A more elaborate explanation was proposed by Coceal et al. (2007), in terms of the basic structural elements of the hairpin-packet model of Adrian et al. (2000), of which they found evidence on instantaneous snapshots of the filtered data and by conditionally-averaging the flow field. They suggest that the larger distance between hairpin vortices and their symmetric part causes the self-induction by the legs of the vortex (upwards) to become stronger relative to the mean shear effect (that contributes to align and stretch vorticity in the streamwise direction). The decreasing trend in θ is thus associated with a more rapid decrease of the self-induction as compared to the decrease of the mean shear.

5.2.3 Scale interactions

To quantify the degree of AM, we consider the expansion of the streamwise velocity skewness $S_u = \langle u'^3 \rangle / (\langle u'^2 \rangle^{3/2})$ using a scale decomposed signal $u' = u'_L + u'_S$, where $u'_L = \psi_A^{(1)} \sigma_A^{(1)} \phi_A^{(1)}$ and $u'_S = u' - u'_L$ are the large and the small-scale fluctuations, respectively. The third-order moment of the streamwise velocity then reads

$$\langle u'^3 \rangle = \langle u'^3_L \rangle + \langle u'^2_L u'_S \rangle + \langle u'^2_S u'_L \rangle + \langle u'^3_S \rangle. \tag{5.4}$$

There is substantial evidence that the scale-decomposed skewness factor is closely related with AM effects (Sreenivasan et al., 1999; Schlatter and Örlü, 2010; Mathis et al., 2011b). Notably, Mathis et al. (2011b) showed that the cross term $\langle u_S'^2 u_L' \rangle$ can be used as an alternative diagnostic tool to a more complex procedure, based on the correlation between the filtered envelope of the small-scale fluctuations and the large-scale signal (Mathis et al., 2011a). This approach has been shown to produce sensible results (e.g. Perret and Savory (2013); Perret and Rivet (2013); Blackman and Perret (2016)), in spite of its intrinsic limitations (Mathis et al., 2011b), and is particularly advantageous when time-resolved velocity measurements are unavailable.

The wall-normal evolution of the terms on the right-hand-side of equation 5.4 are shown in figure 5.3a; profiles were streamwise averaged over a repeating unit, at the centreplane of the cubes. Apart from $\langle u_L'^3 \rangle$ that is nominally zero throughout the inner region of the boundary layer, all remaining terms have a non-negligible contribution. The small-scale term $\langle u_S'^3 \rangle$ accounts for the majority of the skewness factor below the edge of the canopy, since the shear-layer interface provides a high-degree of sheltering of the flow within from that above (refer to figure 5.1a). It then decreases with height in the roughness sublayer, becoming negative at around the mid-point of the logarithmic region. The cross term $\langle u_S'^2 u_L' \rangle$ is most significant above the canopy, within the roughness-affected layer, indicating the existence of a non-linear interaction mechanism that could be AM of the small-scales under the influence of large structures. In an similar manner, the fact that $\langle u_L'^2 u_S' \rangle$ is non-negligible could suggest an equivalent feedback mechanism through which the large scales are modified (Perret and Rivet, 2013). Blackman and Perret (2016) have shown, however, that this is likely an artifact of the POD scale decomposition, which is energy driven as opposed to time or spectral-based filters. Consequently, lower-order modes, typically associated with large-scale structures, may encompass part of the small-scale energy as well.

To further elucidate the scale characteristics of the POD modes, the cross term $\langle u_S'^2 u_L' \rangle$ of the scale-decomposed skewness factor at $y/h = 1.5$, which is presumably related to AM, is plotted in figure 5.3b against the number of POD modes retained in the reconstruction of the large-scale velocity component u_L'. These data confirm the results of Perret and Rivet (2013), showing a sharp decay as u_L' gradually combines higher-order modes. It thus seems that a POD-based scale decomposition is a sensible approach for the current dataset, though care should be exercised since it does not provide a decomposition purely based on physics.

5.3 Surface drag characteristics

The force experienced by a target roughness element located at $x/h = 0$ is used here as a proxy for the local wall shear stress. Instantaneous maps of the pressure field, obtained
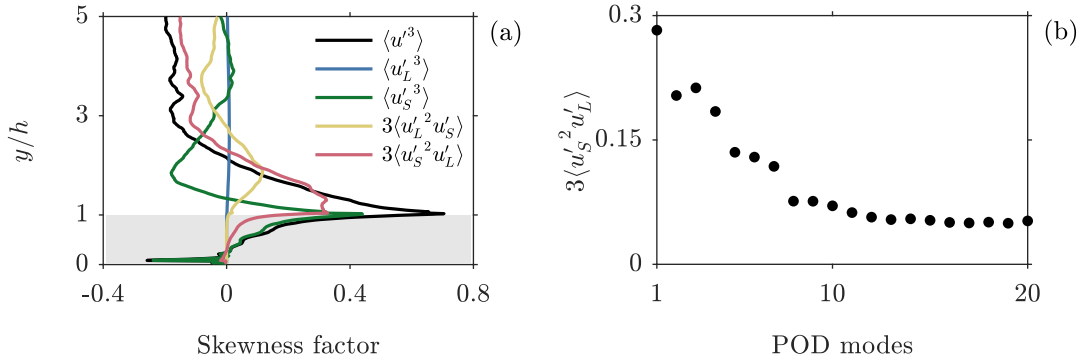
FIGURE 5.3: SCALE INTERACTIONS. **(a)** Terms of the scale-decomposed streamwise skewness factor S_u (equation 5.4). **(b)** Cross term $\langle u_S'^2 u_L' \rangle$ at $y/h = 1.5$ as a function of the number of POD modes retained in the reconstruction of the velocity field.

via 2D-TH in chapter 3, were used to estimate the axial load $F = F_w - F_l$, where the subscript identifies the windward (F_w) and leeward (F_l) sides of the cube. The height of the centre of pressure y_{cp} could also be determined, whose mean value corresponds to the zero-plane displacement d^p. Note that the uncertainty associated with y_{cp} is inversely proportional to F (refer to equation 3.10), causing estimates of y_{cp} to exceed h in a few instances that were not included in the following analysis. Force statistics and conditional averages of the flow field are presented in this section to provide some insight into the canopy-drag behaviour and the relevant flow phenomena.

5.3.1 Force statistics

The joint-probability density function (JPDF) of the fluctuating force and height of the centre of pressure, normalised by the corresponding standard deviations σ_F and $\sigma_{y_{cp}}$, is shown in figure 5.4a, alongside each individual probability density function (PDF). Interestingly, the force exhibits a Gaussian distribution, with frequent negative-drag or thrust-producing events that amount to nearly 13%. This value is greater than 0.1% reported for smooth walls (Alfredsson et al., 1988; Örlü and Schlatter, 2011), and stems from the different nature of the canopy drag that is predominantly pressure based. Although negative drag events would be expected, they have mostly been observed on rough particle-bed studies (e.g. Cameron et al., 2019) wherein the force is traditionally measured via direct methods. It is also evident that roughness obstacles experience extreme excursions of the force, over three times the standard deviation, which is about 98% of the mean value, against 20% over smooth walls (Alfredsson et al., 1988). The height of the centre of pressure shows a skewed distribution towards the edge of the cube with standard deviation $\sigma_{y_{cp}}/h = 0.14$. The force tends to act for the most part below the zero-plane displacement height (55%), albeit occasionally on the lower half of the cube for thrust-producing events. Positive deviations of y_{cp} exhibit a broader distribu-
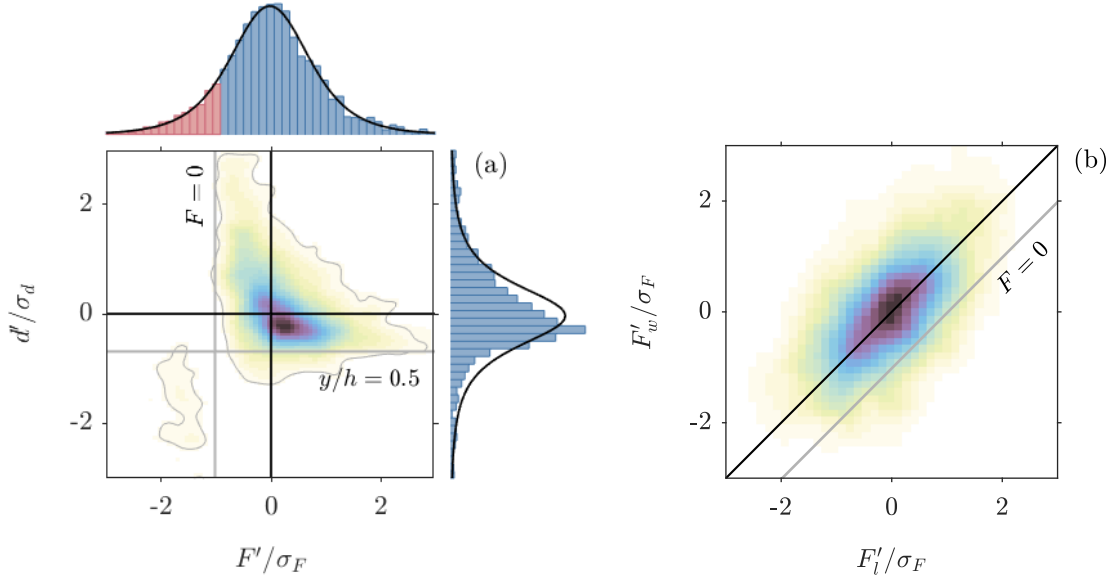
FIGURE 5.4: DRAG FORCE STATISTICS. **(a)** 2D JPDF of the fluctuating force F' and the height of the centre of pressure y'_{cp}, normalised by the standard deviations σ_F and $\sigma_{y_{cp}}$, respectively. The solid-gray lines indicate the cube half height (horizontal) and the zero crossing of the force (vertical). PDF of F' (on top) and y'_{cp} (on the right) overlaid with the corresponding Gaussian distributions (solid-black lines). **(b)** 2D JPDF of the fluctuating force on the windward F'_w and leeward F'_l sides of the cube. Along the solid-black line, the total force remains unchanged and equal to the mean value. Thrust-producing events lie below the solid-gray line.

tion, in some cases approaching the top of the cube, but are generally associated with the least intense force fluctuations. This could possibly be explained by the passage of small-scale turbulent pressure fluctuations associated with the shear layer, which leave an imprint on the upper half of the cube. Large-scale events, in contrast, are more likely to affect uniformly the pressure field within the canopy layer, causing the centre of pressure to lie at approximately half height. The JPDF of the force on the windward and leeward sides of the target roughness obstacle is given in figure 5.4b, normalised by the standard deviation of the total force σ_F. These quantities reveal a strong positive correlation $R_{F_w F_l} = 0.59$, and similar amplitudes, suggesting the existence of an underlying, advecting pressure wave that evenly affects the flow field over a wide region. The most extreme excursions of the force on either side of the cube partially or entirely cancel each other out, so the less intense, anti-signed events corresponding to the second and fourth quadrants of the plane (F'_w, F'_l) are the most important to surface drag.

5.3.2   Conditional averages

In view of these results, we examine the conditional averages of the fluctuating velocity field $\mathbf{u}'(\mathbf{x})$ based on the loading combination upstream and downstream of the target
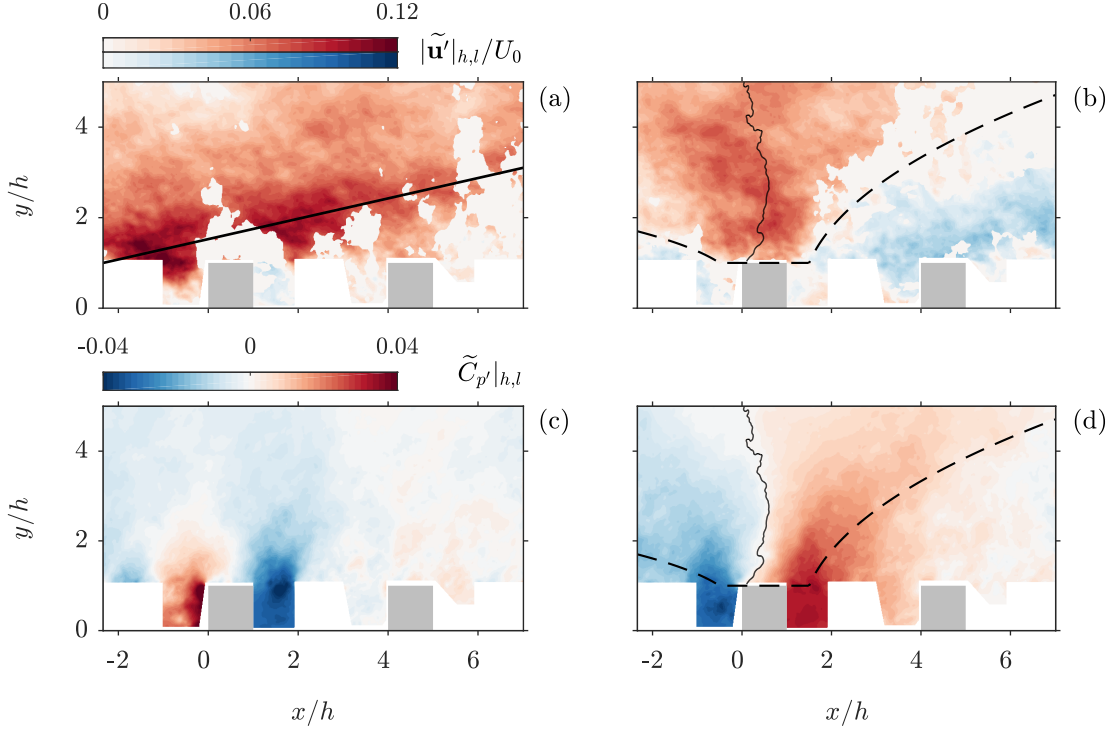
FIGURE 5.5: CONDITIONAL STRUCTURE OF THE BOUNDARY LAYER ON HIGH AND LOW DRAG EVENTS. Maps of the fluctuating velocity magnitude $|\mathbf{u}'|$ **(a)-(b)** and pressure coefficient $\widetilde{C_{p'}}$ **(c)-(d)**, conditionally averaged on a high (h) and low (l) drag events of the obstacle located at $x/h = 0$. Different color maps of velocity are for sweeps (shades of red) and ejections (shades of blue). The solid-black line in (a) represents the average inclination angle of the structure at 13°. In (b) and (d) the dashed-black lines indicate the shear-layer interface between the sweeping motion ($Q4$ events) and ejections ($Q1$ events), and the solid-black line the local minima of the magnitude of the conditioned pressure fluctuations.

element located at $x/h = 0$, defined as

$$\widetilde{\mathbf{u}'}\,|_h\,(\mathbf{x}) = \langle \mathbf{u}' \mid F_w'/\sigma_F > 0.5 \cap F_l'/\sigma_F < 0.5 \rangle$$

and

$$\widetilde{\mathbf{u}'}\,|_l\,(\mathbf{x}) = \langle \mathbf{u}' \mid F_w'/\sigma_F < 0.5 \cap F_l'/\sigma_F > 0.5 \rangle,$$

(5.5)

as well as of the pressure coefficient $\widetilde{C_{p'}}(\mathbf{x})$. The magnitude of the conditional-averaged velocity fluctuations is shown in figures 5.5a-b for positive and negative excursions of the force, respectively. Shades of blue indicate low-velocity outward motions, ejections or $Q2$ events, and shades of red indicate high-velocity inward motions, sweeps or $Q4$ events, that contribute the most to the wall-normal exchange of momentum between the canopy and the flow aloft. At the bottom, figures 5.5c-d are the corresponding conditional averages of the pressure coefficient.

For positive-drag fluctuations, a high-momentum LSM is clearly visible, similar in

shape to the fist POD mode. It lies at an average inclination angle of approximately 13°, in agreement with values estimated from two-point spatial correlations (refer to figure 5.2b). The large pressure difference appears to arise mostly from the sweeping motion impinging on the surface roughness, as the fluid is pushed against the windward side of the cube, creating a highly turbulent region just below the canopy top. It is then deflected upwards and over, giving rise to a $Q1$ event ($u' > 0$, $v' > 0$) immediately above, which in turn contributes to reduce the static pressure in the wake. A careful examination of figures 5.5b-d reveals that the mechanism responsible for negative-drag fluctuations is markedly different. High and low-pressure regions are noticeably broader, and appear to be associated with the large-scale outward and inward interactions. More precisely, the conditional flow structure is characterised by a large shear layer that extends across the entire field-of-view, indicated by the dashed-black line. Downstream of the roughness obstacle this interface is positive inclined and there is a local increase of the static pressure, as the flow is squeezed between the sweep and ejection regions. Within the canopy, the upward flow expands and the turbulent shear layer occupies a wider region, shedding small-scale structures into the roughness sublayer and thereby losing significance. Concurrently, the interface is negative inclined upstream of the cube for $x/h < 0$, and pressure is instead locally reduced. The relative inclination angle is important as it determines the nature of the interaction, which is one of pure shear and relatively less energetic. Although we conditionally averaged the flow field based on the force signal to identify relevant flow phenomena, similar patterns have been observed for different rough-wall boundary layers using distinct approaches, substantiating the present analysis. For example, Zhu et al. (2007) found that during sweeps the turbulent kinetic energy (TKE), Reynolds stresses and production/dissipation rates, have clear narrow peaks just below canopy height. Presumably, this scenario would be equivalent to that conditioned to a positive force fluctuation. During ejections, on the other hand, these variables exhibit a broad maxima above the canopy, contributing to reduce the energy content within. This would then explain the lower pressure value on the windward face of the cube for a condition of low drag. There is also a significant resemblance between the conditional flow structure in figure 5.5b and a bursting event that is a prime contributor to turbulence production (e.g. Runstadler et al., 1963; Kline et al., 1967). Several definitions have been proposed, most of which were comprehensively reviewed by Robinson (1991), but the phenomenon is typically characterised by violent outward eruptions of near-wall fluid and features a shear-layer interface that develops in-between an upstream, high-speed sweep and a downstream, low-speed ejection. Thomas and Bull (1983) studied the interrelation between wall-pressure fluctuations and the burst-sweep cycle in the buffer region of a smooth-wall boundary layer. They showed that an increase in pressure is generally associated with the passage of inclined shear layers that occur on the upstream side of the bursting process, and that it may traverse

most of the boundary layer thickness. This effect is visible too in figure 5.5d.

Of particular interest is the minima of the magnitude of the conditional-averaged pressure fluctuations, represented by the solid-black line on figures 5.5b-d. On closer inspection, it becomes evident that it lies in a sweeping region where the velocity fluctuations are most intense. This implies that, upstream of the contour line, where pressure is low, the flow is predominantly accelerated ($\partial \mathbf{u}'/\partial \mathbf{x} > 0$), whereas in the region downstream, an increase in pressure is accompanied by a local deceleration ($\partial \mathbf{u}'/\partial \mathbf{x} < 0$). A similar analysis was carried out by Hutchins et al. (2011) for a smooth-wall boundary layer. Tracing the separation between increased and reduced small-scale activity, they found that the small-scale energy attenuation or amplification is generally aligned with LSMs exhibiting local positive or negative accelerations, respectively.

5.4 Velocity-pressure interrelations

The influence of the LSMs populating the roughness sublayer is widespread. In addition to leaving a footprint onto the near-wall turbulence, via superposition of energy and amplitude modulation of the small-scale dynamics, the conditional analysis shows evidence that pressure may be equally affected. It is then reasonable to assume they have direct implications on the surface drag characteristics of rough-wall boundary layers, as they do for the smooth wall counterpart. Following the scale-decomposition of the streamwise velocity field presented in §5.2, we examine here this potential link, as well as the role of AM on drag production.

5.4.1 Pressure signature of the large scales

The linear relationship between the pressure field p and the large-scale, streamwise velocity fluctuations $u'_L = \psi^{(1)} \sigma^{(1)} \phi^{(1)}$ is expressed by the correlation function

$$R_{pu_L}(\mathbf{x}) = \langle u'_L(\mathbf{x}, t) \, p'(\mathbf{x}, t) \rangle / (\sigma_{u_L}(\mathbf{x}) \, \sigma_p(\mathbf{x})), \tag{5.6}$$

where σ_{u_L} and σ_p are the corresponding standard deviations. It is represented in figure 5.6, overlaid with an arbitrary contour line and the locus of the first POD mode shape (given in figure 5.1a) to illustrate the phase relationship between a large scale event and pressure. The correlation function is fairly uniform along the vertical direction, but monotonically increases with downstream distance, suggesting that high-momentum regions typically experience an adverse-pressure gradient ($\partial p/\partial x > 0$), while low momentum regions are instead subject to favourable-pressure gradients ($\partial p/\partial x < 0$). The correlation value is predominantly negative in the upstream region, becoming positive farther downstream. Incidentally, the zero-crossing is aligned with the locus of the coherent motion, where the local extrema of the velocity fluctuations lie (i.e. minima or
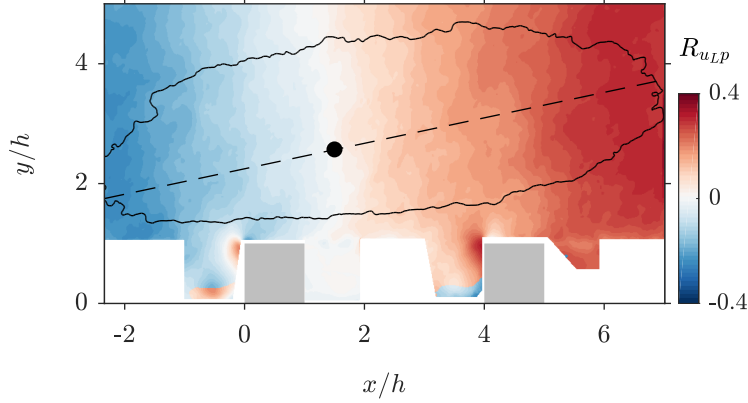
FIGURE 5.6: PRESSURE SIGNATURE OF LARGE COHERENT STRUCTURES. Correlation function between the coefficients of the first POD mode, corresponding to the large-scale streamwise velocity fluctuations, and the pressure field R_{pu_L}. An arbitrary contour line and locus of the first POD mode shape are indicated by the solid-back line and by the filled-back circle, respectively. The average inclination of the structure at 13° is given by the dashed-back line.

maxima), demarcating a region of acceleration ($\partial \mathbf{u}'/\partial \mathbf{x} > 0$) from one of deceleration ($\partial \mathbf{u}'/\partial \mathbf{x} < 0$). For example, in the advent of a low-momentum LSM, the flow experiences a local deceleration upstream from the reference point and an acceleration downstream. We may therefore conclude, tentatively, that an increase in local static pressure is associated with flow regions that exhibit a local acceleration and, conversely, a decrease in pressure is associated with regions exhibiting local decelerations. It is also evident that pressure fluctuations are greatest around the extremities of the structure, at the interface between high and low-momentum regions, where accelerations (in absolute terms) are statistically most intense. This is in agreement with figures 5.5b-d, as well as with results of Thomas and Bull (1983), who analysed the phase relationship between the velocity and surface pressure variations within a smooth-wall boundary layer. They noticed that the amplitude of the pressure fluctuations would vary with the velocity gradient across the shear layer upstream of a bursting event, if the time lag arising from its inclination angle was taken into account. It is important to highlight that although we here focus on the LSMs alone, the same trends were also observed for smaller turbulent features.

The pressure signature of the large scales additionally offers a sensible explanation for the JPDF of the fluctuating force acting on opposite sides of a cube, shown in figure 5.4b. The correlation map resembles a pressure wave whose length is several times larger than h. As it advects downstream, the forces on the windward and leeward sides fluctuate accordingly. However, since the wavelength is considerably larger than the width of a cube, the total force F varies only slightly in response to changes in background pressure from the passage of coherent structures — along the diagonal line featured in figure 5.4b, F remains unchanged. This is reflected on the correlation coefficient between u_L and F

that is only $R_{Fu_L} = 0.064$. To confirm this observation, there remains to determine if the most extreme excursions of the force on either sides of the roughness obstacle are in fact associated with this pressure mode. The force signals F_w and F_l are expected to be out-of-phase by $\pi/2$ with respect to u_L, as pressure fluctuations are larger at the interface between low and high-momentum regions. Consequently, the correlation coefficients at zero lag are relatively small ($R_{F_w u_L} = 0.063$ and $R_{F_l u_L} = 0.01$). A different approach must then be considered, which allows to circumvent the lack of phase information. This is achieved in the following section using extended proper orthogonal decomposition (EPOD) to extract the part of the pressure field correlated with each turbulent flow feature (i.e., POD mode of the velocity dataset).

5.4.2 Extended POD analysis

EPOD was formally introduced by Borée (2003) as statistical tool to analyse correlated events in turbulent flows which may or may not be of the same nature. Maurel et al. (2001), for example, investigated the jet-vortex interaction in a model engine cylinder using EPOD to identify the relevant flow phenomena driving the vortex formation. These only marginally contribute to the total kinetic energy in the flow, so POD performed over the entire domain would have not yielded useful results. In a different manner, Antoranz et al. (2018) recently used EPOD to study and quantify the contribution of velocity modes to the turbulent heat transport in a pipe flow. Their analysis is based on velocity and temperature data from a direct numerical simulation (DNS). Specifically in this context, we analyse the correlation of pressure with the projection of the velocity field on the POD modes presented in §5.2. This is possible since the pressure signal $B \in \mathbb{R}^{n_t \times n_p}$ was inferred from instantaneous snapshots of velocity data $A \in \mathbb{R}^{n_t \times n_p}$, and thereby share the same reference time frame. The extended pressure modes are obtained by projecting B onto the temporal basis Ψ_A, as in Borée (2003). It follows that

$$\Sigma_e \Phi_e^T = \Psi_A^T B, \tag{5.7}$$

where $\Sigma_e = diag(\sigma_e^{(1)}, ..., \sigma_e^r) \in \mathbb{R}^{r \times r}$ is a diagonal matrix containing the norm of the projection of B on each temporal mode of A, and $\Phi_e = [\phi_e^{(1)}, ..., \phi_e(r)] \in \mathbb{R}^{n_p \times r}$ are the EPOD modes of pressure. Note that the square of $\sigma_e^{(i)}$ accounts only for the part of the pressure variance correlated with the temporal mode (i) of the velocity signal, providing a measure of the magnitude of the pressure fluctuations associated with each turbulent scale.

The shape of the first EPOD mode $\phi_e^{(1)}$, represented in figure 5.7a, is unsurprisingly similar to the correlation function R_{pu_L}. Comparing with the first POD mode $\phi^{(1)}$, depicted in figure 5.1a, it becomes clear that the pressure field is positive correlated with the streamwise component of the velocity fluctuations downstream of the coherent
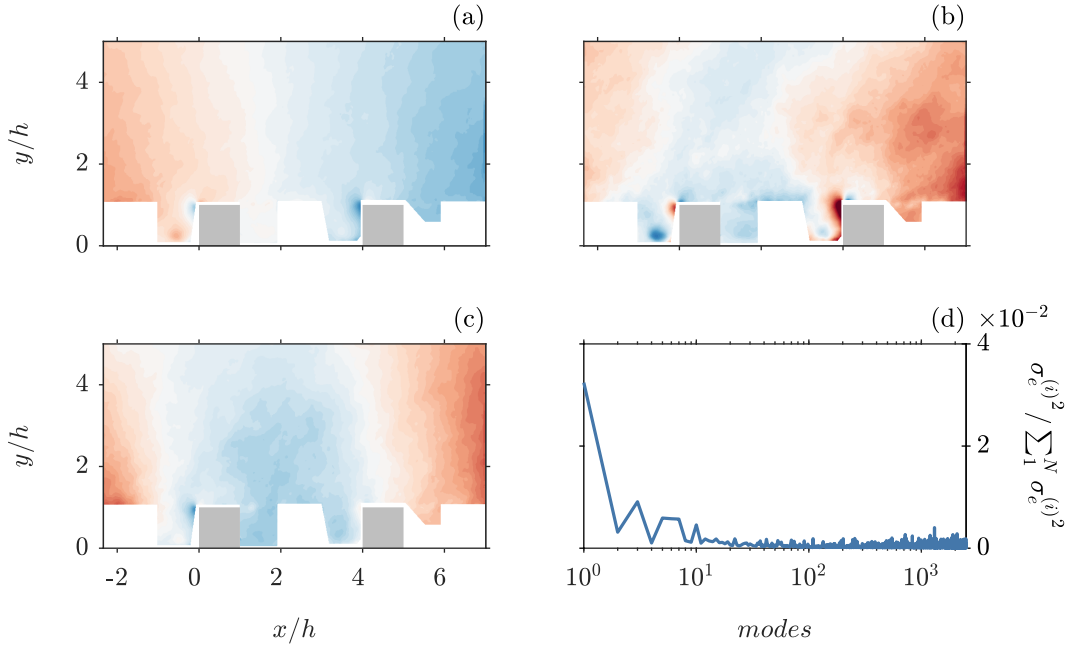
FIGURE 5.7: EXTENDED POD MODES OF PRESSURE. First three extended pressure modes on the velocity basis, $\phi_e^{(1)}$ **(a)**, $\phi_e^{(2)}$ **(b)** and $\phi_e^{(3)}$ **(c)**. The red and blue-shaded regions correspond to positive and negative pressure fluctuations, respectively. **(d)** The relative contribution of the EPOD modes to the total pressure variance.

structure, but instead exhibits an anti-signed behaviour upstream. This relationship is noticeable too for higher-order modes, albeit to a lesser extent. Shown in figure 5.7d, the relative contribution of $\phi_e^{(1)}$ to the total pressure variance is by far the largest, exceeding tenfold that of the second mode. Considering the strong correlation between the forces acting on the windward and leeward sides of a cube ($R_{F_w F_l} = 0.59$), as well as the pressure signature of the LSMs, this convincingly shows that the most extreme excursions of these forces are the imprint of a broad advecting pressure wave associated with the passage of alternating high and low momentum regions. As a first-order approximation $R_{F_w F_l} \propto L_x/h$, suggesting that the significance of the large coherent structures to surface drag is mitigated by the relatively small size of the obstacles compared to the integral length scale. In a different context, Cameron et al. (2019) recently reported a possibly related observation. They found that for small protrusions of a bed particle in open-channel flows (that could be thought of as a densely packed cube array), the high-frequency region of the drag force spectra contributes the most to the total variance, while the direct contribution of the low-frequency range, corresponding to the characteristic frequencies of the large turbulent scales, is relatively small. They may nonetheless be important to surface drag, as the results also suggest they interact with the high-frequency component of the force through a process of amplitude modulation. This will be investigated in the following section.

The current EPOD analysis further allows to identify the relevant flow dynamics

that contribute the most to pressure fluctuations. To illustrate, let us consider the POD modes $\phi^{(2)}$ and $\phi^{(3)}$ (figures 5.1b-c) that correspond to events of smaller wavelength. They are are essentially orthonormal: The first is preferentially aligned horizontally and the second along the wall-normal direction. When superimposed on the first mode, they cause the LSM to shift perpendicularly to their principal direction. Since the EPOD mode $\phi_e^{(2)}$ is relatively weaker than $\phi_e^{(3)}$, as indicated in figure 5.7d, it appears that the passage of alternating high and low momentum regions within the roughness sublayer (associated with an horizontal shift) contributes the most to the pressure fluctuations, while the contribution from a vertical motion is comparably less significant. In a similar manner, $\sigma_e^{(4)} < \sigma_e^{(5)}$.

5.4.3 Implications of amplitude modulation

In light of recent the developments on inter-scale dynamics within turbulent boundary layers (Mathis et al., 2009; Hutchins et al., 2011; Basley et al., 2018), and the evidence that the LSMs potentially interact with the high-frequency part of the drag force of bed particles (Cameron et al., 2019), we investigate their effect on the local (i.e. small scale) pressure fluctuations, and attempt to provide a qualitative description of the mechanisms responsible for drag generation.

Figure 5.8a shows a distribution plot of the data, with the force acting on the target obstacle F' along the horizontal axis and the large-scale streamwise velocity fluctuations u'_L on the vertical axis. The first striking feature is that high and low momentum regions are both likely to produce negative and positive drag fluctuations of comparable intensity. The direct contribution of the large coherent motions to drag fluctuations is associated with quadrants 2 and 4 — when $u'_L > 0$ then $\partial p/\partial x > 0$, yielding $F' < 0$ (and vice versa) — but thus far, the current data seem to suggest that its significance is not as important as the contribution of more compact, isotropic structures. These are possibly related with sweeps and ejections on the order of the canopy scale that contribute to the Reynolds shear stresses, and finer vortical motions populating the shear layer. The symmetry of the scattered data along the vertical axis supports this conclusion, because it suggests that the nature of the dominant processes driving positive and negative drag events are essentially the same.

Although there is a weak correlation between u'_L and F', the most extreme excursions of the force appear to be preferentially aligned with high momentum large-scale events. This is clearly evident by comparing the conditional PDF of the force in the presence of a negative or positive LSM, $f_F(F' \mid u'_L < 0)$ and $f_F(F' \mid u'_L > 0)$, respectively. The first distribution is visibly narrower, specifically, force fluctuations greater than σ_F in absolute terms are nearly 30% more likely to be associated with a positive large-scale event. The existence of an interaction mechanism of AM could explain this observation, whereby the local pressure fluctuations induced by the small-scale dynamics would be
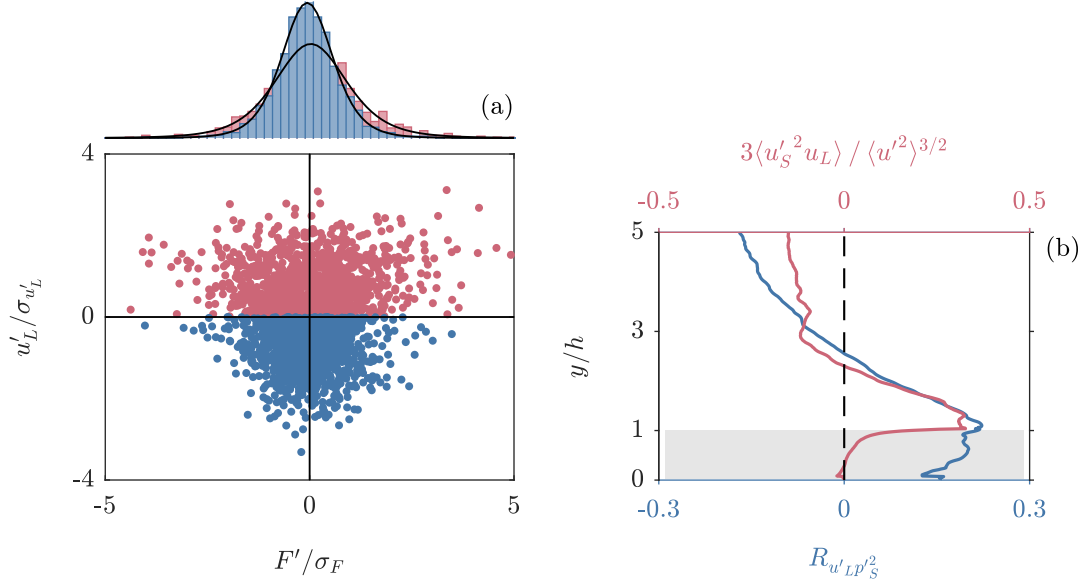
FIGURE 5.8: EFFECT OF AMPLITUDE MODULATION. **(a)** Scatter plot of the data with force fluctuations F' on the x-axis and the large-scale component of the streamwise velocity u'_L on the y-axis. Above are the PDFs of the force conditionally averaged on a high (red) and low (blue) momentum LSM. **(b)** Wall-normal distributions of the correlation coefficient $R_{u_L p_S^2}$ on the bottom axis (blue) and the cross-term $\langle u'^2_s u'_L \rangle$ of the scale-decomposed skewness factor on the top axis (red).

amplified or attenuated along with the turbulent kinetic energy. We test this hypothesis first, by decomposing the fluctuating pressure field into large and small scales using POD, in the same manner as detailed in §5.2 for the streamwise velocity component. Accordingly, the pressure signal of the small scales $p'_S = p' - p'_L$. The pressure signal from the largest scales p'_L is approximated by the linear combination of the first two POD modes, because the second pressure mode shape $\phi_B^{(2)}$ was found to match the first EPOD mode shape $\phi_e^{(1)}$, which is presumably the footprint of the large-scale velocity structures (refer to figure 5.6). Second, following an equivalent approach to that outlined by Mathis et al. (2011b), a measure of the modulation effect is obtained by computing the correlation coefficient

$$R_{u_L p_S^2}(\mathbf{x}) = \langle u'_L(\mathbf{x},t)\, p'^2_S(\mathbf{x},t) \rangle \,/\, (\sigma_{u_L}(\mathbf{x})\, \sigma_{p_S^2}(\mathbf{x})). \tag{5.8}$$

In contrast to the filtered envelope of the small-scale pressure fluctuations, p'^2_S accounts not only for the potential large-scale modulation but also for the small-scale variance. Despite this limitation, a more precise description of this interaction could only be achieved with synchronous, time-resolved measurements of the velocity and pressure fields, which are not yet available. The wall-normal evolution of the correlation function is shown in figure 5.8b, overlaid by the cross term $\langle u'^2_s u'_L \rangle$ of the scale-decomposed skewness factor. The correlation value marginally increases across the canopy, reaching

a positive peak around the shear-layer interface. It then monotonically decreases with height and becomes negative in the outer region of the boundary layer. Remarkably, $R_{u_L p_S^2}$ closely traces the evolution of the cross term $\langle u_s'^2 u_L' \rangle$, exhibiting a peak and zero-crossing at the same locations. The qualitative similarity between the profiles indicates that the AM of the small-scale pressure fluctuations and turbulent kinetic energy are fundamentally coupled around the near-canopy region. Below the shear layer, however, the correlation function is non-zero despite the sheltering it provides from the flow above. This is an important aspect because it illustrates how the high-frequency component of the drag force may likely be modulated. The fact that the shear layer interface does not prevent AM of the small-scale pressure signal, as it does with the turbulent kinetic energy, is possibly related with the nonlocal nature of the pressure field (Tsinober, 2001), which may depend on flow dynamics far from the point under consideration. Pressure fluctuations within the canopy are then subject to the direct influence of the overlying turbulent motions and, as a result, so are the forces acting on the windward and leeward sides of the roughness obstacles.

5.5   Further discussion and conclusion

PIV measurements of the boundary layer over a staggered-cube array were used to obtain a description of the underlying pressure field and surface drag characteristics via 2D-TH. POD of the flow field revealed large coherent motions in the near-wall region that coexist with structures of similar energy and characteristics, yet of smaller scale, from which arises the two-scale behaviour of the two-point velocity correlations (e.g. Reynolds and Castro, 2008; Basley et al., 2019). Statistics of the force acting on a target roughness obstacle exhibit extreme excursions from the mean value, with recurring thrust-producing events. More importantly, the strong correlation between the forces on the windward and leeward sides implies the existence of a coupling mechanism driven by a large-scale, advecting pressure wave whose direct contribution to surface drag is not as significant as that of less intense, anti-signed events (e.g. $F_w' > 0 \cap F_l' < 0$). A conditional analysis was performed to understand the relationship of these events with the turbulent structure of the boundary layer. We identified distinct flow patterns responsible for positive and negative drag fluctuations. The first is dominated by the presence of a forward-leaning high-momentum region impinging on the windward side of the cube, leading to a local increase in pressure. In contrast, the second features an inclined shear layer squeezed in-between an upstream, high-speed sweep and a downstream, low-speed ejection. This is often referred to as a bursting event, and in agreement with the current results, it has been shown to have a broad effect on the pressure field of smooth-wall boundary layers (Thomas and Bull, 1983). Force fluctuations may thus arise not only from momentum-driven processes, but also due to violent inward-outward flow interac-

tions high above the canopy. It is observed that high-momentum regions, in particular Q4 events, generally experience an adverse pressure gradient, with prevailing negative and positive fluctuations upstream and downstream from the locus of the coherent motion, respectively. Conversely, low-momentum regions, or Q2 events, are associated with favourable pressure gradients. The cross-over point in pressure is approximately aligned with the local extrema of the velocity fluctuations (i.e. a local maxima/minima for high/low momentum regions). So it is possible that an increased pressure region is associated with flow features that exhibit a local streamwise deceleration, and conversely a decreased pressure region is associated with a local acceleration. The pressure signature of the large scales is consistent with the hypothesis of an advecting pressure wave inducing extreme force fluctuations on opposite sides of the roughness obstacles. A combined analysis of the POD modes of velocity and the corresponding EPOD modes of pressure confirmed that the large-scale velocity structures have a significant influence on the magnitude of the total pressure fluctuations. However, their direct impact on surface drag appears to be mitigated by the relative size of the roughness obstacles h/L_x, which is considerably smaller in comparison. We additionally found convincing evidence that the small-scale turbulent pressure fluctuations are influenced by the passage of outer layer large-scale events through a mechanism that could be AM. Notably, the criteria used to quantify this interaction is non-negligible within the canopy, so it seems that the high-frequency force fluctuations are implicitly modulated. This conclusion is in agreement with recent findings of Cameron et al. (2019), who investigated the velocity-drag interrelation on bed-particle flows.

In the same manner as in smooth-wall boundary layers, surface drag arises over rough walls from a superposition of events at different scales interacting with each other. This behaviour is intrinsic to all high-Reynolds number wall-bounded turbulence (Marusic et al., 2010), but despite their common features, the mechanisms responsible for drag generation are fundamentally different as a result of the surface geometry. For example, we find that positive and negative fluctuations of the force acting on a roughness obstacle are equally likely to occur irrespective of the large-scale signal, whereas over smooth walls the latter has been shown to be correlated with extreme shear-stress events (Hutchins et al., 2011). In this work, the influence of the large scales on surface drag only becomes apparent by examining the magnitude of the force fluctuations, which are amplified and attenuated in the presence of high and low momentum regions, respectively. To achieve a more precise description of this interaction, and to identify the relevant flow phenomena to surface drag, it would be advantageous to obtain synchronous measurements of the pressure on the surface of a roughness obstacle and the surrounding velocity field. Alternatively, a more complex experimental setup using time-resolved, thin-volume tomographic PIV would improve the uncertainty associated with pressure reconstruction methods.

Chapter 6

Summary and outlook

The present thesis tackled some of the current challenges in understanding and modelling the turbulent flow processes over urban areas. As outlined in chapter 1, the limited Reynolds numbers at which experiments and simulations are often carried out and the large relative roughness height (h/δ), characteristic of urban-like roughness, often render inadequate key generalisations about the flow structure, as well as established analysis methods. Additional complications have to do with the pressure-based nature of the surface drag and the complex geometry of real urban environments that limit application of traditional measurement techniques in the canopy layer. Low-order models of urban boundary layers are therefore favoured over field measurements or scaled models of a particular area of interest, because they can be effectively probed and allow for parametric studies. Particularly, we considered the flow over two staggered arrays of cuboids, with the same plan arrangement, but different height distributions: uniform (C10U) and random (C10R). The first had already been extensively investigated (numerically and experimentally), so existing data were used to validate the current approach. The main findings are summarised in this chapter.

6.1 An alternative floating element design for skin-friction measurement of turbulent wall flows

An accurate estimation of the surface drag is essential for any description of wall-bounded flows. Some of the most popular techniques are based on velocity measurements, but prove to be unreliable when similarity laws do not hold. This is generally the case of boundary layers developing over very-rough surfaces with $h/\delta > 0.2$ (e.g. urban areas) or heterogeneous roughness, which exhibit discontinuities in surface characteristics whose length scale is on the order of the boundary-layer thickness δ. The lack of accuracy of indirect methods for very-rough surfaces is evident by comparing the values reported in the extensive literature on the staggered-cube array C10U: the variability in norm-

alised friction velocity u_τ/U_0 is about 16% of the mean value. In chapter 2 we sought
to overcome this shortfall that could have otherwise undermined following analysis. We
proposed a floating element (FE) device featuring a pair of longitudinal-force trans-
ducers and an additional pair of pitching-moment transducers. Its unique design, in
combination with a centrifugal blower, allows to actively eliminate the negative effect of
transverse sensitivity of the force transducers to vertical loads. Measurements of skin-
friction coefficient for a smooth-wall boundary layer were used to assess the accuracy of
the balance. The results compare well with values inferred from hot-wire anemometry
and with the empirical skin-friction relationship of Österlund et al. (2000), to within
2% for $Re_\theta > 4 \times 10^3$. A detailed uncertainty analysis revealed that the largest error
sources are associated with calibration and drag evaluation methods, and the tilt angle
of the FE relative to the wind-tunnel floor. Finally, measurements of the skin-friction
coefficient for C10U reveled that, at the measurement location, the boundary layer was
fully rough over the entire range of Reynolds number. Notably, the variability of the
data around the mean value is only 2%.

Since its deployment, the FE has been reliably used to test a variety of different
surface roughness, and the setup in the wind tunnel and calibration method have been
streamlined.

6.2 The pressure field within the canopy of urban-like roughness: an experimental approach

Estimates of the pressure field above and within the canopy layer were obtained from
snapshots of planar particle image velocimetry (PIV) using the reconstruction methods
2D-RANS and 2D-TH. The benefit of this approach is two-fold: it provides a detailed
description of the surface pressure over the roughness obstacles, from which important
boundary-layer parameters may be inferred; and it could potentially facilitate identi-
fying the turbulent mechanisms responsible for drag generation. The latter may only
be achieved with synchronous measurements of drag force, velocity and the overlying
pressure field that are otherwise difficult to obtain experimentally.

It is emphasized that there are limitations to these techniques associated with the
nature of the PIV data, which does not capture the out-of-plane velocity and accelera-
tion components. This is especially detrimental within the canopy layer where the flow
is highly three-dimensional, owing to the presence of the roughness elements. Although
it is not possible to accurately quantify the error induced by the missing terms, empir-
ical analysis suggest that this is the primary source of uncertainty — about an order of
magnitude larger than that associated with noise propagation from velocity data. As
an alternative to estimating uncertainty via statistical methods, we followed a *type-B*
evaluation strategy by comparing mean surface pressure and root-mean-square (RMS)

distributions obtained from each reconstruction method, as well as against reported wind tunnel measurements and numerical simulations. We found discrepancies between the mean pressure maps of C10U, obtained using 2D-RANS and 2D-TH (averaging over 2500 snapshots), that were not uniform across the entire field-of-view (FOV) and appeared to be confined to a small region. Their cause has not been fully investigated in this work, but it may likely be due to noise propagation and the sensitivity of the Poisson solver to Neumann boundary conditions. Mean axial-pressure differences across target roughness elements in both arrays of cuboids are comparable with previously reported data, to within 5% of the average value. Furthermore, despite the lack of a meaningful scaling factor and disparity in Reynolds number, the RMS-pressure distribution on the windward and leeward sides of a cube (C10U) are in qualitative agreement with large eddy simulation (LES). The actual RMS error of the instantaneous pressure fields could not be determined as it depends on the RMS ratio between the estimated and reference pressure signals (e.g. taken on the surface of the roughness elements) and on the correlation coefficient between them (Van der Kindere et al., 2019).

Estimates of friction velocity and zero-plane displacement height were obtained for both surfaces, by integrating the pressure distribution around the roughness obstacles. The underlying assumptions are that the viscous contribution represents a small portion of the total surface drag, and that the axial-pressure difference across the roughness obstacles is spanwise uniform. In fact, results from direct numerical simulation (DNS) of Leonardi and Castro (2010) showed that the viscous wall stresses do not exceed 7% of the total drag at a lower Reynolds number for C10U. The values of friction velocity from pressure underestimated those obtained using the FE by $3 - 7\%$ (around 2% for C10R) depending on the reconstruction method, suggesting, as expected, a smaller relative contribution of the viscous terms. Estimates of the zero-plane displacement were also consistent with simulations and experimental data. Notably, the reported value for C10R by Xie et al. (2008), inferred from the mean streamwise velocity profile, exceeded by far the average height H. Given the large uncertainty associated with this method, we instead used their LES data to estimate the displacement height based on the pressure distribution, yielding a similar result to that of the reconstructed pressure data.

It is remarkable that, in spite of the limitations of 2D reconstruction methods, they could still be used reliably to obtain a more complete description of the turbulent flow field. Notwithstanding the associated uncertainty, estimates of the friction velocity and the zero-plane displacement appeared to be more accurate that those obtained via an ill-conditioned three-parameter fit of the log law or the total-stress method. So the current approach could also prove useful to estimate the boundary-layer flow parameters when a direct measurement technique is not available. Some of its shortcomings could be mitigated with a more sophisticated experimental setup, namely using thin-volume tomographic PIV to capture the missing components of velocity and acceleration and a

refractive-index matched facility to eliminate reflections off the surface of the roughness obstacles.

6.3   On the sectional-drag profile of urban-canopy layers

In chapter 4 we discussed the importance of urban canopy models, which attempt to characterise the mean boundary-layer flow based on the surface morphology, and the validity of their assumptions. Specifically, quasi-empirical formulations rest on the principle of outer-layer similarity that was verified for both arrays of cuboids up to second-order statistics, and on the existence of an equilibrium layer. They make additional assumptions about the turbulent structure of the flow within the canopy — negligible contribution of the dispersive stresses to the vertical transport of momentum, constant mixing length l_m and sectional drag coefficient C_D — that appear to be inaccurate, as demonstrated by several authors (Reynolds and Castro, 2008; Barlow and Coceal, 2008; Castro, 2017). The current experiment supported this observation. Although field measurements in the canopy layer were partially obstructed by out-of-plane roughness elements, the horizontally-averaged mean statistics were not significantly affected and are comparable to DNS data. The exponential velocity profile that follows from the aforementioned assumptions was not verified and the mixing-length scale and sectional-drag coefficients were found to vary considerably across the canopy height.

Recently, different formulations have been proposed to relax these requirements. Of particular interest is that by Yang et al. (2016); it defines expressions for the velocity profile on an ad-hoc basis prescribed by a wake-sheltering model, so it does not explicitly parameterise the mixing-length within the canopy, enjoying increased versatility. While most methodologies differ from one another for the shape function of the velocity profile, they invariably assume a constant sectional-drag coefficient. To circumvent this limitation, we proposed an alternative approach that exploits the apparent self-similar behaviour of the axial-pressure difference across individual roughness elements. Results showed that the sectional-drag profile Δp could be described by a functional relationship, governed by a non-dimensional scaling parameter expressed as $\lambda_P U_h^+$, which presumably embodies the effect of the shear layer on the canopy flow topology. The functional relationship depends on the location and intensity of the local extrema of Δp that were linearly correlated with $\lambda_P U_h^+$, except for the height of the local minima. The intensity of the local maxima increases with the strength of the shear layer at a faster rate than that of the local minima, while its location remains approximately unchanged. The height of the local minima, on the other hand, appears to be prescribed by the size of the frontal recirculating region of the cuboids (or sheltered-layer height), which in turn depends on additional geometric parameters such as the plan arrangement and their aspect ratio and height distribution. This particular aspect remains to be further

investigated.

The shape function of the axial-pressure difference, defined as a piecewise third-order polynomial, was able to reproduce the profiles given two parameters: the non-dimensional shear factor $\lambda_P U_h^+$ and a sheltered-layer height h_s. Moreover, it captured the change from skewed distributions for obstacles that stand above the average height to more uniform distributions for those lying in their wake. If used in the framework of a wake-sheltering model, like those of Millward-Hopkins et al. (2013) or Yang et al. (2016), this methodology could potentially provide a better description of the mean canopy flow. There is naturally some uncertainty stemming from the large variability around the correlation functions, nevertheless it might still improve the accuracy of current formulations.

6.4 Scale interactions in velocity and pressure over a staggered cube array

We investigated the surface-drag characteristics of C10U and its relationship with the turbulent structure of the overlying flow. Published work on large-scale roughness had generally focused on universal scale interactions that were first observed in smooth-wall boundary layers or sought to document the impact of surface geometry on flow statistics. However, the mechanisms responsible for drag generation had not yet been identified. This is largely because of the discrete nature of the of surface drag that is locked onto the roughness obstacles, so it cannot be described on a local basis. It is also experimentally difficult, or even impossible, to obtain synchronous measurements of velocity and pressure that could allow drawing conclusions about the interrelation between drag forces and turbulent flow phenomena. As a workaround, the force acting on a target roughness obstacle was inferred from velocity data via 2D-TH and used as a proxy for the local wall-shear stress. From Van der Kindere et al. (2019), the correlation between the reconstructed pressure signal and the actual value is on the order of 0.5. The lack of correlation potentially affected the significance of the statistical analysis but likely not the outcome of their results.

The probability density function (PDF) of the net force acting on a target roughness element exhibited a Gaussian distribution with frequent negative-drag or thrust-producing events. The position of the centre of pressure also showed a broad distribution, skewed towards the canopy top, suggesting that the local flow topology undergoes dramatic changes. Specifically, extreme positive force fluctuations tend to act at half-cube height, while less intense and negative events act near the edge and on the lower half of the cube, respectively. Force fluctuations on the windward F_w and leeward F_l faces are equally significant and revealed a strong correlation. We hypothesise that this is the imprint of a large advecting pressure wave that evenly affects both sides of the roughness

elements, so the less intense anti-signed events, presumably associated with small and intermediate scales, produce the largest net force fluctuations. Conditionally averaging the velocity and pressure fields based on the loading combination (F_w, F_l), we identified the most prominent flow patterns that produce the most extreme excursions of the force. They fall in two categories: It could either be a momentum-driven process which occurs when a large-scale motion impinges on the surface roughness — a low-momentum region (LMR) leads to a relative decrease in pressure on the windward side of the cube and, conversely, a high-momentum region (HMR) to a local increase — or a result of violent inward-outward interactions, charaterised by an inclined shear layer that may traverse most of the boundary-layer thickness. For example, the interaction between an upstream high-speed sweep and a downstream low-speed ejection will cause an increase in pressure as the fluid is squeezed along the interface. Regardless of the flow process, these turbulent structures convect downstream, so their footprint is essentially perceived as a pressure wave.

The signature of the large-scale features on the pressure field was further evidenced by the extended proper orthogonal decomposition (EPOD) analysis. We found that the amplitude of the pressure fluctuations they induce would vary according to the local velocity gradient, so HMRs would typically experience adverse pressure gradients (a decrease in pressure upstream of the locus point and an increase downstream) and LMRs favourable pressure gradients. Additionally, the variance of the pressure fluctuations associated with the large coherent structures was more significant than that of smaller scale motions. Therefore, in view of the statistical analysis of the drag force, we concluded that the direct contribution of the largest structures is mitigated by the relatively smaller size of the roughness elements, as the forces on the windward and leeward sides partially cancel each other out. While their direct influence on the surface drag might be smaller than would be expected (they are the primary contributor over smooth walls), the results suggested that they still play an important role in modulating the kinetic energy and pressure fluctuations of the small-scale features in the near-wall region. This would then explain why the most extreme excursions of the net force are preferentially aligned with HMR.

6.5   Outlook

- The FE design can be refined to improve reliability and reduce the uncertainty associated. This can possibly be achieved using air-bearings to mechanically decouple the streamwise load and/or using a zero-displacement force sensor as opposed to the traditional strain-gauge force transducers that are inherently sensitive to creep and off-axis loading.

- The potential of using pressure estimation methods to achieve a more complete

description of flows over urban areas is well supported by the present research, but the performance of 2D-TH to obtain instantaneous pressure data has not yet been quantified given the lack of synchronous measurements from reference surface-mounted transducers. These are typically larger than the dimensions of the cuboids, so it would be necessary to scale up the experiment in a larger facility.

- Additional quality data is necessary to confirm (or disprove) the scaling arguments presented in chapter 4 and it is left to determine if the location of the lower peak of the axial-pressure distribution across the cuboids can be described by a wake-sheltering model. Only then may the proposed functional relationship be integrated in a canopy model and its performance evaluated.

- Unless 2D-TH is validated, the analyses presented in chapter 5 of the interrelation between the surface roughness and the turbulent structure of the flow would benefit from synchronous, time resolved measurements of the surface pressure and the surrounding velocity field. The boundary-layer flow (velocity and pressure) could then be decomposed on a scale basis, rather than on an energy basis using POD, and it would possible to obtain a more accurate description of the mechanism of amplitude modulation, especially that of the small-scale pressure signal by the LSM within the canopy. Finally, an equivalent study should be carried out for the staggered array of cuboids C10R to understand the impact height variability.

Bibliography

Abbassi, M., Baars, W., Hutchins, N., and Marusic, I. Skin-friction drag reduction in a high-Reynolds-number turbulent boundary layer via real-time control of large-scale structures. *International Journal of Heat and Fluid Flow*, 67:30–41, 2017.

Abe, H., Kawamura, H., and Choi, H. Very large-scale structures and their effects on the wall shear-stress fluctuations in a turbulent channel flow up to reτ= 640. *Journal of fluids engineering*, 126(5):835–843, 2004.

Acharya, M., Bornstein, J., Escudier, M. P., and Vokurka, V. Development of a floating element for the measurement of surface shear stress. *AIAA Journal*, 23:410–415, 1985.

Adrian, R. J., Meinhart, C. D., and Tomkins, C. D. Vortex organization in the outer region of the turbulent boundary layer. *Journal of Fluid Mechanics*, 422:1–54, 2000.

Alfredsson, P. H., Johansson, A. V., Haritonidis, J. H., and Eckelmann, H. The fluctuating wall-shear stress and the velocity field in the viscous sublayer. *The Physics of fluids*, 31(5):1026–1033, 1988.

Allen, J. M. H. Experimental study of error sources in skin-friction balance measurements. *Journal of Fluids Engineering*, 99:197–204, 1977.

Allen, J. M. H. Improved sensing element for skin-friction balance measurements. *AIAA Journal*, 18:1342–1345, 1980.

Amir, M. and Castro, I. P. Turbulence in rough-wall boundary layers: universality issues. *Experiments in fluids*, 51(2):313–326, 2011.

Anderson, W. Amplitude modulation of streamwise velocity fluctuations in the roughness sublayer: evidence from large-eddy simulations. *Journal of Fluid Mechanics*, 789: 567–588, 2016.

Antonia, R. A. and Krogstad, P.-Å. Turbulence structure in boundary layers over different types of surface roughness. *Fluid Dynamics Research*, 28:139–157, 2001.

Antonia, R. A. and Luxton, R. E. The response of a turbulent boundary layer to a step change in surface roughness part 1. smooth to rough. *Journal of Fluid Mechanics*, 48: 721–761, 1971.

Antoranz, A., Ianiro, A., Flores, O., and García-Villalba, M. Extended proper orthogonal decomposition of non-homogeneous thermal fields in a turbulent pipe flow. *International Journal of Heat and Mass Transfer*, 118:1264–1275, 2018.

Aubry, N., Guyonnet, R., and Lima, R. Spatiotemporal analysis of complex signals: theory and applications. *Journal of Statistical Physics*, 64(3-4):683–739, 1991.

Baars, W. J., Squire, D. T., Talluru, K. M., Abbassi, M. R., Hutchins, N., and Marusic, I. Wall-drag measurements of smooth- and rough-wall turbulent boundary layers using a floating element. *Experiments in Fluids*, 57(5):90, 2016a.

Baars, W. J., Hutchins, N., and Marusic, I. Spectral stochastic estimation of high-Reynolds-number wall-bounded turbulence for a refined inner-outer interaction model. *Physical Review Fluids*, 1(5):054406, 2016b.

Barlow, J. and Coceal, O. A review of urban roughness sublayer turbulence. 2008.

Basley, J., Perret, L., and Mathis, R. Spatial modulations of kinetic energy in the roughness sublayer. *Journal of Fluid Mechanics*, 850:584–610, 2018.

Basley, J., Perret, L., and Mathis, R. Structure of high Reynolds number boundary layers over cube canopies. *Journal of Fluid Mechanics*, 870:460–491, 2019.

Baur, T. PIV with high temporal resolution for the determination of local pressure reductions from coherent turbulence phenomena. In *Proc. 3rd Int. Workshop on PIV-Santa Barbara*, pages 101–106, 1999.

Benedict, L. H. and Gould, R. D. Towards better uncertainty estimates for turbulence statistics. *Experiments in Fluids*, 22:129–136, 1996.

Berkooz, G., Holmes, P., and Lumley, J. L. The proper orthogonal decomposition in the analysis of turbulent flows. *Annual review of fluid mechanics*, 25(1):539–575, 1993.

Bhaganagar, K., Kim, J., and Coleman, G. Effect of roughness on wall-bounded turbulence. *Flow, turbulence and combustion*, 72(2-4):463–492, 2004.

BIPM, IEC, IFCC, ILAC, ISO, IUPAC, IUPAP, and OIML. Guide to the expression of uncertianty in measurement. *Joint Committee for Guides in Metrology*, 10:2008, 2008. GUM 1995 with minor corrections.

Blackman, K. and Perret, L. Non-linear interactions in a boundary layer developing over an array of cubes using stochastic estimation. *Physics of Fluids*, 28(9):095108, 2016.

Böhm, M., Finnigan, J. J., Raupach, M. R., and Hughes, D. Turbulence structure within and above a canopy of bluff elements. *Boundary-layer meteorology*, 146(3):393–419, 2013.

Borée, J. Extended proper orthogonal decomposition: a tool to analyse correlated events in turbulent flows. *Experiments in fluids*, 35(2):188–192, 2003.

Brown, K. C. and Joubert, P. N. The measurement of skin friction in turbulent boundary layers with adverse pressure gradients. *Journal of Fluid Mechanics*, 35(4):737–757, 1969.

Cameron, S., Nikora, V., and Marusic, I. Drag forces on a bed particle in open-channel flow: effects of pressure spatial fluctuations and very-large-scale motions. *Journal of Fluid Mechanics*, 863:494–512, 2019.

Castro, I. P. Are urban-canopy velocity profiles exponential? *Boundary-Layer Meteorology*, 164(3):337–351, 2017.

Castro, I. P., Cheng, H., and Reynolds, R. Turbulence over urban-type roughness: deductions from wind-tunnel measurements. *Boundary-Layer Meteorology*, 118(1): 109–131, 2006.

Castro, I. P., Segalini, A., and Alfredsson, P. H. Outer-layer turbulence intensities in smooth-and rough-wall boundary layers. *Journal of Fluid Mechanics*, 727:119–131, 2013.

Castro, I. and Fackrell, J. A note on two-dimensional fence flows, with emphasis on wall constraint. *Journal of Wind Engineering and Industrial Aerodynamics*, 3(1):1–20, 1978.

Castro, I. and Robins, A. The flow around a surface-mounted cube in uniform and turbulent streams. *Journal of fluid Mechanics*, 79(2):307–335, 1977.

Charonko, J. J., King, C. V., Smith, B. L., and Vlachos, P. P. Assessment of pressure field calculations from particle image velocimetry measurements. *Measurement Science and Technology*, 21(10):105401, 2010.

Chauhan, K. A., Monkewitz, P. A., and Nagib, H. M. Criteria for assessing experiments in zero pressure gradient boundary layers. *Fluid Dynamics Research*, 41:021404, 2009.

Cheng, H. and Castro, I. P. Near wall flow over urban-like roughness. *Boundary-Layer Meteorology*, 104:229–259, 2002.

Cheng, H., Hayden, P., Robins, A., and Castro, I. Flow over cube arrays of different packing densities. *Journal of Wind Engineering and Industrial Aerodynamics*, 95(8): 715–740, 2007.

Claus, J., Coceal, O., Thomas, T. G., Branford, S., Belcher, S. E., and Castro, I. P. Wind-direction effects on urban-type flows. *Boundary-Layer Meteorology*, 142:265–287, 2012a.

Claus, J., Krogstad, P.-Å., and Castro, I. P. Some measurements of surface drag in urban-type boundary layers at various wind angles. *Boundary-Layer Meteorology*, 145:407–422, 2012b.

Clauser, F. H. The turbulent boundary layer. In *Advances in applied mechanics*, volume 4, pages 1–51. Elsevier, 1956.

Coceal, O. and Belcher, S. A canopy model of mean winds through urban areas. *Quarterly Journal of the Royal Meteorological Society*, 130(599):1349–1372, 2004.

Coceal, O., Thomas, T. G., and Belcher, S. E. Spatial variability of flow statistics within regular building arrays. *Boundary-layer meteorology*, 125(3):537–552, 2007.

Coles, D. *Measurements in the boundary layer on a smooth flat plate in supersonic flow.* PhD thesis, California Institute of Technology, Pasadena, CA, 1953.

Coles, D. The law of the wake in the turbulent boundary layer. *Journal of Fluid Mechanics*, 1:191–226, 1956.

De Graaff, D. B. and Eaton, J. K. Reynolds-number scaling of the flat-plate turbulent boundary layer. *Journal of Fluid Mechanics*, 422:319–346, 2000.

De Kat, R. and Van Oudheusden, B. Instantaneous planar pressure determination from PIV in turbulent flow. *Experiments in fluids*, 52(5):1089–1106, 2012.

de Kat, R. and Ganapathisubramani, B. Pressure from particle image velocimetry for convective flows: a taylor's hypothesis approach. *Measurement Science and Technology*, 24(2):024002, 2013.

Dhawan, S. *Direct measurements of skin friction.* PhD thesis, California Institute of Technology, Pasadena, CA, 1951.

Di Sabatino, S., Solazzo, E., Paradisi, P., and Britter, R. A simple model for spatially-averaged wind profiles within and above an urban canopy. *Boundary-layer meteorology*, 127(1):131–151, 2008.

Discetti, S., Bellani, G., Örlü, R., Serpieri, J., Vila, C. S., Raiola, M., Zheng, X., Mascotelli, L., Talamelli, A., and Ianiro, A. Characterization of very-large-scale motions in high-re pipe flows. *Experimental Thermal and Fluid Science*, 104:1–8, 2019.

Djenidi, L., Elavarasan, R., and Antonia, R. The turbulent boundary layer over transverse square cavities. *Journal of Fluid Mechanics*, 395:271–294, 1999.

Dogan, E., Hanson, R. E., and Ganapathisubramani, B. Interactions of large-scale freestream turbulence with turbulent boundary layers. *Journal of Fluid Mechanics*, 802: 79–107, 2016.

Esteban, L. B., Dogan, E., Rodríguez-López, E., and Ganapathisubramani, B. Skinfriction measurements in a turbulent boundary layer under the influence of free-stream turbulence. *Experiments in Fluids*, 58:115, 2017.

Fackrell, J. Parameters characterising dispersion in the near wake of buildings. *Journal of Wind Engineering and Industrial Aerodynamics*, 16(1):97–118, 1984.

Ferreira, M. A., Rodríguez-López, E., and Ganapathisubramani, B. An alternative floating element design for skin-friction measurement of turbulent wall flows. *Experiments in Fluids*, 59:155, 2018.

Flack, K., Schultz, M., and Connelly, J. Examination of a critical roughness height for outer layer similarity. *Physics of Fluids*, 19(9):095104, 2007.

Flack, K. A. and Schultz, M. P. Review of hydraulic roughness scales in the fully rough regime. *Journal of Fluids Engineering*, 132(4), 2010.

Flack, K. A., Schultz, M. P., and Shapiro, T. A. Experimental support for townsend's Reynolds number similarity hypothesis on rough walls. *Physics of Fluids*, 17(3): 035102, 2005.

Frei, D. and Thomann, H. Direct measurements of skin friction in a turbulent boundary layer with a strong adverse pressure gradient. *Journal of Fluid Mechanics*, 101:79–95, 1980.

Frenzen, P. and Vogel, C. A. On the magnitude and apparent range of variation of the von karman constant in the atmospheric surface layer. *Boundary-Layer Meteorology*, 72(4):371–392, 1995.

Ganapathisubramani, B., Hutchins, N., Hambleton, W., Longmire, E., and Marusic, I. Investigation of large-scale coherence in a turbulent boundary layer using two-point correlations. *Journal of Fluid Mechanics*, 524:57–80, 2005.

Ganapathisubramani, B., Hutchins, N., Monty, J., Chung, D., and Marusic, I. Amplitude and frequency modulation in wall turbulence. *Journal of Fluid Mechanics*, 712:61–91, 2012.

Geng, C., He, G., Wang, Y., Xu, C., Lozano-Durán, A., and Wallace, J. M. Taylor's hypothesis in turbulent channel flow considered using a transport equation analysis. *Physics of Fluids*, 27(2):025111, 2015.

Grass, A., Stuart, R., and Mansour-Tehrani, M. Vortical structures and coherent motion in turbulent flow over smooth and rough boundaries. *Philosophical Transactions of the Royal Society of London. Series A: Physical and Engineering Sciences*, 336(1640): 35–65, 1991.

Grass, A. J. Structural features of turbulent flow over smooth and rough boundaries. *Journal of fluid Mechanics*, 50(2):233–255, 1971.

Grimmond, C. and Oke, T. R. Aerodynamic properties of urban areas derived from analysis of surface form. *Journal of applied meteorology*, 38(9):1262–1292, 1999.

Gurka, R., Liberzon, A., Hefetz, D., Rubinstein, D., and Shavit, U. Computation of pressure distribution using PIV velocity data. In *Workshop on particle image velocimetry*, volume 2, 1999.

Hagishima, A., Tanimoto, J., Nagayama, K., and Meno, S. Aerodynamic parameters of regular arrays of rectangular blocks with various geometries. *Boundary-Layer Meteorology*, 132(2):315–337, 2009.

Haigermoser, C. Application of an acoustic analogy to PIV data from rectangular cavity flows. *Experiments in fluids*, 47(1):145–157, 2009.

Handford, P. and Bradshaw, P. The pulsed-wire anemometer. *Experiments in fluids*, 7 (2):125–132, 1989.

Hearst, R. J., Gomit, G., and Ganapathisubramani, B. Effect of turbulence on the wake of a wall-mounted cube. *Journal of Fluid Mechanics*, 804:513–530, 2016.

Hirt, F., Zurfluh, U., and Thomann, H. Skin friction balances for large pressure gradients. *Experiments in Fluids*, 4:296–300, 1986.

Hoyas, S. and Jiménez, J. Scaling of the velocity fluctuations in turbulent channels up to re τ= 2003. *Physics of fluids*, 18(1):011702, 2006.

Hutchins, N., Monty, J., Ganapathisubramani, B., Ng, H., and Marusic, I. Three-dimensional conditional structure of a high-Reynolds-number turbulent boundary layer. *Journal of Fluid Mechanics*, 673:255–285, 2011.

Hutchins, N. and Marusic, I. Large-scale influences in near-wall turbulence. *Philosophical Transactions of the Royal Society A: Mathematical, Physical and Engineering Sciences*, 365(1852):647–664, 2007.

Jackson, P. On the displacement height in the logarithmic velocity profile. *Journal of fluid mechanics*, 111:15–25, 1981.

Jiang, D., Jiang, W., Liu, H., and Sun, J. Systematic influence of different building spacing, height and layout on mean wind and turbulent characteristics within and over urban building arrays. *Wind and Structures*, 11(4):275–290, 2008.

Jiménez, J. Turbulent flows over rough walls. *Annual Review of Fluid Mechanics*, 36: 173–196, 2004.

Johnson, H., Parker, P. A., and Landman, D. Calibration designs for non-monolithic wind tunnel force balances. In *Proceedings of the 7th International Symposium on Strain-Gauge Balances; 10-13 May; Williamsburg, VA; United States*, 2010.

Kanda, M. Large-eddy simulations on the effects of surface geometry of building arrays on turbulent organized structures. *Boundary-Layer Meteorology*, 118(1):151–168, 2006.

Kempf, G. Neue ergebnisse der widerstandsforschung. *Werft, Reederei, Hafen*, pages 234–239, 1929.

Kline, S. and McClintock. Describing uncertainties in single-sample experiments. *Mechanical Engineering*, 75(1):3–8, 1953.

Kline, S. J., Reynolds, W. C., Schraub, F., and Runstadler, P. The structure of turbulent boundary layers. *Journal of Fluid Mechanics*, 30(4):741–773, 1967.

Kolmogorov, A. N. A refinement of previous hypotheses concerning the local structure of turbulence in a viscous incompressible fluid at high Reynolds number. *Journal of Fluid Mechanics*, 13(1):82–85, 1962.

Kono, T., Tamura, T., and Ashie, Y. Numerical investigations of mean winds within canopies of regularly arrayed cubical buildings under neutral stability conditions. *Boundary-layer meteorology*, 134(1):131, 2010.

Krogstad, P.-Å. and Antonia, R. Structure of turbulent boundary layers on smooth and rough walls. *Journal of Fluid Mechanics*, 277:1–21, 1994.

Krogstad, P.-Å. and Efros, V. Rough wall skin friction measurements using a high resolution surface balance. *International Journal of Heat and Fluid Flow*, 31:429–433, 2010. 6th International Symposium on Turbulence and Shear Flow Phenomena.

Krogstad, P.-Å., Antonia, R. A., and Browne, L. W. B. Comparison between rough- and smooth-wall turbulent boundary layers. *Journal of Fluid Mechanics*, 245:599–617, 1992.

Krogstad, P.-Å., Kaspersen, J., and Rimestad, S. Convection velocities in a turbulent boundary layer. *Physics of Fluids*, 10(4):949–957, 1998.

Laskari, A., de Kat, R., and Ganapathisubramani, B. Full-field pressure from snapshot and time-resolved volumetric PIV. *Experiments in fluids*, 57(3):44, 2016.

Lee, J. H., Sung, H. J., and Krogstad, P.-Å. Direct numerical simulation of the turbulent boundary layer over a cube-roughened wall. *Journal of Fluid Mechanics*, 669:397–431, 2011.

Lee, J. H., Seena, A., Lee, S.-h., and Sung, H. J. Turbulent boundary layers over rod-and cube-roughened walls. *Journal of Turbulence*, 13(1):N40, 2012.

Leonardi, S., Orlandi, P., Djenidi, L., and Antonia, R. A. Structure of turbulent channel flow with square bars on one wall. *International journal of heat and fluid flow*, 25(3): 384–392, 2004.

Leonardi, S. and Castro, I. P. Channel flow over large cube roughness: a direct numerical simulation study. *Journal of Fluid Mechanics*, 651:519–539, 2010.

Lettau, H. Note on aerodynamic roughness-parameter estimation on the basis of roughness-element description. *Journal of applied meteorology*, 8(5):828–832, 1969.

Ligrani, P. M. and Moffat, R. J. Structure of transitionally rough and fully rough turbulent boundary layers. *Journal of Fluid Mechanics*, 162:69–98, 1986.

Lumley, J. L. The structure of inhomogeneous turbulent flows. *Atmospheric turbulence and radio wave propagation*, 1967.

Macdonald, R. Modelling the mean velocity profile in the urban canopy layer. *Boundary-Layer Meteorology*, 97(1):25–45, 2000.

Macdonald, R., Griffiths, R., and Hall, D. An improved method for the estimation of surface roughness of obstacle arrays. *Atmospheric environment*, 32(11):1857–1864, 1998.

Martilli, A. and Santiago, J. L. Cfd simulation of airflow over a regular array of cubes. part ii: analysis of spatial average properties. *Boundary-Layer Meteorology*, 122(3): 635–654, 2007.

Marusic, I., Mathis, R., and Hutchins, N. Predictive model for wall-bounded turbulent flow. *Science*, 329(5988):193–196, 2010.

Marusic, I. On the role of large-scale structures in wall turbulence. *Physics of Fluids*, 13(3):735–743, 2001.

Mathis, R., Hutchins, N., and Marusic, I. Large-scale amplitude modulation of the small-scale structures in turbulent boundary layers. *Journal of Fluid Mechanics*, 628: 311–337, 2009.

Mathis, R., Hutchins, N., and Marusic, I. A predictive inner–outer model for streamwise turbulence statistics in wall-bounded flows. *Journal of Fluid Mechanics*, 681:537–566, 2011a.

Mathis, R., Marusic, I., Hutchins, N., and Sreenivasan, K. The relationship between the velocity skewness and the amplitude modulation of the small scale by the large scale in turbulent boundary layers. *Physics of Fluids*, 23(12):121702, 2011b.

Maurel, S., Borée, J., and Lumley, J. Extended proper orthogonal decomposition: Application to jet/vortex interaction. *Flow, Turbulence and Combustion*, 67(2):125–136, 2001.

McClure, J. and Yarusevych, S. Optimization of planar PIV-based pressure estimates in laminar and turbulent wakes. *Experiments in Fluids*, 58(5):62, 2017.

Medjnoun, T., Vanderwel, C., and Ganapathisubramani, B. Characteristics of turbulent boundary layers over smooth surfaces with spanwise heterogeneities. *Journal of Fluid Mechanics*, 838:516–543, 2018.

Mejia-Alvarez, R., Wu, Y., and Christensen, K. Observations of meandering superstructures in the roughness sublayer of a turbulent boundary layer. *International Journal of Heat and Fluid Flow*, 48:43–51, 2014.

Metzger, M. and Klewicki, J. A comparative study of near-wall turbulence in high and low Reynolds number boundary layers. *Physics of Fluids*, 13(3):692–701, 2001.

Millward-Hopkins, J., Tomlin, A., Ma, L., Ingham, D., and Pourkashanian, M. Estimating aerodynamic parameters of urban-like surfaces with heterogeneous building heights. *Boundary-Layer Meteorology*, 141(3):443–465, 2011.

Millward-Hopkins, J., Tomlin, A., Ma, L., Ingham, D., and Pourkashanian, M. The predictability of above roof wind resource in the urban roughness sublayer. *Wind Energy*, 15(2):225–243, 2012.

Millward-Hopkins, J., Tomlin, A., Ma, L., Ingham, D., and Pourkashanian, M. Aerodynamic parameters of a uk city derived from morphological data. *Boundary-layer meteorology*, 146(3):447–468, 2013.

Musker, A. J. Explicit expression for the smooth wall velocity distribution in a turbulent boundary layer. *AIAA Journal*, 17:655–657, 1979.

Nadeem, M., Lee, J. H., Lee, J., and Sung, H. J. Turbulent boundary layers over sparsely-spaced rod-roughened walls. *International Journal of Heat and Fluid Flow*, 56:16–27, 2015.

Nikuradse, J. *Laws of flow in rough pipes*. National Advisory Committee for Aeronautics Washington, 1950.

O'Donnel, F. B., Jr. A study of the effect of floating-element misalignment on skin-friction-balance accuracy. Defense research laboratory report, University of Texas., 1964.

Ooi, K. and Acosta, A. The utilization of specially tailored air bubbles as static pressure sensors in a jet. *Journal of fluids engineering*, 106(4):459–464, 1984.

Örlü, R. and Schlatter, P. On the fluctuating wall-shear stress in zero pressure-gradient turbulent boundary layer flows. *Physics of fluids*, 23(2):021704, 2011.

Ozarapoglu, V. *Measurements in Incompressible Turbulent Flows*. PhD thesis, Université Laval, Québec, Canada, 1973.

Pailhas, G., Barricau, P., Touvet, Y., and Perret, L. Friction measurement in zero and adverse pressure gradient boundary layer using oil droplet interferometric method. *Experiments in Fluids*, 47:195–207, 2009.

Perret, L. and Rivet, C. Dynamics of a turbulent boundary layer over cubical roughness elements: insight from PIV measurements and pod analysis. In *TSFP DIGITAL LIBRARY ONLINE*. Begel House Inc., 2013.

Perret, L. and Savory, E. Large-scale structures over a single street canyon immersed in an urban-type boundary layer. *Boundary-layer meteorology*, 148(1):111–131, 2013.

Perret, L., Basley, J., Mathis, R., and Piquet, T. The atmospheric boundary layer over urban-like terrain: Influence of the plan density on roughness sublayer dynamics. *Boundary-Layer Meteorology*, 170(2):205–234, 2019.

Perry, A. and Abell, C. Asymptotic similarity of turbulence structures in smooth-and rough-walled pipes. *Journal of Fluid Mechanics*, 79(4):785–799, 1977.

Placidi, M. and Ganapathisubramani, B. Effects of frontal and plan solidities on aerodynamic parameters and the roughness sublayer in turbulent boundary layers. *Journal of Fluid Mechanics*, 782:541–566, 2015.

Placidi, M. and Ganapathisubramani, B. Turbulent flow over large roughness elements: Effect of frontal and plan solidity on turbulence statistics and structure. *Boundary-Layer Meteorology*, 167:99–121, 2018.

Prandtl, L. Über flussigkeitsbewegung bei sehr kleiner reibung. *Verhandl. III, Internat. Math.-Kong., Heidelberg, Teubner, Leipzig, 1904*, pages 484–491, 1904.

Raffel, M., Willert, C. E., Scarano, F., Kähler, C. J., Wereley, S. T., and Kompenhans, J. *Particle Image Velocimetry: A Practical Guide*, chapter 11. Springer, 3rd edition edition, 2018.

Ran, B. and Katz, J. Pressure fluctuations and their effect on cavitation inception within water jets. *Journal of Fluid Mechanics*, 262:223–263, 1994.

Raupach, M. R. and Shaw, R. Averaging procedures for flow within vegetation canopies. *Boundary-layer meteorology*, 22(1):79–90, 1982.

Reis, M. L. C. C., Castro, R. M., and Mello, O. A. F. Calibration uncertainty estimation of a strain-gage external balance. *Measurement*, 46:24–33, 2013.

Reynolds, R. T. and Castro, I. P. Measurements in an urban-type boundary layer. *Experiments in Fluids*, 45:141–156, 2008.

Robinson, S. K. Coherent motions in the turbulent boundary layer. *Annual Review of Fluid Mechanics*, 23:601–639, 1991.

Rodríguez-López, E., Bruce, P. J. K., and Buxton, O. R. H. A robust post-processing method to determine skin friction in turbulent boundary layers from the velocity profile. *Experiments in Fluids*, 56:68, 2015.

Rodríguez-López, E., Bruce, P. J. K., and Buxton, O. R. H. On the formation mechanisms of artificially generated high Reynolds number turbulent boundary layers. *Boundary-Layer Meteorology*, 160:201–224, 2016.

Rodríguez-López, E., Bruce, P. J. K., and Buxton, O. R. H. Experimental measurement of wall shear stress in strongly disrupted flows. *Journal of Turbulence*, 18:271–290, 2017.

Runstadler, P. W., Kline, S. J., and Reynolds, W. C. An experimental investigation of the flow structure of the turbulent boundary layer. Technical Report Report MD-8, Stanford University, 1963.

Santiago, J., Coceal, O., Martilli, A., and Belcher, S. Variation of the sectional drag coefficient of a group of buildings with packing density. *Boundary-layer meteorology*, 128(3):445–457, 2008.

Schlatter, P. and Örlü, R. Quantifying the interaction between large and small scales in wall-bounded turbulent flows: a note of caution. *Physics of fluids*, 22(5):051704, 2010.

Schmidt, M. A., Howe, R. T., Senturia, S. D., and Haritonidis, J. H. Design and calibration of a microfabricated floating-element shear-stress sensor. *IEEE Transactions on Electron Devices*, 35:750–757, 1988.

Schubauer, G. Turbulent processes as observed in boundary layer and pipe. *Journal of Applied Physics*, 25(2):188–196, 1954.

Sheplak, M., Cattafesta, L. N., Nishida, T., and McGinley, C. B. Mems shear stress sensors: Promise and progress. In *Proceedings of the 24th AIAA Aerodynamic Measurement Technology and Ground Testing Conference*. ARC, 2004.

Sirovich, L. Turbulence and the dynamics of coherent structures. i. coherent structures. *Quarterly of applied mathematics*, 45(3):561–571, 1987.

Sreenivasan, K. R., Dhruva, B., and Gil, I. S. The effects of large scales on the inertial range in high-Reynolds-number turbulence. *arXiv preprint chao-dyn/9906041*, 1999.

Österlund, J. M., Johansson, A. V., Nagib, H. M., and Hites, M. H. A note on the overlap region in turbulent boundary layers. *Physics of Fluids*, 12(1):1–4, 2000.

Strutz, T. *Data Fitting and Uncertainty*, chapter 3. Springer Vieweg, 2nd edition edition, 2016.

Takimoto, H., Inagaki, A., Kanda, M., Sato, A., and Michioka, T. Length-scale similarity of turbulent organized structures over surfaces with different roughness types. *Boundary-layer meteorology*, 147(2):217–236, 2013.

Tennekes, H., Lumley, J. L., Lumley, J., et al. *A first course in turbulence*. MIT press, 1972.

Thomas, A. and Bull, M. On the role of wall-pressure fluctuations in deterministic motions in the turbulent boundary layer. *Journal of Fluid Mechanics*, 128:283–322, 1983.

Townsend, A. A. *Structure of Turbulent Shear Flow*. Cambridge University Press, 2nd edition edition, 1976.

Tsinober, A. *An informal introduction to turbulence*, volume 63. Springer Science & Business Media, 2001.

Van der Kindere, J., Laskari, A., Ganapathisubramani, B., and de Kat, R. Pressure from 2d snapshot PIV. *Experiments in fluids*, 60(2):32, 2019.

Van Oudheusden, B. PIV-based pressure measurement. *Measurement Science and Technology*, 24(3):032001, 2013.

Winter, K. G. An outline of the techniques available for the measurement of skin friction in turbulent boundary layers. *Progress in Aerospace Sciences*, 18:1–57, 1979.

Womack, K. M., Meneveau, C., and Schultz, M. P. Comprehensive shear stress analysis of turbulent boundary layer profiles. *Journal of Fluid Mechanics*, 879:360–389, 2019.

Xie, Z.-T., Coceal, O., and Castro, I. P. Large-eddy simulation of flows over random urban-like obstacles. *Boundary-layer meteorology*, 129(1):1, 2008.

Xie, Z. and Castro, I. P. Les and rans for turbulent flow over arrays of wall-mounted obstacles. *Flow, Turbulence and Combustion*, 76(3):291, 2006.

Yang, X. I. A., Sadique, J., Mittal, R., and Meneveau, C. Exponential roughness layer and analytical model for turbulent boundary layer flow over rectangular-prism roughness elements. *Journal of Fluid Mechanics*, 789:127–165, 2016.

Zhu, W., van Hout, R., and Katz, J. On the flow structure and turbulence during sweep and ejection events in a wind-tunnel model canopy. *Boundary-layer meteorology*, 124 (2):205–233, 2007.